

Copyright

by

Xiaojin Zheng

2021

**The Dissertation Committee for Xiaojin Zheng Certifies that this is the approved
version of the following Dissertation:**

**GEOMECHANICAL AND PETROPHYSICAL STUDIES TO
REDUCE RISK IN CO₂ GEOLOGICAL STORAGE**

Committee:

D. Nicolas Espinoza, Supervisor

Kamy Sepehrnoori

Matthew T. Balhoff

Timothy A. Meckel

Hugh Daigle

**GEOMECHANICAL AND PETROPHYSICAL STUDIES TO
REDUCE RISK IN CO₂ GEOLOGICAL STORAGE**

by

Xiaojin Zheng

Dissertation

Presented to the Faculty of the Graduate School of
The University of Texas at Austin
in Partial Fulfillment
of the Requirements
for the Degree of

DOCTOR OF PHILOSOPHY

The University of Texas at Austin
May 2021

Dedication

To my mom, dad, and sisters

Acknowledgements

First and foremost, I would like to express my deep and sincere gratitude to my supervisor, Dr. D. Nicolas Espinoza, for providing invaluable and continuous support throughout this research. His guidance helped me in all the time of research and writing of this dissertation. It was a great privilege to work and study under his guidance. His vision, enthusiasm, patience, and empathy have also deeply inspired me.

Second, I would like to extend my gratitude to my dissertation committee, Dr. Kamy Sepehrnoori, Dr. Matthew Balhoff, Dr. Tip Meckel, and Dr. Hugh Daigle, for providing insightful comments and suggestions. It was indeed a great journey for me to investigate CO₂ leakage problems with you in the past three years. I am also thankful to the Gulf Coast Carbon Center for providing sediment samples for this research.

I would like to thank the financial support from ExxonMobil through its membership in the University of Texas at Austin Energy Institute and DeWitt-Morette France-UT Endowed Excellence Grants. I am thankful to the ExxonMobil team (Ganeswara Dasari, Gary Teletzke, Martin Lacasse, Steve Davis, and Rodrick Myers) and collaborators from École des Ponts (Matthieu Vandamme and Jean-Michel Pereira) for providing meaningful feedback and generating the discussions that helped guide this research.

My sincere thanks also go to all the staff in the Hildebrand Department of Petroleum and Geosystems Engineering. I am thankful to Glen Baum, Gary Miscoe, and Daryl Nygaard, for helping me set up experimental devices and providing other laboratory supports. I would also like to thank Diane Landeros, Traci Laird, and Leah Freeman for helping me purchase laboratory supplies.

Finally, my completion of this research would not have been accomplished without the support of my family and friends. I am extremely grateful to all my lab mates in the Energy Geomechanics Laboratory and my other friends for their technical and emotional supports. I would like to express my special thanks to my mom, dad, and sisters for their encouragement and spiritual support throughout my life.

Abstract

GEOMECHANICAL AND PETROPHYSICAL STUDIES TO REDUCE RISK IN CO₂ GEOLOGICAL STORAGE

Xiaojin Zheng

The University of Texas at Austin, 2021

Supervisor: D. Nicolas Espinoza

Geological carbon storage is the key to reduce CO₂ emissions and mitigate global warming. The long-term storage of CO₂ in geological formations requires a secure sealing reservoir. Faults are key components in defining fluid migration pathways and sealing integrity in sedimentary basins. The injection of fluids into a compartmentalized formation increases pore pressure and might reactivate pre-existing faults. The rock compressibility determines the extent of pressure build-up and the risks associated with CO₂ injection. The transport properties of fault gouge and the potential clay smear in faults describe the resistance of fluid flow across faults and have direct implications on the height of the trapped CO₂ column. The CO₂ leakage into overlying formations compromises storage efficiency and the detection of subsurface leakages necessitates an effective pressure monitoring technique.

Thus, this dissertation includes the determination of rock compressibility, the quantification of fault transport properties, the prediction of CO₂ column height, and the monitoring of unfavorable leakages in CO₂ storage. The dissertation reports the uniaxial strain unloading compressibility of Frio sand for predicting pressure build-up during CO₂

injection. The transport properties of synthetic fault gouge are measured through permeability tests and CO₂ breakthrough pressure tests. A stochastic model is developed to account for the continuity of clay smears and statistically determine the possible range of CO₂ column height. Finally, a compositional model built in a reservoir simulator quantifies injection-induced changes of pore pressure above the injection zone and provides guidance for leakage detection.

The major conclusions of this dissertation are: (1) the uniaxial strain compressibility is about one half of the isotropic compressibility and the uniaxial strain unloading compressibility is about one-third of the uniaxial strain loading compressibility at comparable levels of effective stress; using incorrect compressibility values considerably underestimates the risks during injection; (2) the absolute permeability of synthetic fault gouge decreases by about one order of magnitude and the CO₂ breakthrough pressure increases approximately by half order of magnitude with increments of 10 wt% of clay; (3) the ductility, continuity, and location of clay smears add significant variability to the determination of fault sealing capacity; ductile clays favor continuous smears and results in a long CO₂ column; (4) the pore pressure increase above the injection zone as a result of partially undrained loading is up to 1% of the pressure increase in the injection zone for the chosen reservoir model; the pressure increase above the injection zone in the presence of leaks can be one order of magnitude larger than the case without leaks.

Together, the understanding of reservoir injectivity and sealing potential improves the reservoir risk management, provides assurance of the long-term CO₂ storage, and mitigates unintended subsurface leakages.

Table of Contents

List of Tables	xiii
List of Figures	xiv
Chapter 1: Introduction.....	1
1.1 Evaluation of reservoir injectivity in CO ₂ geological storage.....	1
1.2 Assessment of reservoir sealing capacity in CO ₂ geological storage	2
1.3 Monitoring of subsurface leakages in CO ₂ geological storage	3
1.4 Outline of the dissertation	3
Chapter 2: Measurement of Unloading Pore Volume Compressibility of Frio Sand under Uniaxial-strain Stress Path and Implications on Reservoir Pressure Management.....	6
2.1 Introduction	6
2.2 Methods.....	10
2.2.1 Sediment samples	10
2.2.2 Experimental apparatus and procedures	11
2.2.3 Theory for data analysis.....	13
2.3 Experimental results	14
2.4 Discussion	17
2.4.1 Relationship between loading and unloading compressibility.....	17
2.4.2 Relationship between isotropic and uniaxial strain compressibility ...	18
2.4.3 Summary of uniaxial strain PVC	19
2.4.4 Porosity models accounting for non-linear stress-strain relationship .	21
2.4.5 Comparison with compressibility data in the literature.....	23
2.4.6 Reservoir simulation of fluid injection into a compartmentalized reservoir	24

2.5 Conclusions	27
Chapter 3: Multiphase CO ₂ -brine Transport Properties of Synthetic Fault Gouge	29
3.1 Introduction	29
3.2 Materials and experimental methods	32
3.2.1 Sediments and synthetic sample preparation	32
3.2.2 Experimental methods	35
3.2.2.1 Core holder tests	35
3.2.2.2 Consolidation tests	36
3.2.2.3 Breakthrough pressure tests.....	37
3.3 Results	41
3.3.1 Absolute permeability.....	41
3.3.2 Breakthrough pressure and post-breakthrough CO ₂ permeability	44
3.3.3 Summary of permeability results in synthetic fault gouge	45
3.4 Discussion	48
3.4.1 Influence of fine-grain void ratio on absolute permeability	48
3.4.2 Implications of breakthrough pressure on maximum CO ₂ column height	50
3.4.3 Comparison with breakthrough pressure estimated through MICP	53
3.4.4 Prediction of fault breakthrough pressure and CO ₂ permeability from SGR.....	56
3.5 Conclusions	60
Chapter 4: Stochastic Quantification of CO ₂ Fault Sealing Capacity in Sand-Shale Sequences.....	62
4.1 Introduction	62
4.2 Methodology	67

4.2.1 Geological settings	67
4.2.2 Prediction of CO ₂ column height using the SGR-based method	68
4.2.3 Prediction of CO ₂ column height using the PSSF-based method	69
4.3 Results.....	73
4.3.1 SGR-based column height prediction.....	73
4.3.2 PSSF-based column height prediction.....	75
4.4 Discussion	77
4.4.1 Uncertainty quantification in the determination of maximum CO ₂ column height.....	77
4.4.2 Effects of clay ductility on CO ₂ column height and comparison with SGR-based method and juxtaposition only.....	81
4.4.3 Application of the PSSF-based method to hydrocarbon columns observed in the field	84
4.5 Conclusions	86
Chapter 5: Pressure Monitoring above the Injection Zone for CO ₂ Geological Storage ..	89
5.1 Introduction	89
5.2 Methodology	93
5.2.1 Reservoir geometry, boundary conditions, and input parameters	93
5.3 Results.....	95
5.3.1 Pressure increase in the above-injection-zone	95
5.3.2 Relationship between AIZ ΔP and IZ ΔP	99
5.3.3 Prediction of CO ₂ plume migration from AIZ pressure increase.....	101
5.4 Discussion: subsurface leakage detection	103
5.4.1 Presence of a leaky fault	103
5.4.2 Other relevant scenarios	106

5.5 Conclusions	109
Chapter 6: Conclusions.....	112
Appendix.....	116
A1 Measurement of Biot coefficient	116
A2 Uniaxial strain compressibility in the long unloading path	117
A3 Derivation of the relationship between isotropic compressibility and uniaxial strain compressibility	118
A4 Schematic diagram of consolidation setup.....	122
A5 Pressure steps in CO ₂ breakthrough pressure tests	122
A6 Comparison between natural gas column and CO ₂ column in the High Island Field	124
A7 Coupling between fluid flow and geomechanics.....	126
A8 Sensitivity tests on grid size in the numerical simulation	128
A9 Capillary pressure and relative permeability	129
A10 AIZ pressure monitoring using the SGR-based and the PSSF-based fault permeability.....	131
Bibliography	133

List of Tables

Table 2.1:	Summary of compressibility tests on Frio sand samples	12
Table 3.1:	Summary of experiments. Sample acronyms: pure sand (PS), silty sand (SS), and clayey sand (CS).	34
Table 5.1:	Input parameters.....	95
Table A1:	Pressure steps in CO ₂ breakthrough pressure tests.	123

List of Figures

Figure 2.1: CO ₂ storage and its relation to unloading compressibility and fault reactivation: (a) schematic diagram of CO ₂ injection in a geological formation bounded by faults; (b) injection and depletion stress paths illustrated by Mohr circles; and (c) porosity changes induced by injection and depletion.	7
Figure 2.2: Stress paths for three tests: the blue line represents the stress path of test 1, with isotropic stage, deviatoric stage, and uniaxial strain stage, in sequence; the gray line represents the stress path of test 2 (isotropic path); the red line represents the stress path of test 3 (uniaxial strain path), in which stepwise increase of confining pressure is performed to avoid shear failure.	13
Figure 2.3: Stress-strain curves for the three test types: (a) stress-strain curves for test 1 (sample 5063A): for each isotropic, deviatoric, and uniaxial strain section, there are several loading/unloading cycles; (b) confining pressure versus volumetric strain for test 2 (sample 5053.2B): there are four major loading paths with three small loading/unloading cycles and four major unloading paths unloaded to 1 MPa; (c) effective axial stress versus axial strain for test 3 (sample 5053.2D): there are several small loading/unloading cycles along the major loading path and four continuous unloading paths to 2 MPa.	15

- Figure 2.4: Summary of all the isotropic compressibility tests and the uniaxial strain compressibility tests: (a) isotropic path; and (b) uniaxial strain path. All the solid symbols represent the data during loading, while all the empty symbols represent the data during unloading. The logarithm of the compressibility decreases non-linearly with the increase of mean effective stress; loading compressibility is larger than unloading compressibility at comparable mean effective stress. 17
- Figure 2.5: Comparison of loading and unloading compressibility at comparable mean effective stress: (a) isotropic path; (b) uniaxial strain path. The compressibility data shows consistent stress-dependency; unloading compressibility is about 1/3 of the loading compressibility at comparable effective mean stress for both bases..... 18
- Figure 2.6: Uniaxial strain compressibility versus isotropic compressibility at comparable mean effective stress (sample 5053.2B and 5053.2D): uniaxial strain compressibility is about one half of isotropic compressibility, including both loading compressibility and unloading compressibility..... 19
- Figure 2.7: Uniaxial strain pore compressibility as a function of mean effective stress measured directly from uniaxial strain tests and estimated from isotropic and deviatoric paths assuming linear isotropic elasticity: solid symbols denote loading and empty symbols denote unloading; loading compressibility is 2.3 to 4.6 times larger than the unloading compressibility at the same mean effective stress. 21

Figure 2.8: Void ratio as a function of mean effective stress: (a) bulk compressibility test in sample 5053.2B; (b) uniaxial strain compressibility test in sample 5053.2D. The plots highlight the nonlinear response of rock compressibility with respect to mean effective stress.	22
Figure 2.9: Comparison between compressibility data from the literature and our experimental data under isotropic loading, isotropic unloading, uniaxial strain loading, and uniaxial strain unloading condition. The compressibility of unconsolidated sediments depends on their fabric and is higher than the consolidated rock under the same stress condition.	24
Figure 2.10: Reservoir simulation: (a) reservoir geometry; (b) reservoir pressure increase due to injection as a function of pore space utilization ratio with different compressibility values; ΔP indicates the pressure increase near the fault during CO ₂ injection. Uniaxial strain unloading compressibility results in the highest pore pressure build-up; (c) reservoir pressure increase due to injection as a function of pore space utilization ratio with different fault permeabilities. Lower fault permeability leads to higher pressure increase in a partially compartmentalized reservoir.....	27
Figure 3.1: Breakthrough pressure test setup: (a) confining fluid pump (blue line); (b) CO ₂ reservoir source; (c) CO ₂ sub-reservoir for injecting CO ₂ (red lines); (d) sediment sample; (e) isotropic core holder; (f) outlet port - may be connected to a pressure vessel; (g) data acquisition computer; (h) data acquisition hardware and electrical lines (green lines); (i) photo of inner core holder structure; (j, k) pressure transducers.	38

Figure 3.2: CO ₂ breakthrough monitoring (example for experiment CS-29): (a) evolution of upstream CO ₂ pressure P _p and confining pressure P _c ; (b) CO ₂ permeability after breakthrough. We increase CO ₂ pressure stepwise and monitor the experiment for CO ₂ breakthrough. CO ₂ flow rate increases after the immediate CO ₂ breakthrough and then decreases with decreasing upstream CO ₂ pressure. The yellow markers represent the measured CO ₂ breakthrough pressure interval.....	39
Figure 3.3: Absolute brine permeability as a function of clay content in a conventional core holder with the steady state method. The mean effective stress is between 6.4 MPa to 6.8 MPa. Absolute brine permeability decreases roughly by one order of magnitude when doubling clay content.	42
Figure 3.4: Results of consolidation tests for clay-sand mixtures: (a) porosity versus axial effective stress; (b) absolute permeability versus axial effective stress; (c) absolute permeability versus porosity. Porosity and the logarithm of permeability decrease linearly with the logarithm of axial stress. The logarithm of permeability is linearly proportional to porosity... .	43
Figure 3.5: Summary of CO ₂ breakthrough pressure tests. CO ₂ breakthrough pressure increases by about half order of magnitude when adding 10 wt% clay up to ~40 wt% into synthetic fault gouge samples. The breakthrough pressure interval is delimited by the maximum pressure with no breakthrough (lower bound) and the imposed fluid pressure that causes breakthrough (upper bound).	44

Figure 3.6: Post-breakthrough CO ₂ permeability: (a) CO ₂ permeability versus clay content; (b) CO ₂ permeability versus upstream CO ₂ pressure. The permeability decreases by about one to two orders of magnitude when adding 10 wt% of clay content into synthetic fault gouge samples. There is a power relationship between clay content and post-breakthrough CO ₂ permeability.....	45
Figure 3.7: Summary of permeability tests: (a) absolute brine permeability and post-breakthrough CO ₂ permeability versus clay content (the color bar indicates the mean effective stress); the hollow circles represent the permeability results during the consolidation; (b) post-breakthrough CO ₂ relative permeability versus clay content; we start to record the time after CO ₂ breaks through samples (the color bar indicates the time after breakthrough). CO ₂ relative permeability is always less than 1 (as expected in the absence of fractures) and decreases significantly with the increase of clay content. The maximum post-breakthrough relative permeability is less than 0.1 when clay content is larger than 40 wt%.....	47
Figure 3.8: Influence of fine-grain void ratio in absolute brine permeability. The fine-grain void ratio dictates absolute permeability, instead of bulk porosity or bulk void ratio. The cathodoluminescence image of Barnett shale (a binary grain-size system with coarse sands and fine clays -after (Milliken, 2019)) shows that the porosity of packed fine grains determines transport properties.....	49

Figure 3.9: Supercritical CO₂ breakthrough pressure: (a) comparison of our data scaled to field conditions (P = 6.89 MPa, T = 333 K) with the data from the literature including field cores and homogeneous sediment samples. Breakthrough pressure is inversely proportional to mean pore size, which is calculated with the Kozeny-Carman equation as a function of porosity and permeability; (b) summary of scCO₂ breakthrough pressure for clay/sand mixtures and corresponding CO₂ column height at field conditions. The CO₂ capillary sealing capacity is proportional to clay content through an exponential-law relationship (logistic function). 51

Figure 3.10: MICP results: (a) converted Hg to CO₂ pressure and saturations from MICP tests; (b) comparison between breakthrough pressures obtained from MICP and direct CO₂ breakthrough pressure measurements. The inferred breakthrough pressures from the second inflection point are similar to direct breakthrough pressure measurements. 55

Figure 3.11: Field application of our model in the High Island field: (a) shale volume distribution; (b) SGR; (c) predicted absolute permeability; (d) predicted CO₂ breakthrough pressure; (e) predicted CO₂ relative permeability. The predicted properties are based on relationships found in this work. 59

- Figure 4.1: Juxtaposition seal and clay smear fault sealing mechanisms and their implications on maximum CO₂ column height in a sand-shale sequence:
 (a) schematic diagram of a hanging wall and a footwall with increasing fault throw; (b) triangle diagram showing clay smear distribution in faults; smears become discontinuous when fault throw is larger than a critical throw; (c) an example of clay smear in a fault in Hambach mine, Germany (Vrolijk et al., 2016); (d) fault sealing mechanisms at different locations and trapped CO₂ column with plume on the hanging wall side.... 63
- Figure 4.2: Possible scenarios for the accumulation of CO₂ at a fault: accumulation from the side of the footwall, and accumulation from the side of the hanging wall (focus of this study)..... 66
- Figure 4.3: Determination of CO₂ column height using the SGR-based method: (a) stratigraphic profile of a sand-shale sequence in the High Island field; (b) SGR distribution in the triangle diagram; (c) breakthrough pressure distribution in the triangle diagram using Equation 4.4; (d) an example for CO₂ column height determination with 300 ft fault throw. CO₂ column height stops increasing once the buoyancy pressure line contacts the breakthrough pressure line. This is the maximum CO₂ column height. Leak points are not allowed where sand and shale juxtapose..... 69

Figure 4.4: Workflow for determination of CO ₂ column height including clay smears from the PSSF-based method: (a) result of juxtaposing the hanging wall with the footwall; (b) stochastic clay smear distribution within the fault; the blue intervals represent the breaches and the yellow intervals represent the smears (SSFc is assumed to be 3 in this case); (c) final leak point in the fault by combining juxtaposition sealing and clay smearing sealing; the blue intervals represent leak points and the pink intervals represent seals. The position of the closest leak point to the caprock determines the maximum attainable CO ₂ column height, assuming migration occurs through across-fault breaches only.	70
Figure 4.5: Stochastic distribution of clay smear location: the location of clay smear depends on the previous location and complies with a normal distribution within a range limited by the increment of fault throw.	72
Figure 4.6: Predictions of CO ₂ column height with increasing fault throw: (a) breakthrough pressure at the migration point predicted by the SGR-based method; (b) CO ₂ column height predicted by the SGR-based method; (c) relationship between number of leak points and fault throw in the juxtaposition case; (d) CO ₂ column height predicted by the juxtaposition only; (e) relationship between number of leak points and fault throw in the PSSF-based method; (f) CO ₂ column height predicted by the PSSF-based method; (g) relationship between number of leak points and fault throw for 100 simulations; (h) CO ₂ column height predicted by the PSSF-based method for 100 simulations.	74

Figure 4.7: Schematic diagram of CO ₂ column variability due to location and presence of leak points (sand-breach-sand): (a) inverse linear relationship between column height and fault throw; (b) discontinuous distribution of column height due to the presence of leak points. Small leak points are vulnerable to clay smears, while big leak points set an upper bound for the maximum possible column height.....	77
Figure 4.8: Statistical analysis of CO ₂ column height with increasing fault throw: (a) relative frequency of CO ₂ column height at different fault throws; (b) relative frequency of CO ₂ column height at major intervals of fault throw.....	79
Figure 4.9: Distribution maximum CO ₂ column heights at a fault throw of 450 ft for 100 simulations: (a) distribution of leak probability along the fault; (b) Cumulative frequency of maximum CO ₂ column height. The maximum possible column height is closely related to the distribution of leak probability along the depth.....	80
Figure 4.10: Distribution of clay smear and CO ₂ column height with different values of SSFc: (a) SSFc=2; (b) SSFc=4; (c) SSFc=6. The juxtaposition seal serves as the lower bound of CO ₂ height prediction. Clay smears (yellow intervals) add significant uncertainty to the prediction of CO ₂ column height. Ductile clay with a high SSFc tends to have a long smear in faults and thus support a large CO ₂ column.....	83

Figure 4.11: Upper bound for sealing capacity: our PSSF-based results (purple, cyan, and yellow markers) is superposed to the field data (black markers) (Yielding, 2002). There are one hundred realizations for each SSFc. The PSSF-based method reproduces variability observed in the field, highlights the uncertainties in the calculation of CO ₂ column height, and expose the limitations of the SGR-based method.....	85
Figure 5.1: Comparison among fully drained, partially undrained, and undrained conditions: the pore pressure changes under the fully undrained condition are proportional to the imposed volumetric strain but also depend on the hydraulic diffusivity of the porous medium.....	92
Figure 5.2: Reservoir geometry and boundary conditions. CO ₂ is injected into the injection zone (IZ) at the depth of 3,040 m. The injection zone is overlain by a caprock and five above-injection-zone (AIZ) layers for pressure monitoring.....	94
Figure 5.3: Pore pressure changes in the CO ₂ storage complex (half-domain shown because of symmetry: injector located on the right boundary). CO ₂ injection increases pressure $\Delta P > 1,000$ kPa in the injection zone. Partially undrained loading induced by CO ₂ injection causes changes of pore pressure $\Delta P < 20$ kPa around the reservoir layer. Pore pressure in AIZ sands along the injector increases in the first 10 days to a peak value and then decreases with time. Pore pressure in shale exhibits more gradual and long-lasting changes than in sands.....	96

Figure 5.4: CO ₂ injection rate and evolution of IZ and AIZ pressure changes: (a) injection rate and bottom-hole pressure increase in the injection zone (IZ); (b) pressure increase above the injection zone (AIZ) due to partially undrained loading.....	98
Figure 5.5: Poroelastic response at t = 8 days due to CO ₂ injection: (a) pore pressure changes in the storage complex and pressure fronts above the injection zone (AIZ); (b) vertical displacement. Surface heave is negligible while pore pressure change in the AIZ is in the order of 10 ¹ kPa.....	99
Figure 5.6: Relationship between AIZ ΔP and IZ ΔP: (1) ratio between AIZ ΔP and IZ ΔP as a function of time (sampled points along the injector); (2) ratio between AIZ ΔP and IZ ΔP as a function of horizontal distance to the injector (time = 8 days). The maximum ratio is about 1% in the areas of interest.....	100
Figure 5.7: Tracking of CO ₂ plume location with AIZ pressure monitoring. (a) CO ₂ plume half-length: the migration of CO ₂ plume is tracked through CO ₂ saturation. The 1,200 kPa pressure front in the IZ moves simultaneously with the CO ₂ plume for a constant injection rate. (b) Prediction of CO ₂ arrival using the ratio between AIZ ΔP and IZ ΔP at the same horizontal distance from the injector.....	102
Figure 5.8: Evolution of pore pressure and CO ₂ saturation above the injection zone in the presence of a leaky fault: (a) pressure increase in five AIZs along the injector, including the case with no leaks and the case with a leaky fault; (b) CO ₂ saturation in five AIZs along the fault. A leaky fault results in steady and higher increases in AIZ pressure than the base case.	105

Figure 5.9: Pressure change above the injection zone (AIZ) in the presence of a leaky fault. The red dashed box highlights the estimated leaky path based solely on the observed pore pressure field, which coincides with the location of the leaky fault.....	106
Figure 5.10: Distribution of CO ₂ plume after two years of CO ₂ injection in different scenarios: (a) base case with no leaks; (b) case with a sealing fault; (c) case with a leaky fault; (d) case with a leaky abandoned well; (e) case with a leaky injector; and (f) case with two injectors. The inserted plot at the top left of each sub-figure represents the schematic top-view of each layout.....	107
Figure 5.11: Pore pressure increases above the injection zone for different storage scenarios shown in Figure 5.10. The fault permeability varies from 10 nD to 1,000 mD. The effective permeability of leaky blocks in other leaky scenarios is 1,000 mD.....	109
Figure A1: Stress path for the Biot coefficient test.....	116
Figure A2: Regression analysis for the Biot coefficient test.....	117
Figure A3: Uniaxial strain compressibility in the long unloading path (sample 5053.2D): the secant constrained modulus is defined to describe the compressibility change with large unloaded stress; the plot summarizes the compressibility in four long unloading paths with different initial stress.....	118
Figure A4: Structure of the improved consolidation setup.....	122
Figure A5: Structure map of the HC Sand in the High Island 24L Field: the distribution of natural gas is highlighted in pink (Brown, 2011).....	125
Figure A6: Flow chart for the iterative two-way coupling (Tran et al., 2004).....	128

Figure A7: Sensitivity tests on grid size in the numerical simulation	129
Figure A8: Capillary pressure and relative permeability in CMG: figures (a) and (b) are for sand; figures (c) and (d) are for shale.	130
Figure A9: Impacts of different fault permeability on AIZ pressure changes: (a) SGR-based permeability predicted by experimental measurements on synthetic fault gouge; (b) PSSF-based permeability predicted by clay smear and shale juxtaposition sealing; (c) AIZ pressure increase in different cases.	132

Chapter 1: Introduction

1.1 EVALUATION OF RESERVOIR INJECTIVITY IN CO₂ GEOLOGICAL STORAGE

Geologic carbon storage is a potentially effective strategy to mitigate the release of CO₂ into the atmosphere (Nicot, 2008). Deep saline aquifers and depleted hydrocarbon reservoirs are the primary targets for long-term CO₂ storage (S Bachu, 2008; Emberley et al., 2004). Continued CO₂ injection into compartmentalized reservoirs leads to an increase of pore pressure and consequently lowers the effective stress, resulting in an unloading mechanical process (Guglielmi et al., 2015; J. Rutqvist et al., 2007; Verdon, 2014). The state of stress may move towards the shear yield envelope and pre-existing weak planes (such as faults and fractures) might be reactivated (Cappa, 2011; White, 2016). Reactivated faults may serve as preferential paths for unintended fluid flow (Rutqvist, 2016; Stork et al., 2015). Thus, the evaluation of the allowable injection pressure without compromising the reservoir integrity (i.e., the reservoir injectivity) helps the estimation of potential risks associate with CO₂ injection.

Reservoir compressibility affects the rate of pore pressure increase in a closed pore volume during fluid injection (Mathias et al., 2011). The conventional isotropic deformation assumption does not hold because the total vertical stress on reservoir rocks remains constant with zero lateral strain (Chertov et al., 2014; Ong et al., 2001; Segall & Fitzgerald, 1998). Considering unloaded stress on the formation, the parameter most relevant to fluid injection is the unloading pore volume compressibility under uniaxial strain conditions, which is currently not well documented in the literature. Thus, understanding the appropriate stress-strain path of compressibility is critical for the accurate prediction of pore pressure buildup during CO₂ injection (Ehlig-Economides et al., 2010; Shi et al., 2008).

1.2 ASSESSMENT OF RESERVOIR SEALING CAPACITY IN CO₂ GEOLOGICAL STORAGE

The reservoir sealing capacity is essential for the assessment of long-term CO₂ storage. A good sealing reservoir necessitates a pre-existing fault to be unfavorable for fluid flow and serve as a structural barrier. A variety of mechanisms contribute to a sealing fault, such as juxtaposition seal and fault gouge seal. Fault gouge seal includes clay smear, cataclasis or granular flow, and chemical sealing (Bense et al., 2013; Doughty, 2003; Draganits et al., 2005; Exner et al., 2013; Faulkner et al., 2010; Fristad et al., 1997; Zee et al., 2003). Juxtaposition seal instead is based on juxtaposing permeable units against less permeable lithologies (Fulljames et al., 1997).

The shale gouge ratio (SGR), the shale smear factor (SSF), and the probabilistic shale smear factor (PSSF) attempt to quantify the amount of clay mineral in faults (Childs et al., 2007; Fristad et al., 1997; Lindsay et al., 2009; Yielding et al., 1997). The clay content in natural fault gouge controls the transport properties of fault gouge (van der Zee & Urai, 2005). The sand-rich gouge has high permeability and low breakthrough pressure and thus favors fluid flow across faults (Espinoza, 2017; Guiltinan et al., 2018). However, the quantitative effects of clay content on fault permeability and CO₂ breakthrough pressure have not been thoroughly reported yet.

Reservoir sealing capacity controls the height of the trapped CO₂ column in CO₂ storage. Different juxtaposition scenarios and different modes of clay smears (continuous or truncated) alter the distribution of clay along faults and thus change transport properties of fault zones (Faerseth, 2006; Noorsalehi-Garakani et al., 2013, 2015; Schmatz et al., 2010; Schmatz & Urai, 2006). CO₂ tends to leak through the locations where sand juxtaposes with sand without clay smears (Childs et al., 2007). The position of leakage points in faults determines CO₂ column height and requires more attention for the assessment of reservoir sealing capacity.

1.3 MONITORING OF SUBSURFACE LEAKAGES IN CO₂ GEOLOGICAL STORAGE

Subsurface leakages in CO₂ geological storage are not uncommon (Bense et al., 2013; Cerveny et al., 2005). Fault leakage rates measured on the surface in natural CO₂ analogs vary from 0.006 to 0.3 ton/year/m² (Busch et al., 2010). The presence of fractured caprock, defective abandoned wells, or leaky injectors also permits unfavorable leakages to overlying formations. These potential subsurface leakages may adversely affect the existing mineral or groundwater resources (Zeidouni & Pooladi-Darvish, 2012a). Thus, implementing robust monitoring methods to detect subsurface leakages is critical to provide assurance of carbon sequestration.

Most monitoring techniques are based on measurements on the surface and in the injection zone. On-surface monitoring can capture large geophysical features but is limited by high costs, laborious interpretation, and a large buffer zone of signals imposed by overburden (Arts et al., 2004; Jonny Rutqvist et al., 2010). Monitoring in the injection zone enables direct access to the zone of interest and offers early leak detection, but remains limited to a few observation wells and small sampling volumes (Ajo-Franklin et al., 2013; Hovorka et al., 2006a; Zeidouni & Pooladi-Darvish, 2012b). The pressure monitoring above the injection zone is a new approach to document the extent of isolation of confining system and track the migration of CO₂ plume. It is meaningful to investigate the feasibility of using pressure monitoring above the injection zone to detect undesirable subsurface leakages.

1.4 OUTLINE OF THE DISSERTATION

This dissertation is organized into four main chapters. Chapter 2 reports the uniaxial strain unloading compressibility of unconsolidated Frio sand, a target formation for CO₂ geological storage in Texas. The tests consist of isotropic loading/unloading, deviatoric

loading/unloading, and uniaxial strain loading/unloading. Data analysis yields a comparison between loading and unloading compressibility under uniaxial strain conditions and a comparison between isotropic compressibility and uniaxial strain compressibility. A reservoir simulation is developed to quantify the effects of different compressibilities on pore pressure changes during injection in a compartmentalized reservoir.

Chapter 3 discusses the effects of grain size, porosity, and clay content on transport properties of smectite-rich fault gouge. Synthetic fault gouge samples are prepared with sand and clay from the Frio and Anahuac formations located on the coast of the Gulf of Mexico. This chapter reports absolute permeability, breakthrough pressure, and post-breakthrough CO₂ permeability of synthetic fault gouge. The results permit deriving quantitative relationships for transport properties as a function of clay content and evaluating effects of transport properties on CO₂ migration.

Chapter 4 investigates CO₂ fault sealing capacity through stochastic realizations of clay smears as a function of fault throw. This study shows an application example using borehole geophysical data from the High Island field on the coast of the Gulf of Mexico, comparing CO₂ column heights predicted by the SGR-based and PSSF-based methods. A sensitivity test on the critical shale smear factor investigates how the mechanical properties of clay smears alter CO₂ column height. The proposed stochastic method is applied to analyze the data from the literature and highlight the uncertainties in the prediction of the maximum CO₂ column height.

Chapter 5 examines the feasibility of implementing pressure monitoring above the injection zone (AIZ) to potentially track the CO₂ plume and detect undesirable leaks. A compositional model coupled with the geomechanics module is built in the reservoir simulator. The results investigate the magnitude, evolution, and distribution of the AIZ

pressure increase due to partially undrained loading and suggest the possible configuration of pressure sensors in the subsurface. The discussion section considers the presence of different subsurface scenarios, including the presence of a poorly cemented injector wellbore, a leaky abandoned wellbore, a leaky/sealing fault, and two injectors.

Finally, Chapter 6 summarizes the above works.

Chapter 2: Measurement of Unloading Pore Volume Compressibility of Frio Sand under Uniaxial-strain Stress Path and Implications on Reservoir Pressure Management

2.1 INTRODUCTION

Petroleum and geosystems engineering requires the injection of fluids into underground formations for multiple purposes. For example, carbon geological storage consists in injecting large quantities of carbon dioxide (CO_2) into aquifers or depleted hydrocarbon reservoirs (Figure 2.1a) (S Bachu, 2008; Emberley et al., 2004). The injection process usually increases pore pressure in reservoirs and consequently reduces effective stresses, resulting in an unloading mechanical process (Guglielmi et al., 2015; J. Rutqvist et al., 2007; Verdon, 2014). Reservoir pressurization is the opposite stress path to reservoir depletion during hydrocarbon production, a loading process with decreasing pore pressure (Segall & Fitzgerald, 1998; Sun et al., 2018).

Continued injection into compartmentalized reservoirs results in an increase of pore pressure P_p , which lowers the effective stress and slightly increases of porosity ϕ (Rutqvist et al., 2009; Zhou et al., 2008). The state of stress may move towards the shear yield envelope and pre-existing weak planes (such as faults and fractures) might be reactivated (Figures 2.1b and 2.1c) (Cappa, 2011; White, 2016). Reactivated faults may be able to serve as preferential paths for fluid flow, which can alter the compartmentalization of the reservoir and compromise seal integrity (Rutqvist, 2016; Stork et al., 2015).

Generally, reservoir compressibility affects the rate of pore pressure increase during injection in a closed pore volume (Mathias et al., 2011). The diffusivity equation for slightly compressible fluids is able to describe pore pressure changes with time during a drained process (Peters, 2012):

$$\nabla^2 P_p = \frac{\phi \mu C_t}{k} \frac{\partial P_p}{\partial t} \quad (2.1)$$

where μ represents the fluid viscosity, k represents the reservoir permeability, and C_t represents the overall reservoir compressibility. C_t can be written as $C_t = C_g S_g + C_o S_o + C_w S_w + C_f$, where C_f , C_g , C_o , C_w are the formation compressibility, gas compressibility, oil compressibility, and water compressibility, respectively; S represents saturations. The reservoir compressibility attenuates the incremental increase of pore pressure due to the injection and the likelihood of fault reactivation.

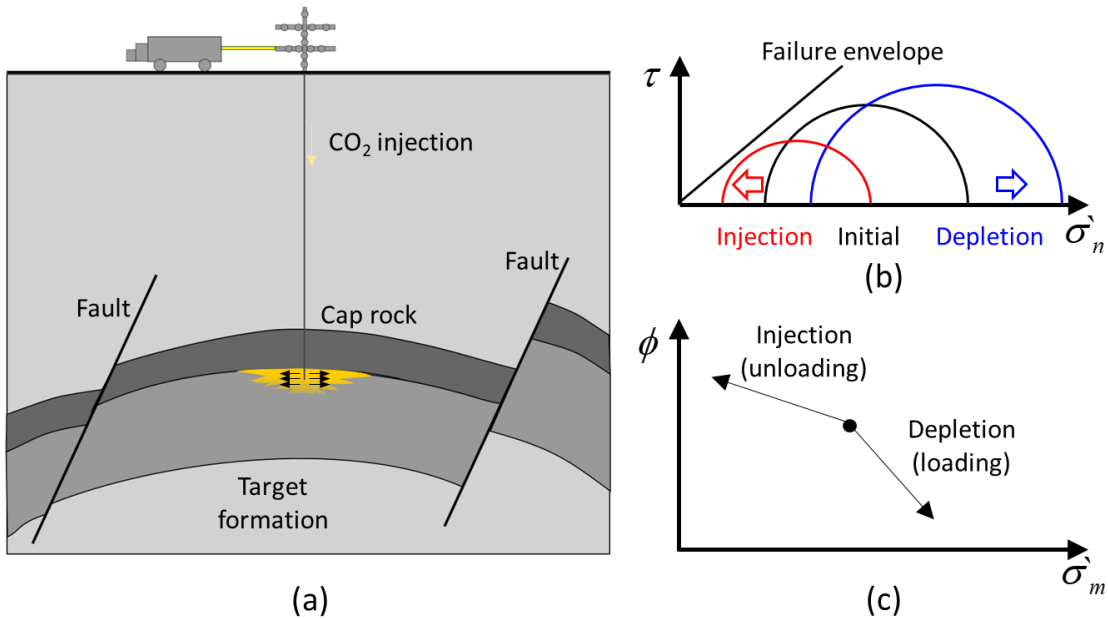


Figure 2.1: CO₂ storage and its relation to unloading compressibility and fault reactivation: (a) schematic diagram of CO₂ injection in a geological formation bounded by faults; (b) injection and depletion stress paths illustrated by Mohr circles; and (c) porosity changes induced by injection and depletion.

Traditionally, bulk compressibility has been measured under isotropic stress condition, which means the effective stress is changed by the same amount in all directions (Li et al., 2006). Isotropic bulk compressibility has two different execution modes: (1)

under constant pore pressure and changing confining pressure (C_{bc}^{iso}), and (2) under constant confining pressure and changing pore pressure (C_{bp}^{iso}) (Zimmerman, 1990). The confining pressure in an isotropic core holder is equivalent to the mean total stress. Likewise, the isotropic PVC are C_{pc}^{iso} and C_{pp}^{iso} (Zimmerman et al., 1986):

$$\left\{ \begin{aligned} C_{bc}^{iso} &= -\frac{1}{V_b} \left(\frac{\partial V_b}{\partial P_c} \right)_{P_p=cst} \\ C_{bp}^{iso} &= \frac{1}{V_b} \left(\frac{\partial V_b}{\partial P_p} \right)_{P_c=cst} \end{aligned} \right. \quad (2.2a)$$

$$\left\{ \begin{aligned} C_{pc}^{iso} &= -\frac{1}{V_p} \left(\frac{\partial V_p}{\partial P_c} \right)_{P_p=cst} \\ C_{pp}^{iso} &= \frac{1}{V_p} \left(\frac{\partial V_p}{\partial P_p} \right)_{P_c=cst} \end{aligned} \right. \quad (2.2c)$$

$$\left\{ \begin{aligned} C_{bc}^{iso} &= -\frac{1}{V_b} \left(\frac{\partial V_b}{\partial P_c} \right)_{P_p=cst} \\ C_{bp}^{iso} &= \frac{1}{V_b} \left(\frac{\partial V_b}{\partial P_p} \right)_{P_c=cst} \end{aligned} \right. \quad (2.2d)$$

where V_b is bulk volume, V_p is pore volume, P_p is pore pressure, and P_c is confining pressure. Both modes can exhibit loading or unloading stress paths.

However, the conventional isotropic deformation assumption does not hold for the deformation of thin and long reservoirs subjected to changes of pore pressure. During reservoir management, the total vertical stress (overburden $\sigma_{zz} = \sigma'_{zz} + \alpha P_p$) on the reservoir rock remains constant with zero lateral strain (Chertov et al., 2014; Ong et al., 2001; Segall & Fitzgerald, 1998). The uniaxial strain condition (change of vertical strain ε_{zz} with no change of lateral strains ε_{yy} and ε_{xy}) results in changes of effective stress σ' by different amounts in different directions. Similar to Equation 2.2, there are four uniaxial strain compressibilities, involving bulk and pore volumes (Zimmerman, 2000b):

$$\left\{ \begin{aligned} C_{bc}^{uni} &= \frac{1}{V_b} \left(\frac{\partial V_b}{\partial \sigma_{zz}} \right)_{\varepsilon_{xx}, \varepsilon_{yy}, P_p = cst} \\ C_{bp}^{uni} &= -\frac{1}{V_b} \left(\frac{\partial V_b}{\partial P_p} \right)_{\varepsilon_{xx}, \varepsilon_{yy}, \sigma_{zz} = cst} \end{aligned} \right. \quad (2.3a)$$

$$\left\{ \begin{aligned} C_{pc}^{uni} &= \frac{1}{V_p} \left(\frac{\partial V_p}{\partial \sigma_{zz}} \right)_{\varepsilon_{xx}, \varepsilon_{yy}, P_p = cst} \\ C_{pp}^{uni} &= -\frac{1}{V_p} \left(\frac{\partial V_p}{\partial P_p} \right)_{\varepsilon_{xx}, \varepsilon_{yy}, \sigma_{zz} = cst} \end{aligned} \right. \quad (2.3b)$$

$$\left\{ \begin{aligned} C_{pc}^{uni} &= \frac{1}{V_p} \left(\frac{\partial V_p}{\partial \sigma_{zz}} \right)_{\varepsilon_{xx}, \varepsilon_{yy}, P_p = cst} \\ C_{pp}^{uni} &= -\frac{1}{V_p} \left(\frac{\partial V_p}{\partial P_p} \right)_{\varepsilon_{xx}, \varepsilon_{yy}, \sigma_{zz} = cst} \end{aligned} \right. \quad (2.3c)$$

$$\left\{ \begin{aligned} C_{pc}^{uni} &= \frac{1}{V_p} \left(\frac{\partial V_p}{\partial \sigma_{zz}} \right)_{\varepsilon_{xx}, \varepsilon_{yy}, P_p = cst} \\ C_{pp}^{uni} &= -\frac{1}{V_p} \left(\frac{\partial V_p}{\partial P_p} \right)_{\varepsilon_{xx}, \varepsilon_{yy}, \sigma_{zz} = cst} \end{aligned} \right. \quad (2.3d)$$

where C_{bc}^{uni} and C_{bp}^{uni} are the uniaxial strain bulk volume compressibilities with respect to effective vertical stress and pore pressure; C_{pc}^{uni} and C_{pp}^{uni} are the uniaxial strain pore volume compressibilities (PVC) with respect to effective vertical stress and pore pressure. Historically, uniaxial strain compressibility was rarely measured on intact core samples due to equipment constraints and procedural difficulties (Fjar et al., 2008). Modern triaxial machines allow for PID (proportional–integral–derivative) control of confining pressure as a function of radial strain and allow for these measurements in order to obtain a more accurate value for $C_f = C_{pp}^{uni}$ (Dudley et al., 2016).

Uniaxial strain compressibility is also sensitive to the stress path. Unloading compressibility is much less reported than loading compressibility although loading uniaxial strain compressibilities have recently become available. The parameter most relevant to fluid injection is the unloading PVC under uniaxial strain condition (C_{pp}^{uni}). Understanding the appropriate stress path and appropriate laboratory measurement of compressibility is critical for evaluating risks associated with CO₂ injection and reservoir pressure management (Ehlig-Economides et al., 2010; Shi et al., 2008).

In this study, we report the uniaxial strain unloading compressibility of unconsolidated Frio sand, a target formation for CO₂ geological storage in Texas. The field cores were the onshore equivalent of the Frio found in the Gulf of Mexico Basin. The tests

consist of isotropic loading/unloading, deviatoric loading/unloading, and uniaxial strain loading/unloading. Data analysis yields porosity, uniaxial strain compressibility during loading and unloading, and a comparison between isotropic compressibility and uniaxial strain compressibility. Finally, we conduct a reservoir simulation sensitivity study to quantify the effects of different compressibilities and fault permeabilities on pore pressure changes during injection in a compartmentalized reservoir.

2.2 METHODS

2.2.1 Sediment samples

The sediment samples were obtained from the injection well of the Frio Pilot Test in the interval corresponding to the Frio formation (Kharaka et al., 2009b). The Frio site is vertically aligned with the South Liberty oil field, near Dayton, Texas, in a region of the Gulf Coast where large industrial sources of CO₂ are present (Doughty et al., 2008). The Oligocene Frio Formation is a fluvio-deltaic system that extends through the Gulf of Mexico Basin (Hovorka et al., 2006b; Swanson et al., 2013). Frio sand is composed of subarkosic fine-grained, moderately sorted quartz sand grains, and minor amounts of illite and calcite (Kharaka et al., 2006, 2009b). The CO₂ injection well was perforated at the depth of the Frio C sand in the interval 5056-5072 ft (Hovorka et al., 2004; Jung et al., 2017). The cores were obtained at depths around 5053-5056 ft and 5063-5066 ft.

The Frio sand is an unconsolidated sediment with no cohesive strength (other than slight cohesion due to evaporated salt from the in-situ brine). We used epoxy to hold the unconsolidated sand during coring. The initial porosity measured with well logging tools is about 33% (Jung et al., 2017). The average initial porosity measured with mercury intrusion capillary pressure (MICP) is 32.5%, and the porosity measured with the manometric method in the laboratory is 33.8%. In the interval 5053-5056 ft, most grains

are larger than 10 μm with a mean grain size of \sim 100 μm . The pore throat distribution from MICP yields $d_{10}= 1.7 \mu\text{m}$, $d_{50}= 20 \mu\text{m}$, $d_{90}= 33 \mu\text{m}$.

2.2.2 Experimental apparatus and procedures

We used a TerraTek triaxial frame, which is capable of applying up to 2,205 kN axial load and total radial stresses up to 138 MPa (Ramos et al., 2017). We place the sample between two stainless steel endcaps and jacket it with a heat shrink plastic tube. Axial displacements are an average from four independent cantilever arms, and total radial displacements are an average from two perpendicular measurements from independent cantilever arms. All the data (including axial strain, radial strain, deviatoric stress, confining pressure, and pore pressure) are recorded every 1 s.

Uniaxial-strain conditions are obtained by PID control, which regulates the applied confining pressure as a function of radial strain in response to either change of pore pressure (pore pressure change test), or the axial stress (effective stress change test). For the pore pressure change test, the system maintains constant axial total stress while pore pressure decreases. For the effective stress change test, the pore pressure is maintained constant while axial effective stress increases. These two types of experiments correspond to the two conditions in Equation 2.3c and 2.3d.

Table 2.1 summarizes all the experiments performed in this study. All the samples are tested in dry conditions, except sample 5053.2A saturated with brine to measure the Biot coefficient (detailed measurement procedures can be found in Appendix A1). The numbers in the sample ID indicate the depth (ft) from where the cores were retrieved.

For test 1 (sample 5053.2A and 5063A), the experiments are conducted following three stages (blue line in Figure 2.2): (1) isotropic loading, (2) deviatoric loading to in-situ

stress state, and (3) uniaxial strain loading. Deviatoric stress σ_D and mean effective stress σ_m^* are defined as:

$$\sigma_D = \sigma_{zz} - \sigma_{xx} \quad (2.4)$$

$$\sigma_m^* = \frac{\sigma_{xx}^* + \sigma_{yy}^* + \sigma_{zz}^*}{3} \quad (2.5)$$

where $\sigma_{xx}^* = \sigma_{yy}^*$ because of axisymmetric conditions. In stage (1), the rock sample is compressed under isotropic loading. Deviatoric stress is zero while mean effective stress increases. In stage (2), the sample is subjected to deviatoric loading to the in-situ stress condition. Confining pressure is constant while deviatoric stress increases. In stage (3), we increase the deviatoric stress while maintaining radial strain constant.

Table 2.1: Summary of compressibility tests on Frio sand samples

Test	Sample ID	Stress path	Tests conducted
1	5053.2A/ 5063A	One major loading path with small loading/unloading cycles	Isotropic/deviatoric/ uniaxial strain compressibility tests
2	5053.2B	Four major loading paths with three small loading/unloading cycles, and four major unloading paths	Isotropic compressibility tests
3	5053.2D	Four major loading paths with three small loading/unloading cycles, and four major unloading paths	Uniaxial strain compressibility tests

For test 2 (sample 5053.2B), we conduct the experiment under the isotropic condition during all major and minor loading/unloading cycles (gray line in Figure 2.2). For test 3, we load sample 5053.2D mostly under the uniaxial strain condition with short intervals of isotropic loading to avert shearing (red line in Figure 2.2).

The friction angle of Frio sand is about 38° (Jung et al., 2017). According to the Mohr-Coulomb criterion, the maximum stress anisotropy is $\sigma_1^*/\sigma_3^* = 4.2$, where σ_1^* is the maximum principal effective stress and σ_3^* is the minimum principal effective stress.

Likewise, the critical state line has a slope as $\sigma_D / \sigma'_m = 1.55$. We maintain the loading path below the critical state line to avoid shear yield during the entire loading process.

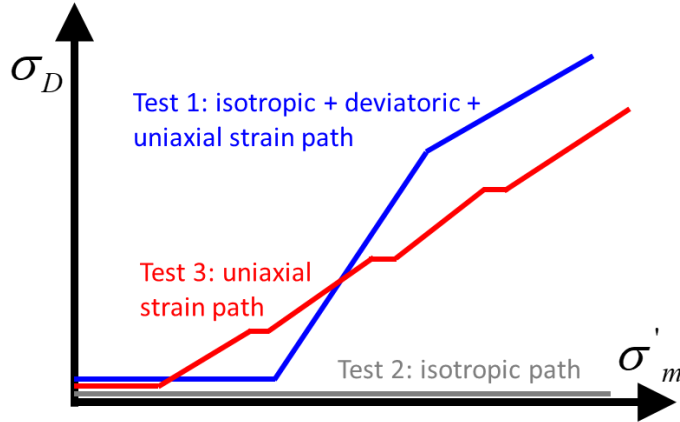


Figure 2.2: Stress paths for three tests: the blue line represents the stress path of test 1, with isotropic stage, deviatoric stage, and uniaxial strain stage, in sequence; the gray line represents the stress path of test 2 (isotropic path); the red line represents the stress path of test 3 (uniaxial strain path), in which stepwise increase of confining pressure is performed to avoid shear failure.

2.2.3 Theory for data analysis

We obtain bulk modulus K from the isotropic path, Young's modulus E from the deviatoric path, and constrained modulus M from the uniaxial strain path. Young's modulus (E) is the slope of the deviatoric stress curve as a function of axial strain in a deviatoric test, while bulk modulus (K) is defined as the slope of the isotropic stress as a function of the volumetric strain. The volumetric strain is $\varepsilon_{vol} = \varepsilon_{xx} + \varepsilon_{yy} + \varepsilon_{zz}$, where ε_{xx} and ε_{yy} are horizontal strains, and ε_{zz} is the vertical strain. For uniaxial strain tests, $\varepsilon_{xx} = \varepsilon_{yy} = 0$, and the volumetric strain reduces to $\varepsilon_{vol} = \varepsilon_{zz}$. The inverse of the compressibility in a uniaxial strain test is called constrained modulus and it is defined as

$$M = \left(\frac{\Delta \sigma'_{zz}}{\Delta \varepsilon_{zz}} \right)_{\varepsilon_{xx}, \varepsilon_{yy} = cst} \quad (2.6)$$

Based on Equations 2.3a and 2.6, and using the equation $\varepsilon_{vol} = dV_b / V_b$ that disregards the mineral grain deformation, the uniaxial strain bulk volume compressibility is

$$C_{bc}^{uni} = \frac{1}{M} \quad (2.7)$$

If the rock is under constant overburden stress ($\sigma_{zz} = \sigma^*_{zz} + \alpha P_p$), changes in pore pressure result in changes of vertical effective stress ($\Delta\sigma^*_{zz} = -\alpha\Delta P_p$), according to linear poroelasticity where α is the Biot coefficient. The Biot coefficient is defined from the stress-strain relationship $\varepsilon = \underline{\underline{D}} \cdot (\underline{\underline{\sigma}} - \alpha P_p \underline{\underline{I}})$, where $\underline{\underline{D}}$ is the inverse of the stiffness matrix and $\underline{\underline{I}}$ is the identity matrix. Therefore, Equation 2.6 can be written as $M = -\left(\frac{\alpha\Delta P_p}{\Delta\varepsilon_{zz}}\right)_{\varepsilon_{xx}, \varepsilon_{yy}=cst}$. The uniaxial strain compressibility for changes of pore pressure becomes

$$C_{bp}^{uni} = \frac{\alpha}{M} \quad (2.8)$$

The current porosity during loading can be derived from its definition and the variations in volumetric strain, and it is equal to

$$\phi = 1 - \frac{(1-\phi_0)(1-\varepsilon_m)}{(1-\varepsilon_{vol})} \quad (2.9)$$

where ε_m is the strain of the rock matrix and may include occluded porosity. If we assume the matrix compressibility is much smaller than the bulk compressibility ($\varepsilon_m \ll \varepsilon_{vol}$), the current porosity simplifies to

$$\phi = \frac{\phi_0 - \varepsilon_{vol}}{1 - \varepsilon_{vol}} \quad (2.10)$$

2.3 EXPERIMENTAL RESULTS

Figure 2.3 summarizes the stress-strain results for the three test types. Each stress-strain curve has several loading-unloading cycles along the entire stress path. The stress-

strain curve is non-linear and exhibits both elastic and plastic deformation during the loading process. The sample recovers elastic deformation with decreasing effective stress during the unloading process. The overlay of unloading and reloading curves in the small cycles indicates mostly elastic deformation in these two processes.

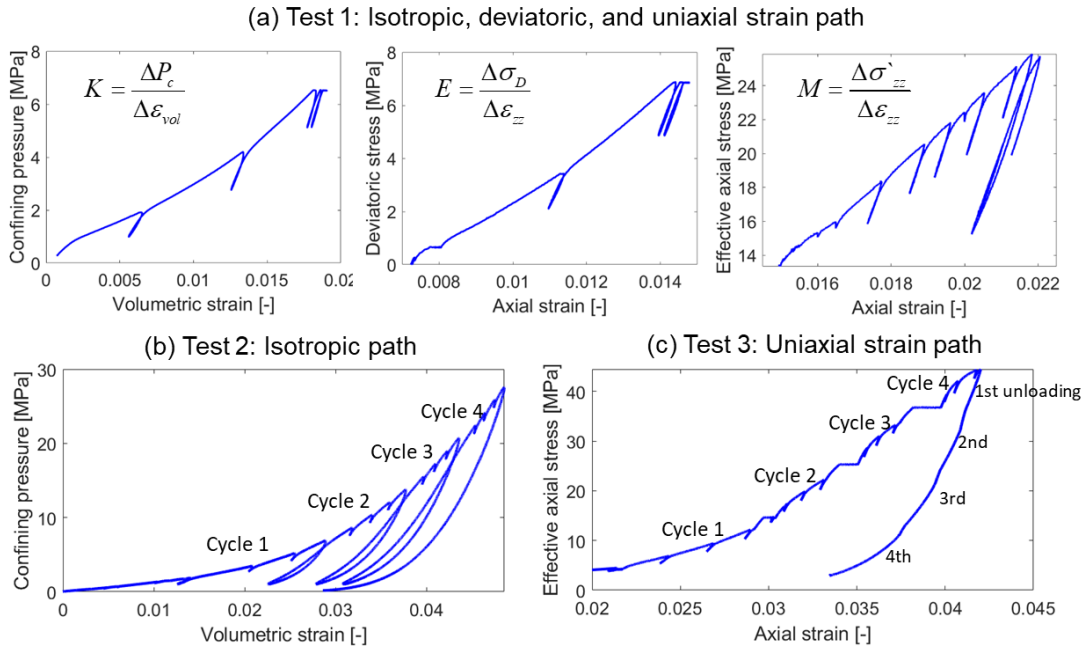


Figure 2.3: Stress-strain curves for the three test types: (a) stress-strain curves for test 1 (sample 5063A): for each isotropic, deviatoric, and uniaxial strain section, there are several loading/unloading cycles; (b) confining pressure versus volumetric strain for test 2 (sample 5053.2B): there are four major loading paths with three small loading/unloading cycles and four major unloading paths unloaded to 1 MPa; (c) effective axial stress versus axial strain for test 3 (sample 5053.2D): there are several small loading/unloading cycles along the major loading path and four continuous unloading paths to 2 MPa.

Test 1 consists of an isotropic stage, a deviatoric stage, and a uniaxial strain stage. Most of the porosity reduction happens in the first stage with $\varepsilon_{vol} \sim 10^{-2}$ (isotropic stage). The porosity varies less than 1% in the following two stages (deviatoric loading and uniaxial strain loading). The determined Biot coefficient at σ'_m from 3.5 to 7 MPa is $\alpha =$

0.944 (see Appendix A1). Tests 2 and 3 follow isotropic and uniaxial strain paths in a wide stress range. The concave loading line in the stress-strain curve shows that the rock stiffness increases with the increasing effective stress.

The unloading stress-strain curves show consistent steeper slopes than the loading curves, which indicates that the loading stiffness is smaller than the unloading stiffness at comparable mean effective stress. Figure 2.4 summarizes the results of all the isotropic compressibility tests and uniaxial strain compressibility tests. Loading compressibility is always larger than unloading compressibility at the same mean effective stress. Both the isotropic compressibility and uniaxial strain compressibility decrease with increasing mean effective stress, which suggests that compressibility is highly stress-dependent. The gaps among the data clusters in Figure 2.4b are due to a stepwise increase of confining pressure. The measured uniaxial strain pore compressibility of Frio sand is about 0.65 to 3.63 GPa⁻¹ (4.5 to 25 μ sip) for loading and 0.26 to 1.45 GPa⁻¹ (1.8 to 10 μ sip) for unloading in the range of 4.5 to 26 MPa of mean effective stress.

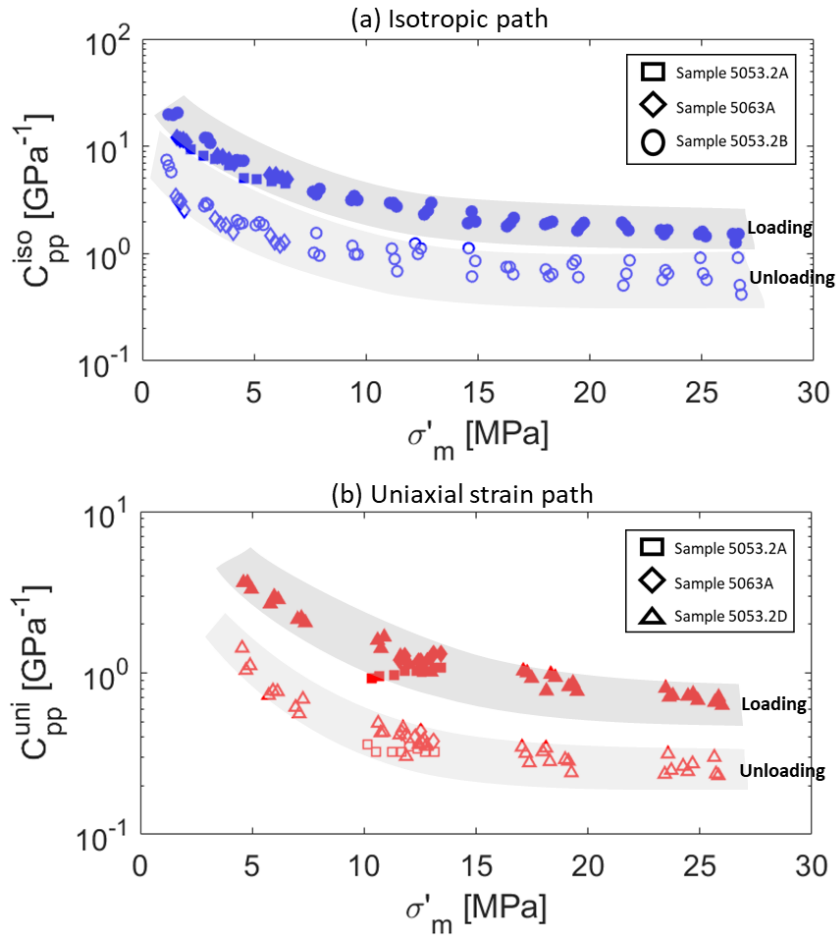


Figure 2.4: Summary of all the isotropic compressibility tests and the uniaxial strain compressibility tests: (a) isotropic path; and (b) uniaxial strain path. All the solid symbols represent the data during loading, while all the empty symbols represent the data during unloading. The logarithm of the compressibility decreases non-linearly with the increase of mean effective stress; loading compressibility is larger than unloading compressibility at comparable mean effective stress.

2.4 DISCUSSION

2.4.1 Relationship between loading and unloading compressibility

Experimental results show that the unloading compressibility is about 2.5 times lower than the loading compressibility (Figure 2.4). This hysteresis in the load-unload

cycle can be attributed to damage occurring during the loading cycle (Plona et al., 1995). The loading and unloading compressibilities show a clear relationship (Figure 2.5). The unloading compressibility is about 1/3 of the loading compressibility at comparable effective mean stress for both the isotropic path and the uniaxial strain path. The ratio between the unloading compressibility and the loading compressibility for most data points is between 1/4 and 1/2. The uniaxial strain compressibility in the long unloading path is discussed in Appendix A2.

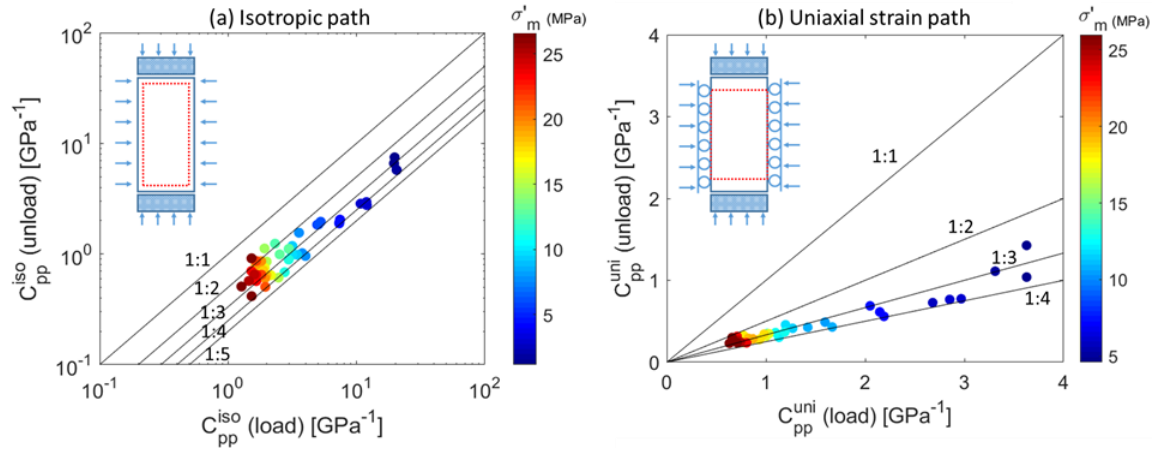


Figure 2.5: Comparison of loading and unloading compressibility at comparable mean effective stress: (a) isotropic path; (b) uniaxial strain path. The compressibility data shows consistent stress-dependency; unloading compressibility is about 1/3 of the loading compressibility at comparable effective mean stress for both bases.

2.4.2 Relationship between isotropic and uniaxial strain compressibility

We plot the uniaxial strain compressibility against the isotropic compressibility in Figure 2.6 in order to compare them at the same mean effective stress. Most of the data points are distributed around the 1:2 line, indicating that uniaxial strain compressibility is about one half of isotropic compressibility for both loading and unloading paths. Regression analysis shows that $C^{uni} = 0.51C^{iso}$, with $R^2 = 0.9850$.

According to isotropic linear elasticity theory, the relationship between uniaxial strain compressibility and isotropic compressibility can be expressed as

$$C^{uni} = \frac{(1+\nu)}{3(1-\nu)} C^{iso} \quad (2.11)$$

The detailed derivation of this equation is available in the Appendix A3 and other references (Andersen, 1988; Anderson et al., 1985). The equivalent Poisson' ratio calculated from the regression is 0.211.

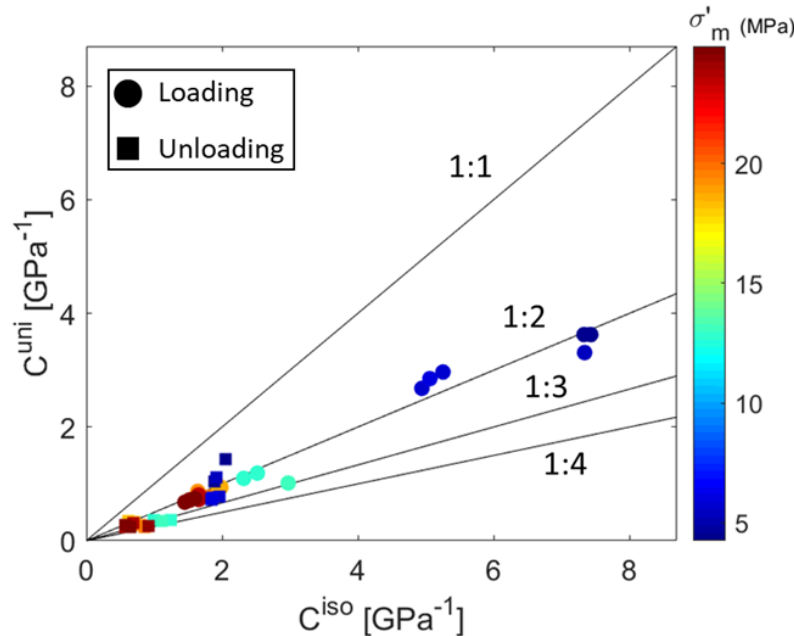


Figure 2.6: Uniaxial strain compressibility versus isotropic compressibility at comparable mean effective stress (sample 5053.2B and 5053.2D): uniaxial strain compressibility is about one half of isotropic compressibility, including both loading compressibility and unloading compressibility.

2.4.3 Summary of uniaxial strain PVC

Reservoir simulation requires an accurate input of PVC. This value plays a critical role in material balance calculations for depletion and injection processes (Ong et al.,

2001). Using the theoretical relations among the compressibilities, the pore volume compressibilities are (see Appendix A3):

$$\left\{ \begin{array}{l} C_{pc}^{uni} = \frac{\alpha}{\phi M} \\ C_{pp}^{uni} = \frac{-2(1-2\nu)\alpha^2 + 3(1-\nu)[\alpha(1+\phi) - \phi]}{\phi(1+\nu)M} \end{array} \right. \quad (2.12a)$$

$$\left\{ \begin{array}{l} C_{pc}^{uni} = \frac{\alpha}{\phi M} \\ C_{pp}^{uni} = \frac{-2(1-2\nu)\alpha^2 + 3(1-\nu)[\alpha(1+\phi) - \phi]}{\phi(1+\nu)M} \end{array} \right. \quad (2.12b)$$

Equation 2.12b simplifies to $C_{pp}^{uni} \sim C_{pc}^{uni} \sim \frac{1}{\phi M}$ when $K_{drained} \ll K_{unj}$ ($\alpha \sim 1$),

where $K_{drained}$ is the jacketed drained bulk modulus and K_{unj} is the unjacketed drained bulk modulus. Hence, the pore compressibility is roughly equal to the bulk compressibility divided by porosity.

The uniaxial strain pore compressibility could also be estimated from the isotropic tests ($C_{pp}^{uni_iso}$) and deviatoric tests ($C_{pp}^{uni_dev}$) with the assumption of linear isotropic elasticity, with known values of K , ν or E , ν :

$$\left\{ \begin{array}{l} C_{pp}^{uni_iso} = \frac{1}{\phi M^{iso}} = \frac{(1+\nu)}{3\phi(1-\nu)K} \end{array} \right. \quad (2.13a)$$

$$\left\{ \begin{array}{l} C_{pp}^{uni_dev} = \frac{1}{\phi M^{dev}} = \frac{(1+\nu)(1-2\nu)}{\phi(1-\nu)E} \end{array} \right. \quad (2.13b)$$

Figure 2.7 summarizes uniaxial strain pore compressibility from both direct measurements and theoretical estimations (Equation 2.13). We use the equivalent Poisson's ratio from Figure 2.6 in our calculations. The loading PVC is 2.3 to 4.6 times larger than the unloading PVC at the same mean effective stress.

Generally, plastic deformation accompanies the volumetric change during uniaxial strain loading. The theoretical estimations of pore compressibility from isotropic and deviatoric paths may not be accurate due to visco-plastic deformations but help support the quantification of stress-sensitivity of the uniaxial strain pore compressibility. Accurate estimations of uniaxial strain compressibility require direct experimental measurements.

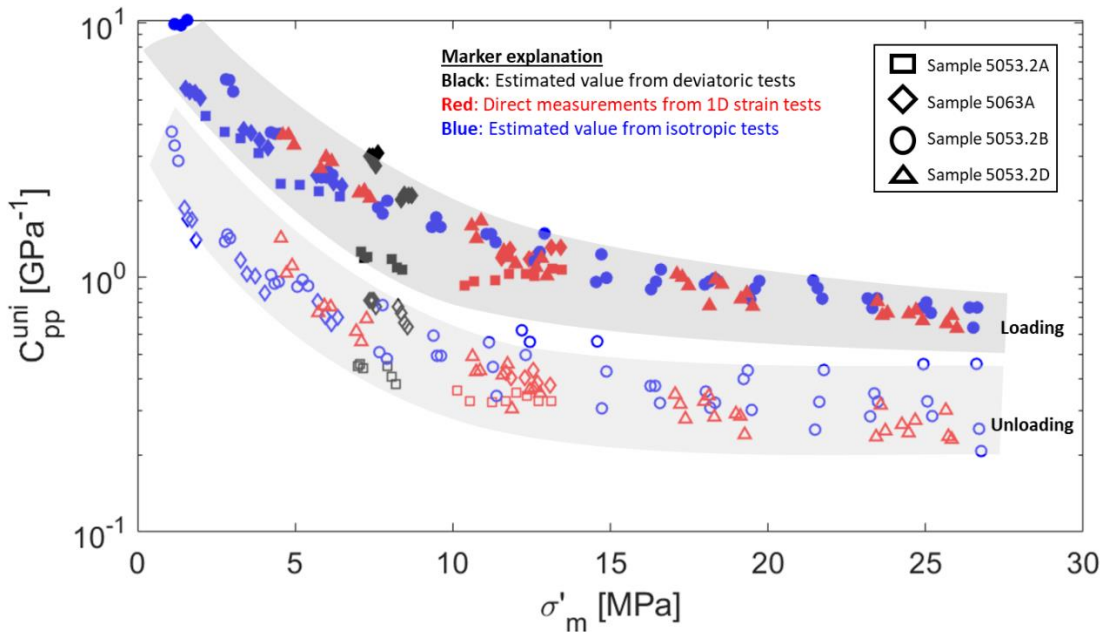


Figure 2.7: Uniaxial strain pore compressibility as a function of mean effective stress measured directly from uniaxial strain tests and estimated from isotropic and deviatoric paths assuming linear isotropic elasticity: solid symbols denote loading and empty symbols denote unloading; loading compressibility is 2.3 to 4.6 times larger than the unloading compressibility at the same mean effective stress.

2.4.4 Porosity models accounting for non-linear stress-strain relationship

The non-linear relationship between uniaxial strain compressibility and mean effective stress is not straightforward to capture in reservoir simulation, since most simulators assume a linear change of porosity with pore pressure (equivalent to mean effective stress). Alternatively, reservoir simulators may use “compressibility tables”. Porosity can be also expressed as void ratio by $e = \phi / (1 - \phi)$. Hence, the void ratio is a function of mean effective stress (Figure 2.8). There is a clear linear relationship between void ratio and the logarithm of mean stress during loading or unloading processes for both isotropic compressibility and uniaxial strain compressibility, such that:

$$\begin{cases} \Delta e = \lambda \ln \frac{\sigma'_m}{\sigma'_{m0}} & (\text{loading}) \\ \Delta e = \kappa \ln \frac{\sigma'_m}{\sigma'_{m0}} & (\text{unloading}) \end{cases} \quad (2.14)$$

where λ is the slope of void ratio as a function of the logarithm of mean effective stress during loading and κ is the slope during unloading. The parameter λ captures both the elastic and plastic strain during loading, while κ captures the elastic strain during unloading. For bulk compressibility test, $\lambda = -0.020$, $\kappa = -0.0065$ (Figure 2.8a). For uniaxial strain compressibility test, $\lambda^* = -0.016$, $\kappa^* = -0.005$ (Figure 2.8b), where λ^* and κ^* are the equivalent λ and κ parameters in the uniaxial strain condition. Instead of using a compressibility table, the parameters λ and κ (or λ^* and κ^*) are able to capture the nonlinear rock compressibility and can be implemented in reservoir simulation.

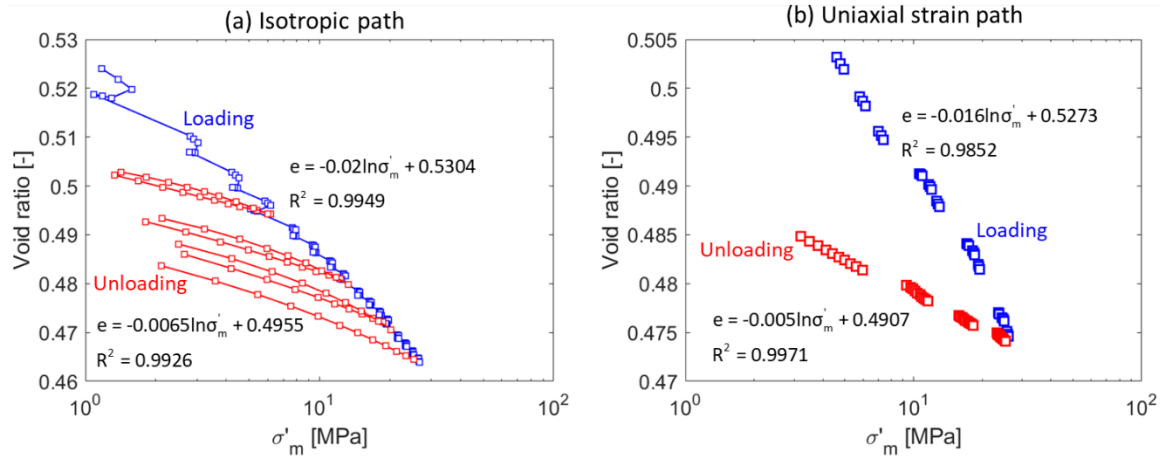


Figure 2.8: Void ratio as a function of mean effective stress: (a) bulk compressibility test in sample 5053.2B; (b) uniaxial strain compressibility test in sample 5053.2D. The plots highlight the nonlinear response of rock compressibility with respect to mean effective stress.

2.4.5 Comparison with compressibility data in the literature

Compressibility data in the literature exhibits large variability. Figure 2.9 summarizes the PVC data of different rock types under isotropic loading, isotropic unloading, uniaxial strain loading, and uniaxial strain unloading. Our experimental data are drawn as solid markers. The isotropic loading compressibility of Boise sandstone, Bandera sandstone, and Berea sandstone are smaller than Frio sandstone compressibility, probably due to the friable nature of Frio sand (Anderson et al., 1985; Zimmerman, 1990). The unconsolidated arkosic sand reported by Sawabini (1974) exhibits a large compressibility compared with those of other relatively consolidated sandstones, as expected due to grain rearrangement (Newman, 1973).

The compressibility of unconsolidated sediments depends on their fabric. Unconsolidated sands have angular grains and negligible grain-to-grain cementation. The result is a small area of grain-to-grain contact prone to high stress concentrations and grain failure at high effective stresses (Chertov et al., 2014). Therefore, the amount of recoverable strain is small (often less than 10%) and almost all compaction results from grain rotation and sliding (Waal et al., 2015). For example, the compressibility of Frio sand is between the compressibility of Berea sand and the compressibility of unconsolidated arkosic sand (Figure 2.9c). Besides, the loading compressibility of cemented rock (Berea sandstone) is close to the unloading compressibility of unconsolidated rock (Frio sand).

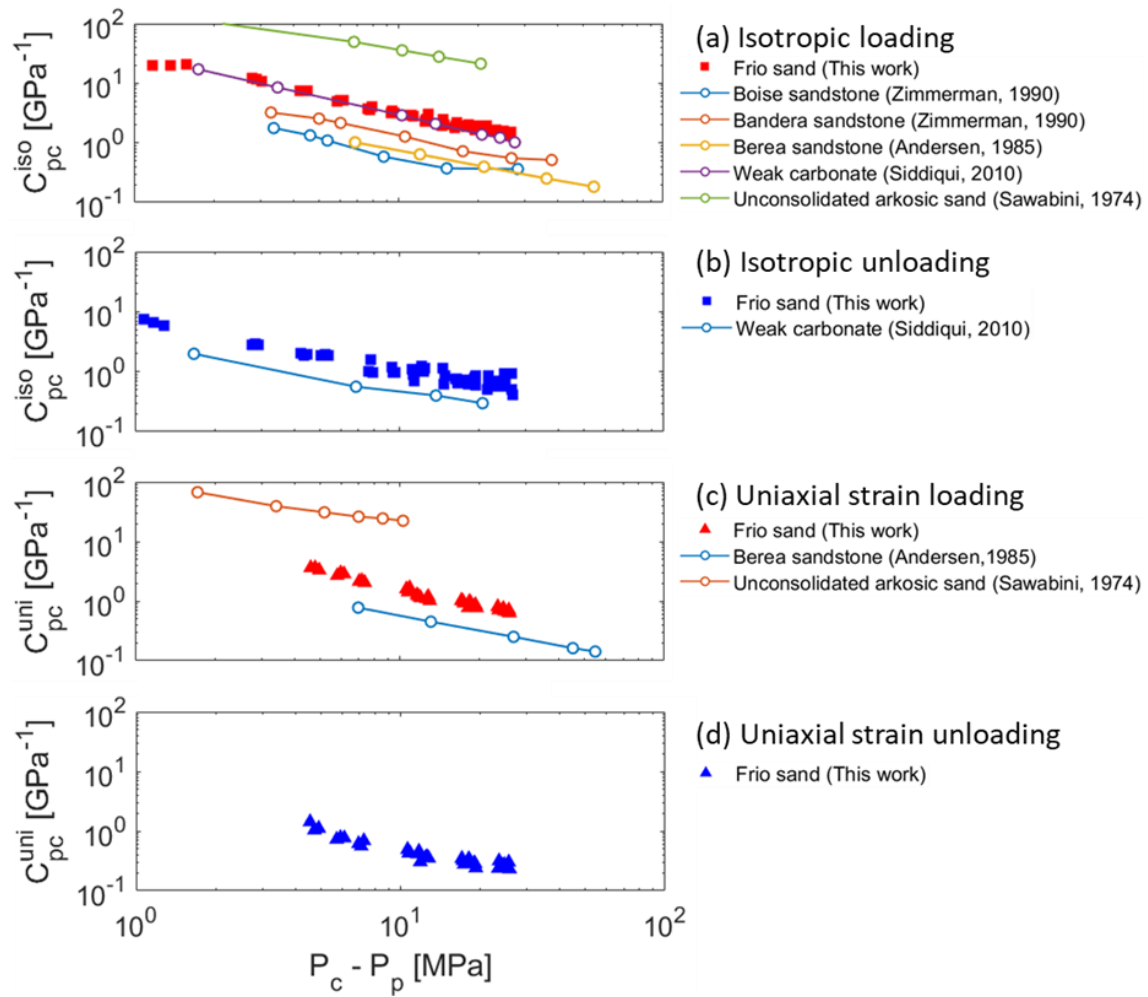


Figure 2.9: Comparison between compressibility data from the literature and our experimental data under isotropic loading, isotropic unloading, uniaxial strain loading, and uniaxial strain unloading condition. The compressibility of unconsolidated sediments depends on their fabric and is higher than the consolidated rock under the same stress condition.

2.4.6 Reservoir simulation of fluid injection into a compartmentalized reservoir

A simple model built in the reservoir simulator CMG serves to predict the pressure change induced by the process of injection. The total thickness of the model is 91.44 m divided evenly into 20 grid layers. The reservoir extends 7.94 km by 6.25 km in lateral directions (401 blocks by 41 blocks) (Figure 2.10a). The injection well is located in the

center of the reservoir with refined grid blocks. The injection activity lasts for one year at a constant injection rate of 2,472 tons CO₂ per day (surface gas rate), about 0.9×10⁶ tons CO₂/year. Two partially leaky faults with refined grid blocks are located 0.9 km from the boundary of the reservoir. The pressure at the boundary is set constant. The simulation uses conventional black-oil reservoir simulation equations without a coupled geomechanics module. The petrophysical parameters are chosen to replicate the Frio formation: $\phi = 0.34$, $k = 100 \text{ mD}$, with the depth of the reservoir top at 5,053 ft. The fault permeability and porosity were set to 0.1 mD and 0.1, respectively. We did a sensitivity study during injection to see the impact of compressibility on pore pressure build-up near the fault. Compressibility is assumed to be constant because the imposed changes in pressure are relatively small. The reservoir pressure (at the boundary of faults) increases with the ratio of pore space utilization R (Figure 2.10b), defined as

$$R(t) = \frac{V_{inj}(t)}{V_p} \quad (2.15)$$

where V_{inj} is the cumulative injection volume and V_p is the total pore volume between faults. V_{inj} is a function of time and increases by the daily injected volume each day.

The sensitivity study considers four different compressibilities ($C_{pp}^{uni_loading}$, $C_{pp}^{uni_unloading}$, $C_{pp}^{iso_loading}$, and $C_{pp}^{iso_unloading}$), which impact the degree of pressure buildup during injection (Figure 2.10b). Using isotropic compressibility underestimates the pressure increase. Even if the uniaxial strain compressibility rather than isotropic compressibility is considered, simulations should further specify which uniaxial strain compressibility is used, either loading or the unloading.

Hence, it is not conservative to use loading compressibility for predicting reservoir pressure for injection, because it underestimates the pore pressure increase. Figure 2.10b highlights that the correctness and accuracy of PVC are essential to avert fault reactivation

and loss of seal integrity due to unexpectedly high increases of pore pressure during long-term injection in geological formations (Jung et al., 2017, 2018).

The faults in the reservoir model serve as “pressure valves”, where the reservoir pressure buildup is related to how permeable the fault is. Figure 2.10c shows the simulation results with the uniaxial strain unloading compressibility and different fault permeabilities. Low fault permeability leads to high pressure increase in this partially compartmentalized reservoir. Accurate predictions of fault permeability are required for reliable reservoir pressure management. The following chapters will discuss fault permeability in details.

The typical pressure increase in CO₂ storage projects varies from 0.2 to 1 MPa. The amount of pressure buildup in the Sleipner project, in the North Sea (with the injection rate 0.9 Mt/year) was negligible since the injected saline aquifer (Utsira sandstone) is very large with few barriers to flow (Eiken et al., 2011; Verdon et al., 2013). However, the pressure increase in the Snøhvit project, in the Barents sea, was as high as 6.5 MPa after 15 months injection (with the injection rate 0.7 Mt/year) because the target Tubaen sandstone formation had low porosity and permeability and was sealed by partially leaky faults (Eiken et al., 2011; Grude et al., 2013; Hansen et al., 2013; Shi et al., 2013). The Basal Cambrian sandstone in the Quest project, in Alberta, Canada, has permeability in the order of 1,000 mD and the pressure increase after a three-year injection (1 Mt/year) has been about 0.8 MPa (Tawiah et al., 2020; Tucker et al., 2016). We use a similar injection rate of 0.9 Mt/year in our simulation. The pressure buildup is reasonable and is less than 0.5 MPa after a one-year injection with 0.03% pore space occupied by CO₂. This value is in agreement with the ratio of pore space utilization in the Sleipner project which is about ~0.003% after injecting 13 Mt CO₂ into the porous Utsira sandstone (Verdon et al., 2013).

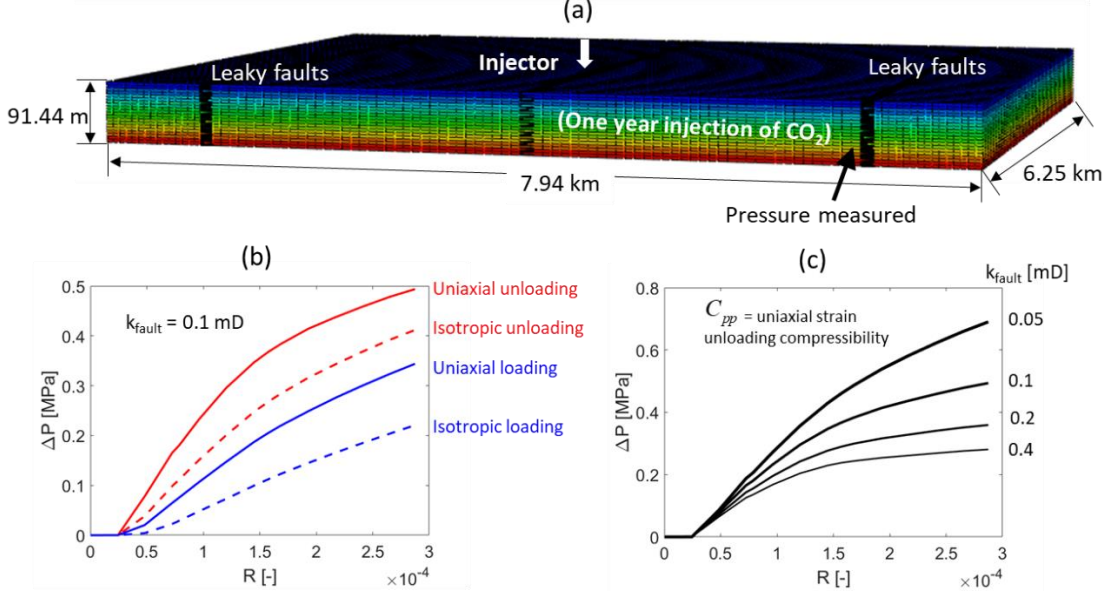


Figure 2.10: Reservoir simulation: (a) reservoir geometry; (b) reservoir pressure increase due to injection as a function of pore space utilization ratio with different compressibility values; ΔP indicates the pressure increase near the fault during CO_2 injection. Uniaxial strain unloading compressibility results in the highest pore pressure build-up; (c) reservoir pressure increase due to injection as a function of pore space utilization ratio with different fault permeabilities. Lower fault permeability leads to higher pressure increase in a partially compartmentalized reservoir.

2.5 CONCLUSIONS

We conducted triaxial loading tests on Frio sand to measure isotropic compressibility and uniaxial strain compressibility during the loading and unloading cycles. The major conclusions of this study are:

- Experimental measurements are required to quantify the uniaxial strain pore compressibility. Uniaxial strain unloading compressibility captures reservoir deformation better than conventional isotropic loading compressibility and should be used in reservoir simulation of CO_2 injection.

- Uniaxial strain compressibility is stress-dependent. The compressibility decreases with the increase of mean effective stress. The non-linear compressibility of Frio sand can be modeled with the void ratio as a function of the logarithm of mean stress.
- The uniaxial strain unloading compressibility is about one-third of the uniaxial strain loading compressibility at comparable levels of effective mean stress.
- Uniaxial strain compressibility is about one half of the isotropic compressibility at comparable levels of effective mean stress.
- Accurate compressibility measurements shed light on porosity change due to plastic deformation during fluid injection or depletion, which would be beneficial for managing the time and the extent of injection or depletion deployment.
- Incorrect compressibility input (such as isotropic and/or loading compressibility) for CO₂ storage projects will result in a lower estimation of pore pressure increase during CO₂ injection, which may underestimate the risk of fault reactivation.

Chapter 3: Multiphase CO₂-brine Transport Properties of Synthetic Fault Gouge¹

3.1 INTRODUCTION

Deep saline aquifers and depleted oil and gas fields are the primary targets for long-term CO₂ utilization and storage (Stefan Bachu, 2015; Busch et al., 2010). Structural sealing capacity is a primary criterion for evaluating potential target formations for safe CO₂ storage (Phillips et al., 2020). Faults can contribute to structural trapping and compartmentalization but also could serve as potential migration pathways (Bense et al., 2013; Cerveny et al., 2005; van der Zee & Urai, 2005; Zoback & Gorelick, 2012). Fault leakage rates in natural CO₂ analogs (flux measured at the surface) vary from 0.006 to 0.3 ton/year/m², disregarding potential losses due to carbonation dissolution reactions (Busch et al., 2010; Lewicki et al., 2006).

A variety of mechanisms contribute to fault sealing. Fault juxtaposition seal is based on juxtaposing permeable units against less permeable lithologies (Fulljames et al., 1997). The structure of the fault zone also plays an important role in defining fault sealing capacity. Fault gouge sealing includes clay smear, cataclasis or granular flow, and chemical sealing (Bense et al., 2013; Doughty, 2003; Draganits et al., 2005; Exner et al., 2013; Faulkner et al., 2010; Fristad et al., 1997; S. E. Laubach et al., 2019; Zee et al., 2003). Clay smearing involves dragging of clay into faults as shear displacement between the hanging wall and the footwall proceeds (Fulljames et al., 1997; Lehner & Pilaar, 1997). Granular flow results in the mixing of grains with different sizes and grain breakage, which leads to poorly sorted mixtures, reduction in porosity and permeability, and deformation bands (Bense et al., 2013; Johansen et al., 2005). Chemical sealing consists of processes of

¹ Zheng, X., & Espinoza, D. N. (2021). Multiphase CO₂-brine transport properties of synthetic fault gouge. *Marine and Petroleum Geology*, 129, 105054. <https://doi.org/10.1016/j.marpetgeo.2021.105054>. Xiaojin Zheng carried out experiments, wrote the original draft, and performed formal analysis.

mineral dissolution and precipitation, diagenesis, and cementation (Stephen E. Laubach, 2003; Luquot & Gouze, 2009; Rohmer et al., 2016). In some cases, the fault core may be surrounded by a more permeable damage zone due to the presence of fractures (Faulkner et al., 2010). A variety of methods help quantify fault seal potential, including: Shale Smear Factor (SSF) (Lindsay et al., 2009), Clay Smear Potential (CSP) (Fulljames et al., 1997), Generalized Smear Potential (GSP) (Doughty, 2003), Generalized Smear Factor (GSF) (Yielding et al., 1997), Shale Gouge Ratio (SGR) (Fristad et al., 1997; Yielding et al., 1997), Probabilistic Shale Smear Factor (PSSF) (Childs et al., 2007), Mechanical Clay Injection Potential (MCIP) (Zee et al., 2003) and Scaled SGR (SSGR) (Çiftçi et al., 2013). All these methods put emphasis on the properties and geometry of the fault gouge.

Natural fault gouge is usually composed of clay and sand with varying weight fractions. Thus, several studies have tried to characterize the transport properties of fault gouge based on mixtures of sand and clay. Kaolinite clay is often used as representative clay in fault gouge experiments due to its simple chemistry and non-swelling characteristics (Bos et al., 2000; Crawford et al., 2008; Ikari et al., 2009; Rutter et al., 1986; Rutter & Maddock, 1992; Zhang & Cox, 2000). The following bullets summarize the results of transport properties of fault gouge and seal rocks.

- *Permeability:* The permeability of fault gouge can decrease in excess of three orders of magnitude with increasing clay content (kaolinite) up to 40 wt% and further addition of clay results in a slower permeability reduction (Crawford et al., 2008). The logarithm of fault gouge permeability decreases by 0.5 to 1 order of magnitude when effective stress is increased by 10 MPa (Crawford et al., 2008; Delle Piane et al., 2016; Faulkner & Rutter, 2000; Wibberley, 2002). The permeability parallel to fault gouge is larger than the permeability perpendicular to the gouge (Uehara & Shimamoto, 2004). The permeability of fault gouge may increase due to smear

thinning and loss of smear continuity at large deformations (Takahashi, 2003). CO₂ penetration can cause swelling in smectite-bearing rocks, close small fractures, and thus reduce bulk permeability (de Jong et al., 2014).

- *Breakthrough pressure:* This is the pressure required to displace wetting fluids by non-wetting fluids in the largest pore throats of an interconnected pore system (Hildenbrand et al., 2002; Li et al., 2005). Caprocks (such as shale) usually have a high breakthrough pressure to inhibit fluid flow (Busch & Amann-Hildenbrand, 2013). Water saturation and pore structure play an important role in controlling breakthrough pressure (Zhao & Yu, 2017). Small pores with a high specific surface in clay-rich caprocks give rise to a high capillary entry pressure and high viscous drag that hinder CO₂ migration (Espinoza, 2017; Guiltinan et al., 2018). The breakthrough pressure of synthetic clay-rich samples ranges from 3.9 MPa to 5.0 MPa for liquid CO₂ and from 2.8 MPa to 4.6 MPa for supercritical CO₂ (Makhnenko et al., 2017). The quantitative effects of clay content on CO₂ breakthrough pressure have not been reported yet.
- *Relative permeability:* After breakthrough, permeability and relative permeability prevail as controlling parameters for fluid flow (Sperrevik et al., 2002). Effective gas permeability is generally one order of magnitude lower than water permeability for clay-rich caprocks (Duan et al., 2020; Wollenweber et al., 2010). The relative permeability of fault gouge is poorly understood. Studies on homogeneous silt and clay samples show CO₂ relative permeability is smaller than 0.2 with a water saturation of 0.7-0.9 after CO₂ breakthrough (Espinoza, 2017).

The objective of this study is to quantify the effects of grain size, porosity, and clay content on transport properties of smectite-rich fault gouge. We prepared and tested synthetic fault gouge with sand and clay from the Frio and Anahuac formations located in

the coast of the Gulf of Mexico. First, our study presents experimental results of absolute permeability, breakthrough pressure, and post-breakthrough CO₂ permeability on synthetic fault gouge. The results permit deriving quantitative relationships for all these properties as a function of clay content. Afterwards, we discuss the influence of fine-grain void ratio on absolute permeability, the implications of breakthrough pressure on maximum CO₂ column height, the effects of post-breakthrough CO₂ permeability on CO₂ migration, and the application of our experimentally-derived relationships to a realistic fault.

3.2 MATERIALS AND EXPERIMENTAL METHODS

3.2.1 Sediments and synthetic sample preparation

The sediment samples were obtained from the Frio CO₂ Pilot Test conducted in the Frio sand and capped by the Anahuac shale. The Frio site is vertically aligned with the South Liberty oil field, Texas, in a region of the Gulf Coast where there are many industrial CO₂ sources (Doughty et al., 2008). The Frio cores come from depths around 1540.15-1541.07 m (5053-5056 ft) and 1543.20-1544.12 m (5063-5066 ft), and Anahuac shale from depth 1490.41-1490.72 m (4889.8-4890.8 ft). The Frio sand is composed of moderately sorted quartz sand and minor amounts of calcite, while the Anahuac shale is primarily composed of smectite (40.4%) with minor amounts of illite (5.5%) (Kharaka et al., 2006, 2009b; Wilson & Wilson, 2014).

We attempted to replicate unconsolidated fault gouge tectonites by mixing unconsolidated sediments from Frio sand and Anahuac shale. The cores are gently broken down in a mortar (no grain crushing) and then the particles are sieved in a motorized sieve shaker with 5 sieving cycles, 3 minutes each. Then we remix the sand (and clay) manually for a period from 5 to 10 minutes. According to the proportions of clay, there are three types of synthetic fault gouge in our tests, including silty sand (SS) samples, pure sand (PS)

samples, and clayey sand (CS) samples. The homogeneous mixtures of sand and clay are re-sedimented within a cylindrical vessel, following the protocol of consolidation tests (Germaine & Germaine, 2009) and utilizing NaCl salty water (2% of salt). The term “salty water” in this study is simplified as “brine” in the context of geological conditions. The three types of samples are:

- SS samples: The SS samples are composed of disaggregated grains from the original Frio cores.
- PS samples: The PS samples exclude all the silt and clay grains (passing 125 μm sieve) from the original Frio core and preserve only the sand grains. The characteristic grain sizes are $D_{10} = 135 \mu\text{m}$, $D_{50} = 170 \mu\text{m}$, and $D_{90} = 240 \mu\text{m}$.
- CS samples: The CS samples are composed of disaggregated particles from Frio sand and Anahuac shale. The sand component is the same as PS samples. The clay components are particles from the Anahuac shale passing 88 μm sieve (mostly clay with minor amounts of silt, as proven by permeability measurements with values lower than 1 μD in the result section). The *clay content* of the CS samples is listed in Table 3.1. The sand content is equal to (1-*clay content*). The *clay content* in Table 3.1 is defined as clay weight fraction (ω_f), i.e., the mass of clay divided by the total mass of sand-clay mixture, both in dry conditions. Just one sample for each combination was prepared due to the limitations of the available field core material.

Hydration and swelling of clay minerals in deionized water or low-salinity water can result in permeability reduction (Cai et al., 2020). The permeability of Mancos shale decreases from 0.96 μD to 0.59 μD when KCl salinity is reduced from 8% to 4% (Zhang & Sheng, 2017). However, an increase in brine salinity from 1% to 15% can result in a 25% decrease in the mass of CO₂ dissolved in the aqueous phase and even lead to a decrease of permeability up to 85% in the case of salt precipitation (Falcon-Suarez et al.,

2020; Kumar et al., 2020). We used 2 wt% NaCl in the experiment as demonstrated in the literature that 2 wt% salts could possibly offer the least impact of clay swelling on transport properties (Chaturvedi et al., 2019).

The underlying assumption of this mixing method is that fault gouge is a homogeneous mixture of sand and shale. This assumption is consistent with the conventional SGR predictor, in which both clay and sand entrained into a fault are well-mixed. Fault gouge with homogeneous texture is not uncommon when slip events are minor, such as the development of Riedel shears (Otsuki et al., 2003). However, fault gouge may deviate significantly from a homogeneous mixture. The relevance of such homogeneous assumption to natural conditions is discussed in Section 4.

Table 3.1: Summary of experiments. Sample acronyms: pure sand (PS), silty sand (SS), and clayey sand (CS).

Sample ID	Clay content [-]	Permeability		Breakthrough pressure		Post breakthrough permeability	MICP
		Core holder	Consolidation device	Core holder	Breakthrough pressure cell		
PS-1	0			✓			✓
PS-2	0			✓			
PS-11	0	✓					
SS-2	0.02						✓
CS-7	0.10	✓					
CS-8	0.05	✓					
CS-9	0.20	✓					
CS-25	0.40		✓				
CS-26	0.30		✓		✓	✓	✓
CS-27	0.50		✓		✓	✓	✓
CS-28	0.20		✓		✓	✓	✓
CS-29	0.40		✓		✓	✓	✓
CS-30	0.10		✓		✓	✓	
CS-31	0.70		✓		✓		
CS-32	0.90		✓		✓		

3.2.2 Experimental methods

We tested samples with permeability $k > 0.1$ mD using a conventional core holder and samples with $k < 0.1$ mD using a consolidometer and a breakthrough pressure cell. The permeability measurement using the conventional core holder relies on the steady state method. The steady state method is not practical for ultra-low permeability measurements due to long-duration of the experiment. The consolidometer allows measuring the brine permeability of samples with high clay content during the consolidation process in a reasonable time. After consolidating samples, we moved samples to a breakthrough pressure cell (Figure 3.1). All the breakthrough pressure tests were conducted in this breakthrough pressure cell, except for the two sandy samples (PS-1 and PS-2), which were tested directly in a conventional core holder. Immediately after CO_2 breaks through the sample, we measured CO_2 permeability combining Boyle's law, Darcy's law, and the equation of state for CO_2 . The synthetic fault gouge was dried in an oven for two days after breakthrough pressure tests, and then taken for a mercury intrusion capillary pressure (MICP) test.

3.2.2.1 Core holder tests

We utilized Darcy's law to calculate permeability from conventional core holder steady-state fluid flow results. We adjusted pressure gradients to obtain the same level of effective stress for all tests (ranging from 6.4 MPa to 6.8 MPa). Hence, the reported permeability is the average of values at various flow rates. Flow rate is adjusted based on sample permeability to avoid excessive upstream pressure build-up. The range of flow rates for each sample is: (1) 5 – 25 ml/min for the sample PS-11; (2) 0.5 – 4.5 ml/min for the sample CS-8 (5% clay); (3) 0.1 – 0.3 ml/min for the sample CS-7 (10% clay); and (4) 0.01 – 0.035 ml/min for the sample CS-9 (20% clay).

3.2.2.2 Consolidation tests

The consolidometer used in this study is based on the Consolidation Apparatus (25-0402) from the ELE International Company. However, we designed a new consolidation cell to accommodate the uniaxial strain compression under high-stress conditions with two outlets for fluid outflow and diameter of 25 mm (see Appendix A4 for details).

Consolidation tests measure deformation of a brine-saturated sediment as a function of applied stress and time. The incremental stress consolidates the sediment while displacing brine from the pore space. The maximum axial stress in the consolidation test is set to 19.17 MPa to replicate the actual burial and compaction at the depth of the Frio sand cores.

Consolidation process is a coupled process between flow and volume change. The sample permeability can be derived from the strain-time curve during the consolidation process using the following equation (Germaine & Germaine, 2009):

$$k = c_v C_b \mu_f \quad (3.1)$$

where c_v is the coefficient of consolidation, μ_f is the brine viscosity, and C_b is constrained bulk compressibility. The coefficient of consolidation can be approximated as $c_v = 0.197 H_d^2 / t_{50}$, where H_d is the drainage height, defined as $H_d = (1 - \varepsilon_{50} / 100) H_0 / f$, where H_0 is the initial height, ε_{50} is the strain at 50% consolidation, and f is drainage condition factor ($f = 2$ for top and down draining boundaries). The accuracy of the determination of c_v , and therefore permeability, decreases with increasing sample permeability. The sample porosity depends on axial strain and is equal to $\phi = (\phi_0 - \varepsilon_x) / (1 - \varepsilon_x)$ (assuming negligible mineral grain deformation), where ε_x is the axial strain and ϕ_0 is the initial porosity.

3.2.2.3 Breakthrough pressure tests

The setup for measuring CO₂ breakthrough pressure is shown in Figure 3.1. A syringe pump provides constant confining pressure to the sediment sample. The syringe pumps are D-Series from the Teledyne Isco Company with $\pm 0.1\%$ pressure accuracy. A large CO₂ reservoir (volume of 1,200 cm³) provides CO₂ to a small accumulator (volume of 300 cm³) at the downstream side, which supplies CO₂ to the core holder. CO₂ comes out from the top of the core holder at atmospheric pressure into a water-filled beaker. CO₂ bubbles appear in the beaker when CO₂ breaks through the sediment sample. Pore pressure and confining pressure are recorded with a data acquisition device. The data acquisition system combines a multichannel logger (model: 34825A) controlled by BenchLink Data Logger software from Agilent Technologies Inc. The sampling frequency is 0.2 s⁻¹. The pressure transducers provided by Omega Engineering Inc. (model: MMG3.5KV5P4A0T4A5CE) can monitor pressure up to 3,500 psi.

The inner structure of the breakthrough pressure cell is presented in Figure 3.1-i. Two endcaps are placed on the top and the bottom of the synthetic sample. The top endcap connects a roll of stainless steel tubing, which accommodates different sample lengths and axial strains. The bottom endcap connects the lid of the pressure vessel. Sample and endcaps are all wrapped together with a plastic heat-shrink tube, which isolates the sample from the confining fluid. Viton membranes in traditional core holders cannot tolerate CO₂. This improved isotropic core holder allows us to use CO₂ as pore fluid and accommodates large sediment deformations when testing uncemented samples.

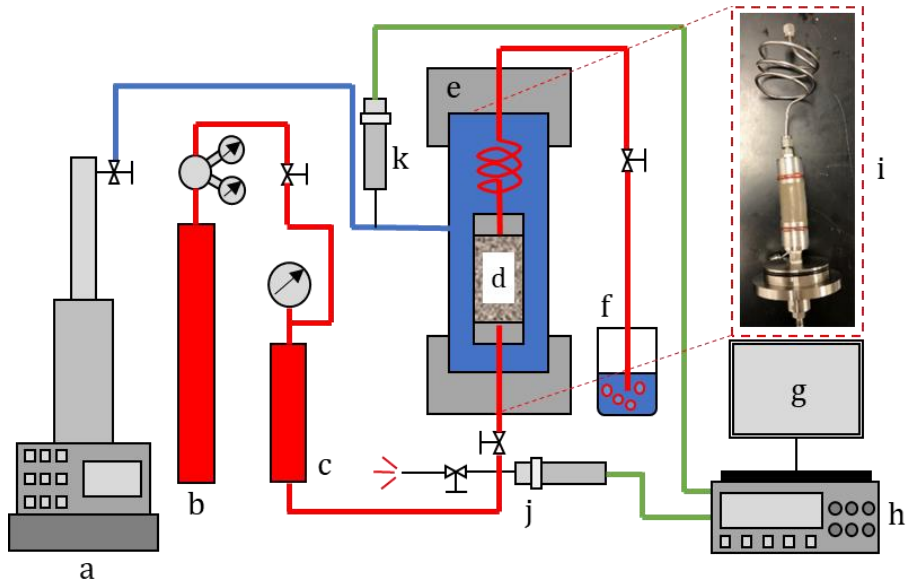


Figure 3.1: Breakthrough pressure test setup: (a) confining fluid pump (blue line); (b) CO₂ reservoir source; (c) CO₂ sub-reservoir for injecting CO₂ (red lines); (d) sediment sample; (e) isotropic core holder; (f) outlet port - may be connected to a pressure vessel; (g) data acquisition computer; (h) data acquisition hardware and electrical lines (green lines); (i) photo of inner core holder structure; (j, k) pressure transducers.

For each sample, we increase CO₂ pressure stepwise by doubling the pressure value each time (Figure 3.2a). The confining pressure is increased in each step accordingly to maintain constant effective stress. The effective horizontal stress in the Anahuac formation is approximately ~6.05 MPa assuming a hydrostatic pore pressure gradient and an effective lateral stress coefficient equal to 1/3. The effective stress in our experiments is maintained at 500 psi (3.45 MPa) for all tests to approximate the in-situ stress condition and stay within limits of the experimental device. Such action assumes negligible changes of effective stress in the caprock and prevents hydraulically fracturing the plug. The impact of effective stress on porosity and absolute permeability of fault gouge is shown in Figures 3.4a and 3.4b. The maximum upstream pressure imposed in our tests is 8.27 MPa. Thus, the maximum confining pressure is 11.72 MPa.

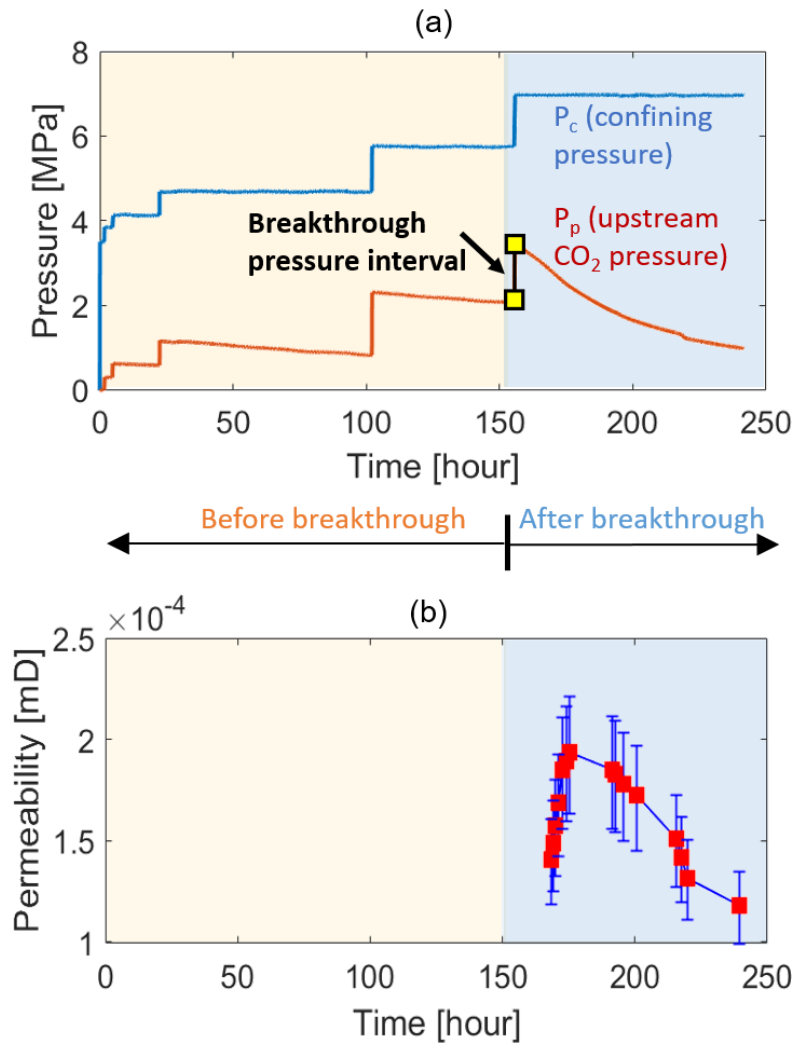


Figure 3.2: CO₂ breakthrough monitoring (example for experiment CS-29): (a) evolution of upstream CO₂ pressure P_p and confining pressure P_c ; (b) CO₂ permeability after breakthrough. We increase CO₂ pressure stepwise and monitor the experiment for CO₂ breakthrough. CO₂ flow rate increases after the immediate CO₂ breakthrough and then decreases with decreasing upstream CO₂ pressure. The yellow markers represent the measured CO₂ breakthrough pressure interval.

After each increment of pressure, we monitor the experiment for CO₂ breakthrough. If there is no breakthrough during a reasonable time (depending on the sample permeability), CO₂ pressure is doubled and the next cycle starts. The details of CO₂

pressure steps for each sample are provided in Appendix A5. The CO₂ pressure is always less than the gas-liquid equilibrium pressure (6.1 MPa at 295±1 K) except in the final stage for the samples with 70% and 90% clay. The slight decrease in CO₂ pressure before CO₂ breakthrough is probably due to minor CO₂ leaks or CO₂ diffusion through the core. However, there is no CO₂ flow at the outlet which ensures no breakthrough.

CO₂ breaks through and pressure decreases when CO₂ pressure is increased to an extent that the breakthrough pressure and percolation threshold are exceeded. The breakthrough pressure interval is delimited by the maximum pressure with no breakthrough (lower bound) and the imposed fluid pressure that causes breakthrough (upper bound) (the interval marked by yellow squares in Figure 3.2a). Small pressure increments limit the overestimation of breakthrough pressure, but result in long-time experiments.

After CO₂ breakthrough, we monitor post-breakthrough CO₂ permeability evolution by measuring CO₂ flow rate at the outlet (Figure 3.2b). Combining Boyle's law, Darcy's law, and the equation of state for a real gas, CO₂ gas permeability after breakthrough is

$$k_{CO_2} = \frac{2q_{down}\bar{\mu}LP_{down}Z_{up}}{A(P_{up}^2 - P_{down}^2)Z_{down}} \quad (3.2)$$

where q_{down} is the volumetric flow rate downstream, P_{up} and P_{down} are the upstream and downstream pressures, Z_{up} and Z_{down} are the upstream and downstream CO₂ gas compressibility factors, and $\bar{\mu}$ is the average CO₂ viscosity, L is the sample length, and A is the cross-section area of the sample. The major error source in the calculation of effective permeability is the measurement of the volumetric flow rate downstream, which is estimated through the gas volume rate coming out of the tubing. The error for other parameters is negligible. The error bar in Figure 3.2b acknowledges a ±5% error in the determination of bubble diameter.

The CO₂ relative permeability is the ratio of CO₂ effective permeability k_{CO_2} at a particular saturation to absolute permeability k :

$$k_{rCO_2} = \frac{k_{CO_2}}{k} \quad (3.3)$$

Finally, we recovered the samples and dried them in an oven at 100 °C. Experimental measurements show that extraction of bound water by drying is negligible on the determination of the percolation threshold determined from MICP measurements (Daigle et al., 2015; Yuan & Rezaee, 2019). However, capillary forces during oven-drying can induce capillary-driven cracks (Shin & Santamarina, 2011). Cementation and the presence of a sand-silt skeleton with low compressibility minimize this effect.

After samples were dried, we conducted MICP tests using a Micromeritics AutoPore IV 9500 device. A vacuum was pulled on the sample, followed by mercury injection at multiple pressures up to 60,000 psi. The analysis assumes constant contact angle for mercury equal to 130° with a liquid-vapor interfacial tension of 0.485 N/m. We inferred the MICP breakthrough pressure from intrusion curves by interpreting the first and the second inflection point.

3.3 RESULTS

3.3.1 Absolute permeability

Figure 3.3 summarizes all the results of absolute brine permeability for samples with clay content up to 20 wt% performed in the conventional core holder with the steady-state method. Permeability ranges from 253 mD (pure sand) to 0.12 mD (20 wt% clay) and decreases by about one order of magnitude when doubling clay content. The error bar in Figure 3.3 reflects variations due to measurements at various flow rates.

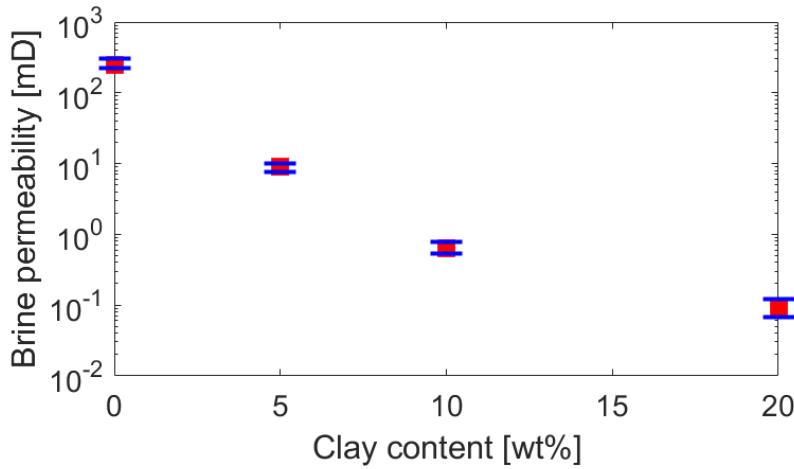


Figure 3.3: Absolute brine permeability as a function of clay content in a conventional core holder with the steady state method. The mean effective stress is between 6.4 MPa to 6.8 MPa. Absolute brine permeability decreases roughly by one order of magnitude when doubling clay content.

Figure 3.4 summarizes absolute permeability and porosity results for consolidation tests including samples with clay content ranging from 30 wt% to 90 wt%. Samples CS-28 and CS-30 with low clay content (< 30 wt%) did not exhibit typical strain vs time consolidation behavior due to rapid pore pressure dissipation; therefore, the corresponding permeability could not be obtained for these samples.

As expected, both porosity and permeability decrease with increasing axial effective stress (Figures 3.4a and 3.4b). Porosity decreases linearly with the logarithm of axial stress, and permeability exhibits a power relationship with axial stress reducing from 0.1 mD to ~0.1 μ D with increasing effective stress up to ~20 MPa. Moreover, the absolute permeability decreases by about one order of magnitude when adding 10 wt% clay, particularly when clay content is less than 70%. The logarithm of permeability and porosity has a linear positive relationship (Figure 3.4c).

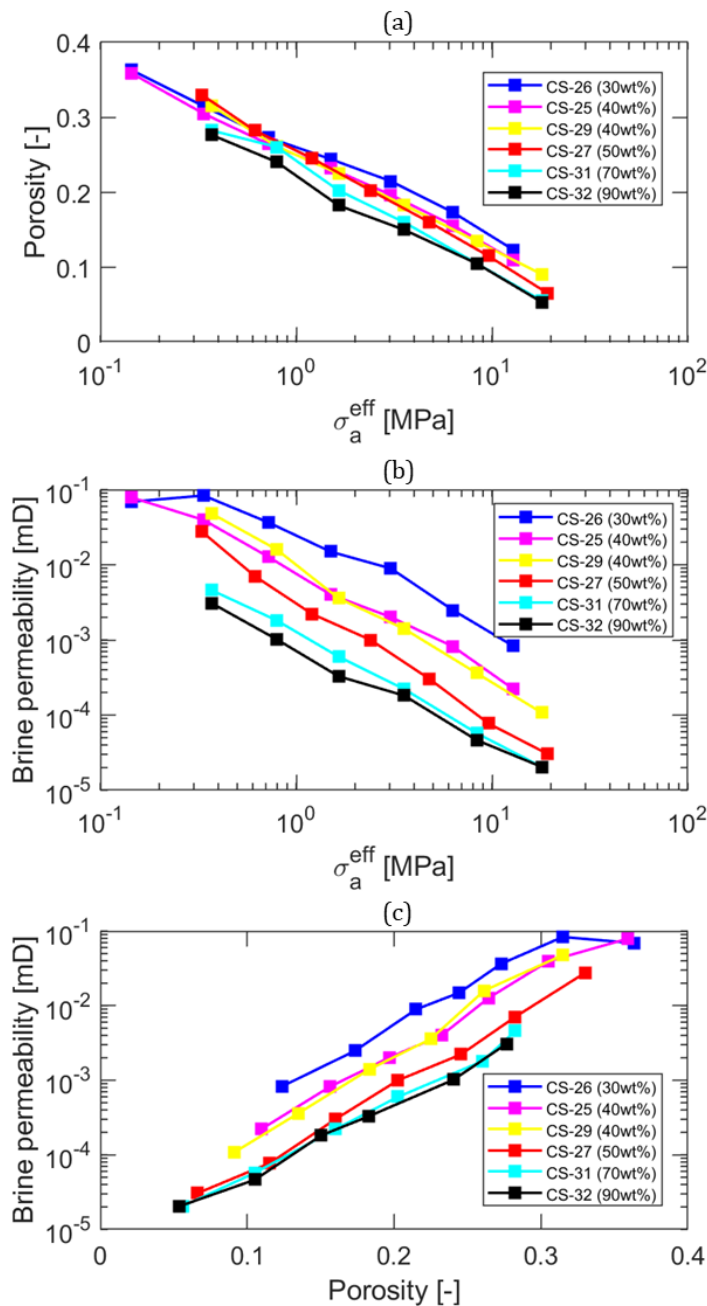


Figure 3.4: Results of consolidation tests for clay-sand mixtures: (a) porosity versus axial effective stress; (b) absolute permeability versus axial effective stress; (c) absolute permeability versus porosity. Porosity and the logarithm of permeability decrease linearly with the logarithm of axial stress. The logarithm of permeability is linearly proportional to porosity.

3.3.2 Breakthrough pressure and post-breakthrough CO₂ permeability

Figure 3.5 summarizes breakthrough pressure results of synthetic fault gouge samples with clay content ranging from 0 up to 90 wt%. The results show that the breakthrough pressure increases approximately by half order of magnitude when adding 10 wt% clay into synthetic samples. CO₂ breakthrough pressure appears to plateau at a value larger than 3 MPa for clay content over 40 wt%. CO₂ did not break through samples CS-31 and CS-32, and the symbols with an arrow in Figure 3.5 represent lower bounds of the breakthrough pressure, being the upper bound undetermined.

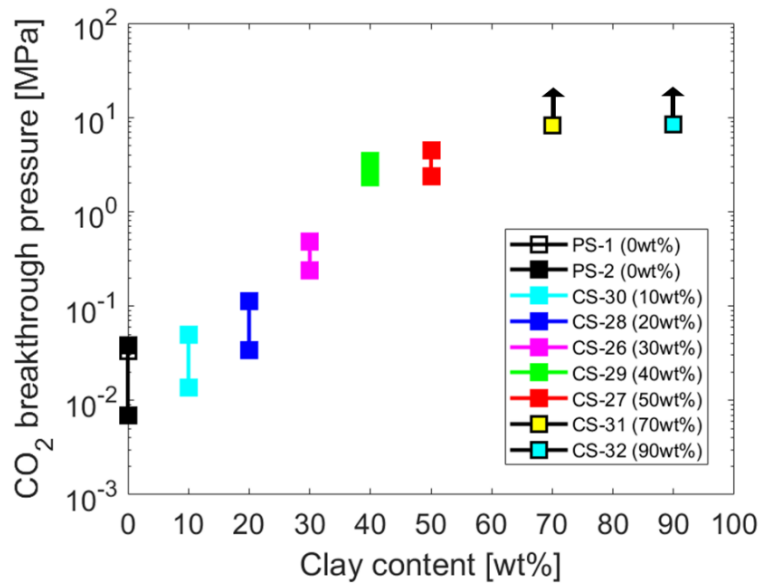


Figure 3.5: Summary of CO₂ breakthrough pressure tests. CO₂ breakthrough pressure increases by about half order of magnitude when adding 10 wt% clay up to ~40 wt% into synthetic fault gouge samples. The breakthrough pressure interval is delimited by the maximum pressure with no breakthrough (lower bound) and the imposed fluid pressure that causes breakthrough (upper bound).

The post-breakthrough CO₂ permeability decreases by about one to two orders of magnitude when adding 10 wt% of clay content into synthetic samples (Figure 3.6). The

log-log plot shows a linearly decreasing trend, which indicates that there is a power relationship between clay content and post-breakthrough CO₂ permeability. All post-breakthrough CO₂ permeability tests show an initial increase of CO₂ permeability followed by a decrease, likely due spontaneous imbibition of brine as CO₂ pressure decreases. Post-breakthrough CO₂ permeability is as low as 10 nD to 100 nD for synthetic fault gouge with clay content higher than 40% (Figure 3.6).

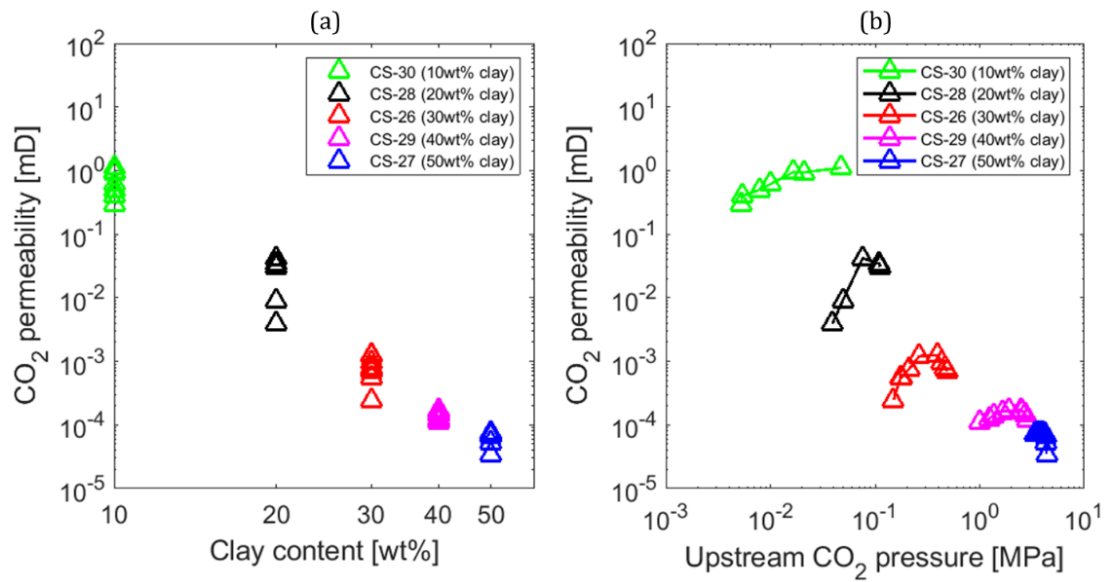


Figure 3.6: Post-breakthrough CO₂ permeability: (a) CO₂ permeability versus clay content; (b) CO₂ permeability versus upstream CO₂ pressure. The permeability decreases by about one to two orders of magnitude when adding 10 wt% of clay content into synthetic fault gouge samples. There is a power relationship between clay content and post-breakthrough CO₂ permeability.

3.3.3 Summary of permeability results in synthetic fault gouge

Figure 3.7a summarizes all the permeability results, including absolute brine permeability and post-breakthrough CO₂ permeability. The absolute brine permeability is higher than the post-breakthrough CO₂ permeability, as expected in the absence of

fracturing or leaks between the sample and the membrane. The permeability of Frio formation is between 263 and 685 mD (Jung et al., 2018; Swanson et al., 2013). The permeability of Anahuac shale (with an average clay content of 59%) is between 0.0006 and 0.0026 mD (J. Lu et al., 2015), in the range of our measurements.

Post-breakthrough CO₂ relative permeability decreases significantly with increments of clay content. The maximum CO₂ relative permeability is less than 0.1 when clay content is larger than 40 wt% (Figure 3.7b). We attempted to measure brine saturation after breakthrough but unfortunately the gravimetric method gave results with high uncertainties.

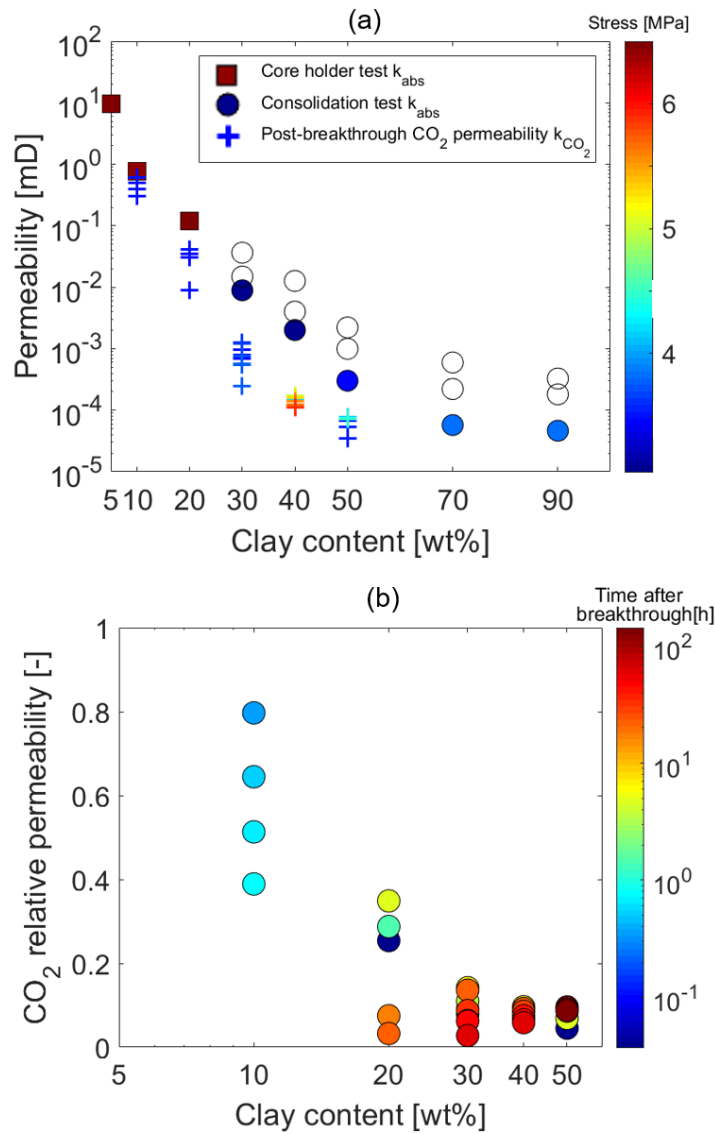


Figure 3.7: Summary of permeability tests: (a) absolute brine permeability and post-breakthrough CO_2 permeability versus clay content (the color bar indicates the mean effective stress); the hollow circles represent the permeability results during the consolidation; (b) post-breakthrough CO_2 relative permeability versus clay content; we start to record the time after CO_2 breaks through samples (the color bar indicates the time after breakthrough). CO_2 relative permeability is always less than 1 (as expected in the absence of fractures) and decreases significantly with the increase of clay content. The maximum post-breakthrough relative permeability is less than 0.1 when clay content is larger than 40 wt%.

3.4 DISCUSSION

3.4.1 Influence of fine-grain void ratio on absolute permeability

The synthetic fault gouge samples prepared in this study are composed of clay and sand. Generally, fine grains fill the space among coarse grains in a homogeneous mixture. Hence, the fluid must pass through the pore space of fine grains when fine grains percolate through the pore space left by coarse grains. The cathodoluminescence image of Barnett shale in Figure 3.8 illustrates this concept, where two large detrital quartz grains are distributed in the clay mineral matrix (Milliken, 2019). The red arrow indicates the direction of fluid flow. The red box, which contains mostly fine clay particles, is a representative volume along the fluid path. We use the fine-grain void ratio to capture the influence of fine grains in absolute permeability. The fine-grain void ratio is defined as (Guiltinan et al., 2018):

$$e_f = \frac{V_p}{V_f} = \frac{\rho_f \phi}{\omega_f \rho_s (1-\phi)} \quad (3.4)$$

where V_p is the pore volume, V_f is the volume of fine solid grains, ϕ is the bulk porosity, ω_f is the clay weight fraction, ρ_f is the density of fine grains, and ρ_s is the density of bulk solid grains. The clay volume fraction in the denominator transfers the focus from total grain solid volume into solid volume of the fine grain fraction. The fine-grain void ratio plays an important role in defining transport properties in the sand-clay system. Details about the fine-grained void ratio have already been discussed in the literature (Guiltinan et al., 2018). We use this concept in the discussion section to help interpret our experimental measurements and further illustrate the intrinsic nature of transport properties in the sand-clay mixtures.

The result shows that all absolute permeability data collapses into one main trend when plotted as a function of fine-grain void ratio (Figure 3.8), which supports the

hypothesis that permeability is mainly controlled by the fine-grain void ratio. Thus, permeability predictions of fault gouge tectonites should not rely on bulk porosity but on the porosity of the clay fraction. Grain-to-grain contacts of silt grains (silt bridging) may preserve large pores within clay and alter sediment permeability at low clay fractions (Schneider et al., 2011).

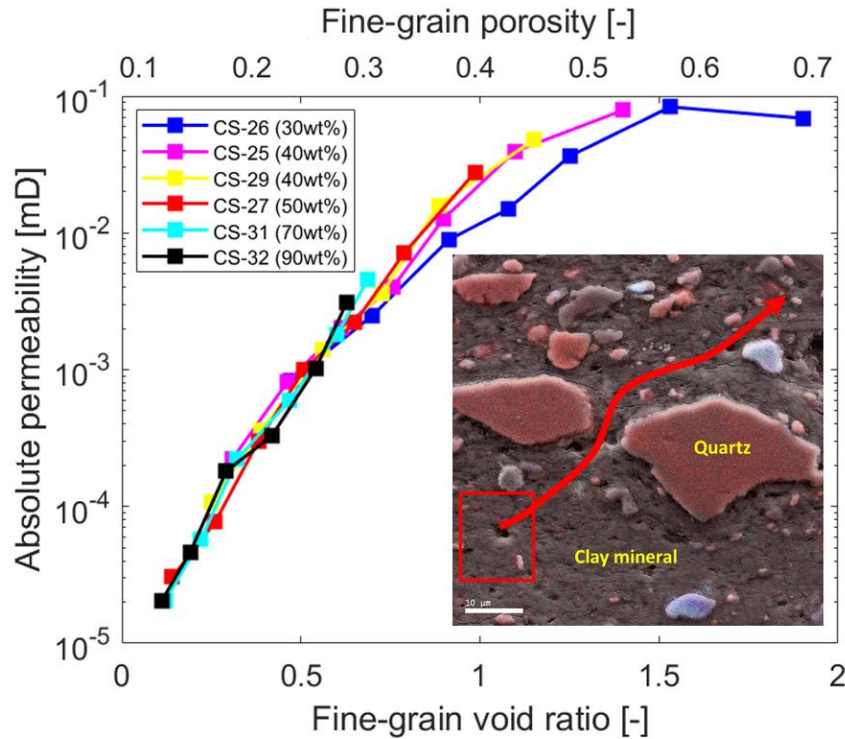


Figure 3.8: Influence of fine-grain void ratio in absolute brine permeability. The fine-grain void ratio dictates absolute permeability, instead of bulk porosity or bulk void ratio. The cathodoluminescence image of Barnett shale (a binary grain-size system with coarse sands and fine clays -after (Milliken, 2019)) shows that the porosity of packed fine grains determines transport properties.

3.4.2 Implications of breakthrough pressure on maximum CO₂ column height

The breakthrough results shown in Figure 3.5 correspond to various upstream pressures, and therefore various interfacial tensions. Hence, let us convert the results to supercritical CO₂ (scCO₂) conditions using Equation 3.5 (Peters, 2012):

$$P_{c \text{ system2}}^* = P_{c \text{ system1}}^* \frac{\sigma_{\text{system2}} \cos \theta_{\text{system2}}}{\sigma_{\text{system1}} \cos \theta_{\text{system1}}} \quad (3.5)$$

where P_c^* is the breakthrough pressure, σ is the interfacial tension, and θ is the contact angle, in systems 1 or 2. The interfacial tension of CO₂-brine depends on pressure and temperature. The experiments in this study are conducted under room temperature (about 295±1K). CO₂-brine interfacial tension decreases from ~72 mN/m and plateaus at ~25 mN/m with the increase of the pressure at T = 298 K (Kvamme et al., 2007). The measured breakthrough pressure results converted to supercritical CO₂ conditions (P = 6.89 MPa, T = 333 K), assuming negligible changes in contact angle are shown in Figure 3.9 together with data from the literature. Brine-CO₂ interfacial tension increases with temperature increase (Kvamme et al., 2007).

The breakthrough data follows an increasing trend with decreasing mean pore size; the literature data is measured through MICP and estimated by Kozeny–Carman equation (Boulin et al., 2013; Espinoza, 2017; Hildenbrand et al., 2002; Horseman et al., 1999; Li et al., 2005; Makhnenko et al., 2017) (Figure 3.9a). The results of our experimental study appear below the trends of homogeneous sediment packs and shale rocks. This deviation is likely due to the pore size heterogeneity of our mixture samples and the ability of the non-wetting phase to find the interconnected pore network with the largest pore sizes. Unlike permeability, breakthrough pressure is not a simple volume average because breakthrough pressure represents the displacement resistance in the largest interconnected

pores rather than in the overall pore space. Hence, breakthrough pressure magnifies the effect of capillary “weak” large pores (Espinoza & Santamarina, 2010).

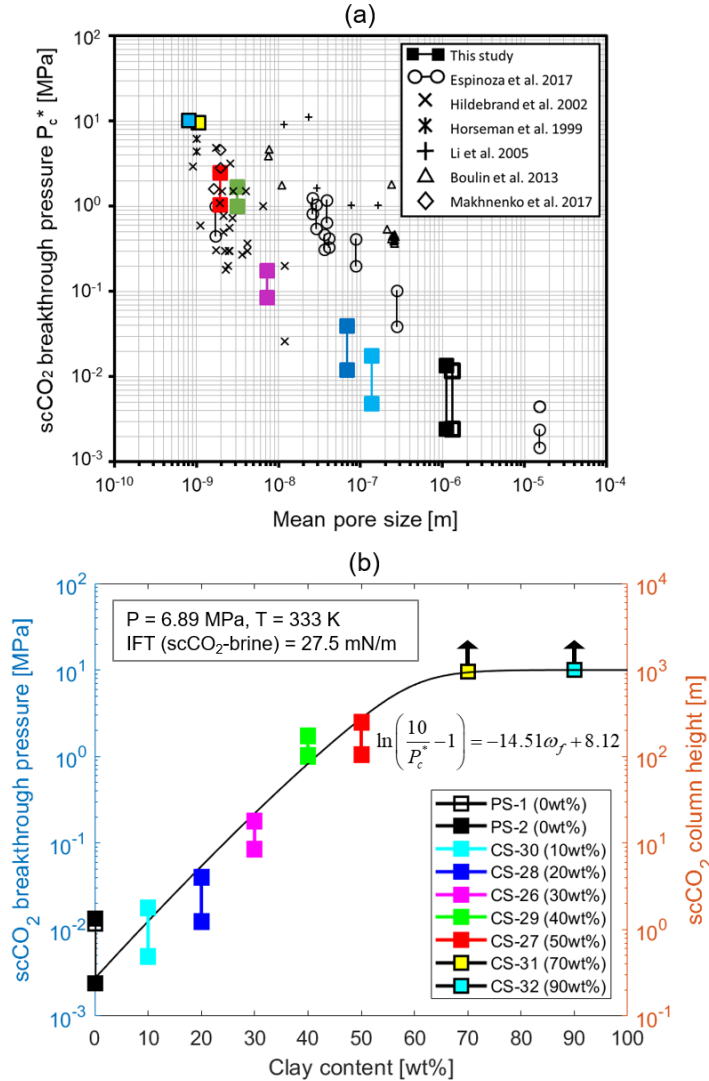


Figure 3.9: Supercritical CO₂ breakthrough pressure: (a) comparison of our date scaled to field conditions ($P = 6.89$ MPa, $T = 333$ K) with the data from the literature including field cores and homogeneous sediment samples. Breakthrough pressure is inversely proportional to mean pore size, which is calculated with the Kozeny-Carman equation as a function of porosity and permeability; (b) summary of scCO₂ breakthrough pressure for clay/sand mixtures and corresponding CO₂ column height at field conditions. The CO₂ capillary sealing capacity is proportional to clay content through an exponential-law relationship (logistic function).

Regression analysis using logistic function yields the relationship between scCO₂ breakthrough pressure and clay content as

$$P_c^* = \frac{10}{1 + e^{-14.51\omega_f + 8.12}} \text{ [MPa]} \quad (3.6)$$

This is a conservative estimation because the upper bounds of breakthrough pressure for samples with 70 and 90 wt% of clay are undetermined. Thus, the fitting on Figure 3.9b highlights the lower bound of estimated breakthrough pressure from our tests. Leaving out these values will exaggerate the increasing trend and result in an unreasonably high sealing potential for the fault gouge with high clay content. Moreover, the current fitting also honors the literature data in Figure 3.9a, in which the maximum sealing capillary pressure is around 10 MPa.

The corresponding CO₂ column height depends on buoyancy and it is equal to

$$h = \frac{P_c^*}{(\rho_w - \rho_{CO_2})g} \quad (3.7)$$

where ρ_w is water density and ρ_{CO_2} is CO₂ density. Supercritical CO₂ breakthrough pressure increases by half order of magnitude when increasing 10 wt% clay in synthetic fault gouge. The samples with clay content above 40 wt% reach an equivalent CO₂ column height of more than 100 m, which is a relatively large column of buoyant CO₂ (Figure 3.9b). Capillary pressure measurements on the Muderong Shale (dominated by interstratified illite-smectite) from the Carnarvon Basin demonstrated the capacity to contain CO₂ gas columns of 250 m (Dewhurst et al., 2002). Yielding (2002) compiled buoyancy pressure data from hydrocarbon columns at multiple locations around the world and obtained that the maximum observed sealing pressure in the Gulf of Mexico Basin was about 200 psi (equivalent to 141 m of CO₂ column).

3.4.3 Comparison with breakthrough pressure estimated through MICP

Mercury injection capillary porosimetry (MICP) tests serve frequently as proxies for estimating entry and breakthrough pressure. The main advantages of MICP tests are that they follow well-established methods, do not use brine and CO₂, and do not require core plugs but can be performed with cuttings (Amann-Hildenbrand et al., 2013). There are several terminologies available to interpret characteristic pressure from MICP results. The threshold pressure is commonly established at the inflection point of the cumulative intrusion curve, or the pressure at which the first derivative of the intrusion curve reaches a local maximum (Katz & Thompson, 1987). Instead, Dewhurst et al. (2002) define the threshold pressure as the pressure corresponding to the largest increase on the first derivative of the capillary pressure curve. The displacement pressure is analogous to the breakthrough pressure defined by Hildenbrand (2002) and represents the pressure required for nonwetting fluids to form a continuous path through the largest connected pore throats of the rock (Schowalter, 1979). It can be estimated from the MICP results as the pressure when the non-wetting phase saturation reaches approximately 10% of the rock pore volume (Schowalter, 1979). Schlömer and Krooss (1997) use a tangent line fitted to the inflection point of the cumulative intrusion curve and extrapolate the trend to the logarithmic pressure axis to find the displacement pressure. Other similar terminologies in the literature (including entry pressure, critical pressure, capillary retention pressure, and threshold displacement pressure) are available elsewhere (Gallé & Tanai, 1998; Hildenbrand et al., 2002). Notice that the displacement pressure may underestimate the breakthrough pressure by invading surface irregularities or sample preparation artifacts (Amann-Hildenbrand et al., 2013). The threshold pressure characterizes the pressure of the first inflection on the capillary pressure curve and, in the sand-clay systems, captures pore sizes in coarse sands, rather than pore sizes in the compacted clay within sand grains. We use the pressure at the

second inflection in this section and compare it with our direct breakthrough pressure measurements.

For comparison purposes, we conducted MICP tests on our samples to estimate MICP-based breakthrough pressure. The interpretation of breakthrough pressure requires a conversion from the mercury (liquid–vapor)–rock system to the CO₂–brine–rock system (Equation 3.5). The contact angle of brine on silica surfaces surrounded by scCO₂ is about 45°, and the interfacial tension of brine-CO₂ at P=6.4 MPa and T=298 K is approximately 0.025 N/m (Espinoza, 2017). Figure 3.10a shows the converted CO₂ pressure as a function of mercury saturation for all tested samples. The overall required pressure for intrusion increases with the increase of clay content, as expected. Samples with low clay content experience Hg intrusion without significant pressure increase until liquid mercury reaches small pore throats. The intrusion pressure for samples with high clay content increases gradually with liquid mercury saturation.

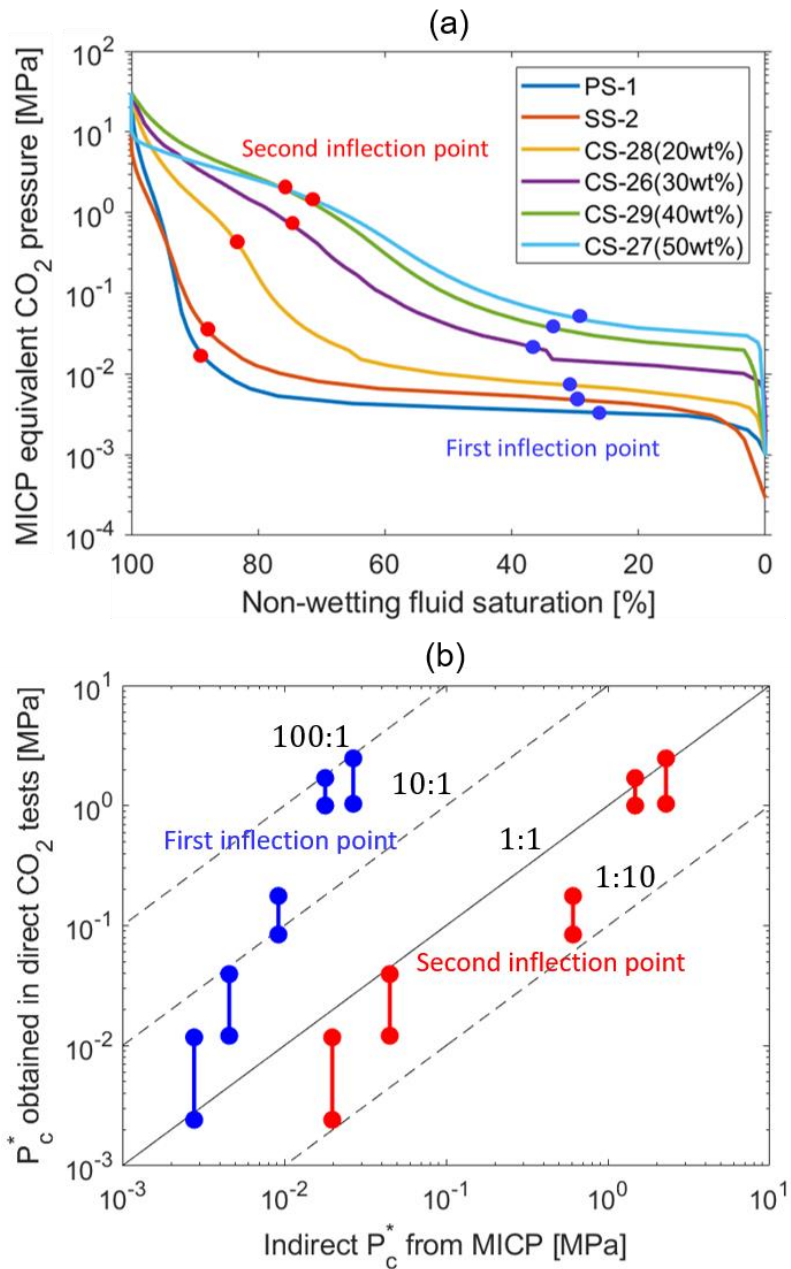


Figure 3.10: MICP results: (a) converted Hg to CO_2 pressure and saturations from MICP tests; (b) comparison between breakthrough pressures obtained from MICP and direct CO_2 breakthrough pressure measurements. The inferred breakthrough pressures from the second inflection point are similar to direct breakthrough pressure measurements.

The intrusion curves in Figure 3.10a show two inflection points. The first inflection point occurs at relatively low liquid mercury pressure. The equivalent CO₂ breakthrough pressures corresponding to the first inflection point (obtained through tangent method) for all samples are lower than 0.0345 MPa, which is one to two orders of magnitudes smaller than the values from direct CO₂ breakthrough pressure tests. The disparity may be due to voids between compacted clay and coarse sands caused during drying before conducting MICP tests, as observed in other experiments (Gallé, 2001). The values of the second inflection point range from 0.02 to 2.3 MPa and are more likely to reflect the true pore size in the compacted clay within sand pores because they yield similar results to direct CO₂ breakthrough pressure measurements. Figure 3.10b summarizes the inferred MICP breakthrough pressure from these two inflection points and the breakthrough pressure results from direct CO₂ measurements. The traditional methods using MICP results may underestimate CO₂ breakthrough pressure if the inflection point is chosen incorrectly. Reliable measurements on breakthrough pressure should be based on direct breakthrough pressure tests.

3.4.4 Prediction of fault breakthrough pressure and CO₂ permeability from SGR

Real fault gouge is much more heterogeneous than homogeneous sediments mixtures, such as our synthetic fault gouge samples. The properties of homogeneous synthetic samples are just approximations.

Likewise, it is possible to estimate CO₂ permeability and breakthrough pressure in field applications if we assume that the SGR is equal to the clay content. SGR is defined as the net clay content of rocks that have slipped past one point at a given fault throw on a fault surface (Yielding et al., 1997):

$$SGR = \frac{\sum_{f=1}^n H \cdot v_f}{T} \quad (3.8)$$

where H is the layer thickness, T is the fault throw, and v_f is the clay volume fraction, which is related to the clay weight fraction (ω_f) through $v_f = \frac{\rho_f}{\rho_s} \omega_f$. The definition of shale gouge ratio calculates an average clay fraction at each single point within a sand-shale sequence and implicitly assumes homogeneous mixtures of sand and clay. The overall permeability of a randomly distributed mixture is the geometric average of the permeability of individual components (Gutjahr et al., 1978). Therefore, fault gouge permeability can be written as (Childs et al., 2007):

$$\log k = SGR \log \frac{k_c}{k_s} + \log k_s \quad (3.9)$$

where k is fault gouge permeability, k_s is sand permeability, and k_c is clay permeability. The linear relationship between SGR and the logarithm of gouge permeability in Equation 3.9 validates our previous results of absolute permeability tests (Figure 3.7a), and the logarithm of relative permeability exhibits a linear relationship with the logarithm of clay content as is shown in Figure 3.7b. A regression analysis yields the fits between SGR and absolute permeability

$$\log k = -4.85SGR - 0.098 \quad (3.10)$$

and the relationship between SGR and relative permeability

$$k_{rCO_2} = 0.0214 SGR^{-1.30} \quad (3.11)$$

The relationship between the breakthrough pressure and clay content with a logistic function is presented in Equation 3.6. Guiltinan et al. (2018) shows the estimated permeability using Purcell's theory and direct permeability measurements with kaolinite clay content up to 100 wt%. The permeability decreases by around one order of magnitude when kaolinite clay content is less than 30%. We did regression analyses and found similar

exponential-law dependency with an exponent around -3.09. Schneider et al. (2011) reported the permeability of mixtures composed of Boston Blue Clay and silt-sized silica from uniaxial consolidation tests. The dependency of permeability on clay content with an exponent about -4.58 (when porosity is 0.4) is similar to our measurements (-4.85 in Equation 3.10). Including high porosity values has a negligible effect on regression coefficients.

We take a fault in the High Island field as an example to illustrate the application of these experimental relationships. The High Island field is an onshore oil & gas producing area, one mile from the Gulf of Mexico in Galveston County. We use the borehole shale volume of one typical well in the High Island field as our input data (Field: HIGH IS. BLK. 24L (FB-E, HI)). The interval of interest extends from 6,000 to 7,800 ft (TVD) in the Lower Miocene, which is composed primarily of regressive coarse-grained, porous, and permeable sandy formations, with overlying shales serving as regional seals (T. A. Meckel et al., 2017). We generate a simplified sand-shale sequence from a gamma-ray emission log in a well assuming a cutoff value of shale volume ($V_{sh} = 75\%$), for which $V_{sh} > 75\%$ is 100% shale and $V_{sh} < 75\%$ is assumed as 100% sand. The fault throw for this example fault is 300 ft. The SGR definition (Equation 3.8) and fitted equations (Equations 3.10, 3.6, and 3.11) permit the estimation of SGR, absolute permeability, breakthrough pressure, and relative permeability along faults (Figures 3.11b, 3.11c, 3.11d, and 3.11e). The figure indicates that the weakest point in this fault occurs at the depth around 2,100 m where gouge absolute permeability is 0.1 mD with a low breakthrough pressure.

As mentioned in the introduction, fault sealing can be a result of juxtaposition, clay smear, cataclasis or granular flow, and chemical sealing (Cerveny et al., 2005). This study only addresses the effect of clay smear on fault sealing. Other minerals (such as calcite precipitation) do have the potential to seal faults but are out of the scope of this study. The

estimation of transport properties using synthetic fault gouge with various clay content assumes the clay content as a result of smearing is the dominant factor controlling the fault sealing potential.

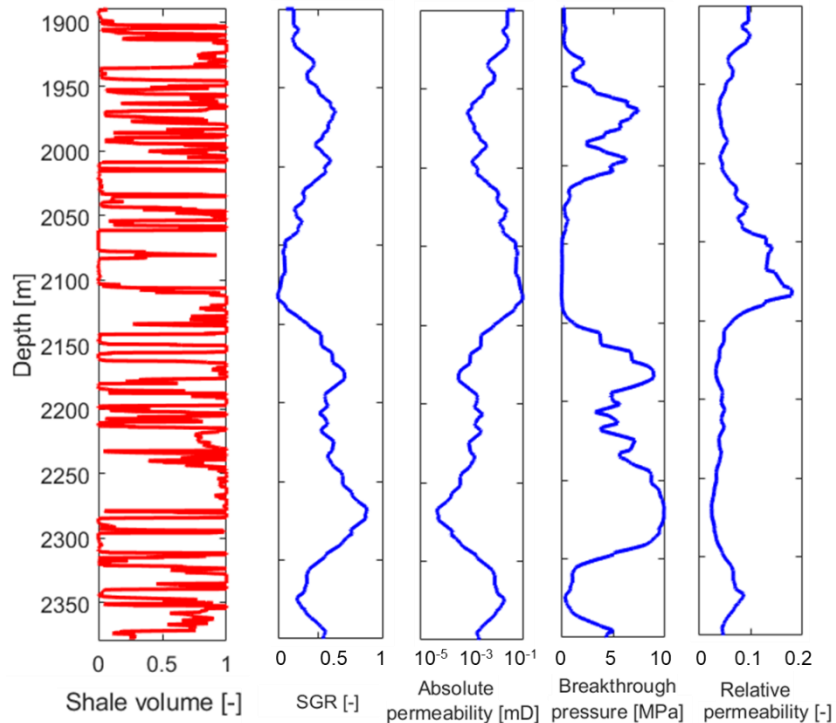


Figure 3.11: Field application of our model in the High Island field: (a) shale volume distribution; (b) SGR; (c) predicted absolute permeability; (d) predicted CO₂ breakthrough pressure; (e) predicted CO₂ relative permeability. The predicted properties are based on relationships found in this work.

Clay smears extend along the faulting direction during the initial increase of fault throw, and will breach if the fault throw is larger than a critical value (Kettermann et al., 2017; Noorsalehi-Garakani et al., 2013, 2015; Schmatz et al., 2010; Schmatz & Urai, 2006). Clay smears will be placed somewhere along faults after the smear loses its continuity, which will add significant uncertainties to fault structural trapping. Different juxtaposition scenarios and different modes of clay smears (continuous or truncated) alter

the amount and distribution of clay in fault gouge and thus change transport properties within fault zones (Faerseth, 2006). The assumptions of homogeneous clay-sand mixtures adopted in this study and in the SGR method have clear limitations. Real fault gouges are heterogeneous and the corresponding models should incorporate clay smear and potential breaching. Such modifications will be discussed in Chapter 4.

3.5 CONCLUSIONS

We conducted absolute permeability tests, breakthrough pressure tests, and post-breakthrough CO₂ permeability tests on synthetic fault gouge samples with various clay contents (mostly smectite). The major conclusions of this study are:

- There is an exponential-law relationship between clay content and fault gouge absolute permeability. Fault gouge permeability decreases about one order of magnitude when adding 10 wt% clay, which indicates clay content has a large influence on fault gouge sealing capacity.
- Fault gouge porosity and the logarithm of fault gouge permeability decrease linearly with the increase of the logarithm of axial stress. The logarithm of permeability and porosity have a linear positive relationship.
- The fine-grain void ratio dictates absolute permeability, instead of bulk porosity or bulk void ratio.
- The breakthrough pressure increases approximately by half order of magnitude with increments of 10 wt% clay into synthetic fault gouge. The measured CO₂ breakthrough pressure is larger than 3 MPa (equivalent to a 100 m CO₂ column) when clay content is over 40 wt%.

- The maximum CO₂ relative permeability is less than 0.1 when clay content is larger than 40 wt%. Future experiments should use additional methods, such as X-ray monitoring, to attempt measuring phase saturations during and after breakthrough.
- It is not trivial to choose the interpretation method for the estimation of breakthrough pressure using MICP. The displacement pressure or threshold pressure inferred from different inflection points may underestimate actual CO₂ breakthrough pressure.
- The fitted equations from experimental results demonstrate the potential to estimate transport properties of fault gouge using clay content. The predicted CO₂ permeability and CO₂ breakthrough pressure can serve as an alternative to validate field measurements.

Chapter 4: Stochastic Quantification of CO₂ Fault Sealing Capacity in Sand-Shale Sequences

4.1 INTRODUCTION

Geological CO₂ storage is a potentially effective strategy for mitigating the release of CO₂ into the atmosphere (Nicot, 2008). Safe CO₂ storage relies on structural barriers with low permeability and high breakthrough pressure, such as caprocks and sealing faults. Sealing mechanisms of faults in sand-shale sequences include sand-shale juxtaposition and clay smears (Cerveny et al., 2005). Different juxtaposition scenarios, the amount and type of clay deposits in the stratigraphic interval, and different modes of clay smears (continuous or truncated) alter the amount and distribution of clay in fault gouge and thus change transport properties within fault zones (Faerseth, 2006). The maximum attainable CO₂ plume height results from a balance of CO₂ buoyancy pressure and sealing properties across faults (Gao et al., 2014; Takahashi, 2003).

Figure 4.1a schematically presents a faulted sand-shale sequence with a varying fault throw along the strike. Three different lithology contacts are possible: sand-sand (blue), shale-shale (red), and shale-sand (purple) (McKie et al., 2010). The classic triangle diagram in Figure 4.1b can describe contact scenarios between the hanging wall and the footwall (Allan, 1989). The sand-sand contacts are preferential fluid migration paths over the shale-shale and the shale-sand contacts.

Ductile clay may be entrained into a fault and smeared on the contact surface as the fault throw increases (Çiftçi et al., 2013; Doughty, 2003). Clay smears (marked in yellow in Figure 4.1b) extend along the faulting direction with increasing fault throw (Kettermann et al., 2017), and will breach if the fault throw is larger than a critical value (Noorsalehi-Garakani et al., 2013, 2015; Schmatz et al., 2010; Schmatz & Urai, 2006). Figure 4.1c shows an actual example of clay smear along a fault plane. The shale gouge ratio (SGR),

the shale smear factor (SSF), and the probabilistic shale smear factor (PSSF) models attempt to quantify changes of fault transport properties with increasing throw.

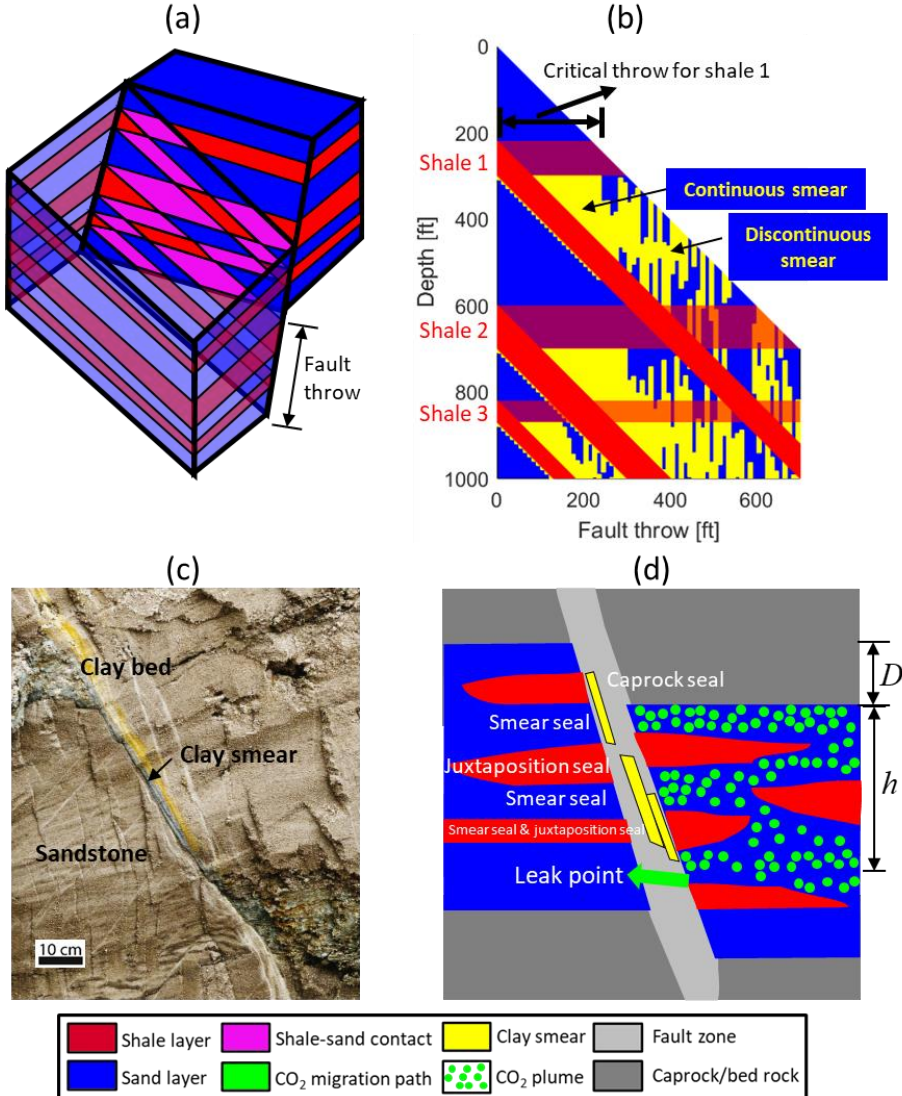


Figure 4.1: Juxtaposition seal and clay smear fault sealing mechanisms and their implications on maximum CO₂ column height in a sand-shale sequence: (a) schematic diagram of a hanging wall and a footwall with increasing fault throw; (b) triangle diagram showing clay smear distribution in faults; smears become discontinuous when fault throw is larger than a critical throw; (c) an example of clay smear in a fault in Hambach mine, Germany (Vrolijk et al., 2016); (d) fault sealing mechanisms at different locations and trapped CO₂ column with plume on the hanging wall side.

SGR is widely used in the oil and gas industry to quantitatively predict the fluid flow properties of faults. At any point along a fault surface, SGR is defined as the net clay content that has passed that point (Yielding et al., 1997):

$$SGR = \frac{\sum_{i=1}^n T_i \times (v_f)_i}{D} \quad (4.1)$$

where D is fault throw, T_i is the thickness of shale layer i , and $(v_f)_i$ is the clay volume fraction of shale layer i . The definition of SGR implicitly assumes a perfect mixing of clay across faults and neglects many geological processes, including clay smears in sand-shale sequences. Yielding (2002) summarized measurements of the proportion of fault plane covered by clay smears and suggested that most smears would breach when $SGR > 0.2$. The effective shale gouge ratio algorithm (ESGR) introduces a weighting function applied to the thickness of shale layers and assumes that a greater contribution of clay in faults is derived from the units closer to the point of interest (Freeman et al., 2010).

Lindsay et al. (2009) proposed the shale smear factor (SSF) to constrain the likelihood of shale smear continuity. SSF is defined as the ratio between fault throw D and shale layer thickness T (Equation 4.2).

$$SSF = \frac{D}{T} \quad (4.2)$$

Lindsay et al. (2009) suggested that clay smears may breach for $SSF > 7$, based on a study of 80 faults at Round O Quarry, Lancashire, UK. The critical fault throw and the Critical Shale Smear Factor (SSFc) depend on the plasticity of the smeared clay and are defined as the fault throw and SSF at the onset of smear breaching. Hence, clay smears extend continuously when $SSF < SSFc$ and breach when $SSF > SSFc$. Clay smears often maintain their length and displace along faults after the smear loses its continuity. When $SSFc$ is exceeded for a single clay smear, the probability of encountering a leak point

between its source layer and cut-off is determined by the Probabilistic Shale Smear Factor (PSSF) (Childs et al., 2007):

$$PSSF = 1 - \frac{T(SSF_c - 1)}{D - T} \quad (4.3)$$

This probabilistic approach to evaluating continuity of clay smears does not focus on details of individual realizations of probabilistically placed shale smears, but rather on the average properties.

The presence of clay smears significantly affects fault structural trapping. Consider a CO₂ plume within a sand-shale sequence reaching a fault, as shown in Figure 4.1d. The plume can be trapped by (1) the caprock, (2) clay smears, and (3) juxtaposition seals (Vrolijk et al., 2016). A leak point caused by discontinuous clay smears may not necessarily be a CO₂ migration path if a sand layer is juxtaposed with a shale layer. Likewise, a sand-sand contact may not necessarily indicate a migration path if clay smears occur at that location. The leak points available for fluid migration are the locations where the sand juxtaposes with the sand without clay smears. Buoyant CO₂ would tend to migrate through the first leak point it encounters as it starts to accumulate beneath a caprock (Childs et al., 2007). Hence, the determination of CO₂ column height and fault sealing capacity requires reliable prediction of the location and distribution of these leak points.

There are two possible scenarios for the accumulation of CO₂ at a fault, one with CO₂ accumulating from the side of the footwall, in which caprock thickness plays an important role in predicting CO₂ column height, and the other one with CO₂ accumulating from the side of the hanging wall, in which the juxtaposition of thin sand-shale layers and clay smears control fault sealing capacity. This study focuses on the second scenario (Figure 4.2).

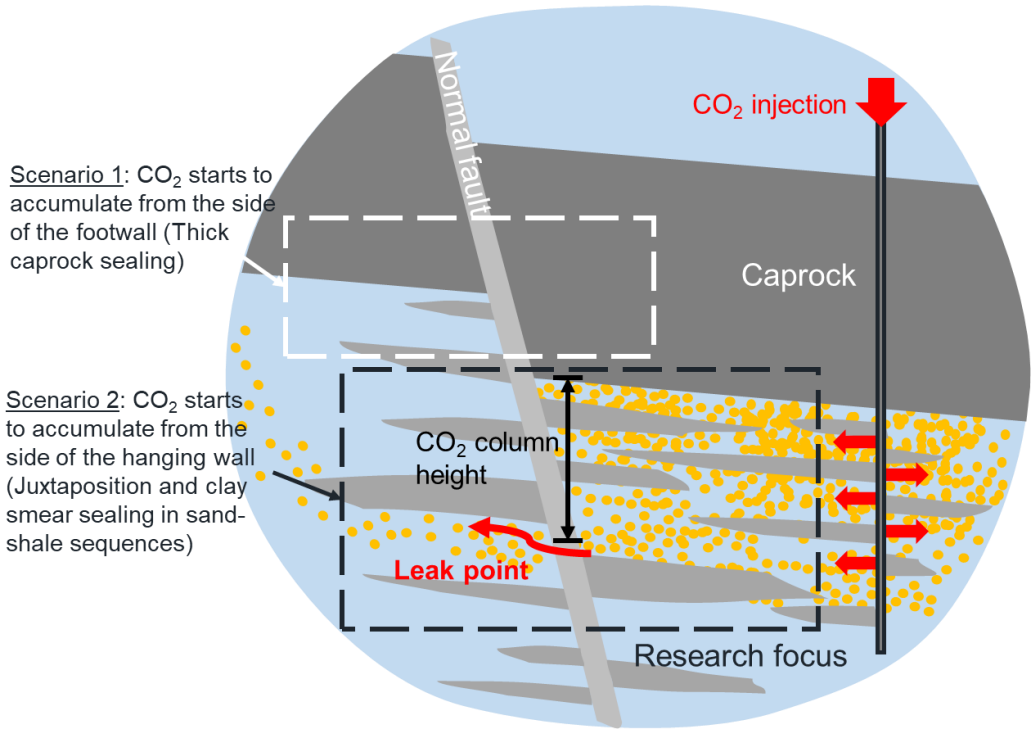


Figure 4.2: Possible scenarios for the accumulation of CO₂ at a fault: accumulation from the side of the footwall, and accumulation from the side of the hanging wall (focus of this study).

This study investigates CO₂ fault sealing capacity through stochastic realizations of clay smears as a function of fault throw. The methodology section presents the procedures to determine column height using the SGR-based and PSSF-based methods as a function of fault throw. Implicit assumptions of the model include: (1) normal faulting with dip slip only; (2) constant fault throw with depth; (3) a single planar fault plane; (4) constant stratigraphy; (5) no fault growth, fault damage, and diagenetic effects. The results section shows an application example using borehole geophysical data from the High Island field on the coast of the Gulf of Mexico, comparing CO₂ column heights predicted by the SGR-based and PSSF-based methods. A sensitivity test on critical shale smear factor (SSFc) investigates how the mechanical properties of clay smears alter CO₂ column height.

Finally, we use the proposed stochastic method to analyze the data from literature and make conclusions about the uncertainties in the prediction of maximum CO₂ column height and the validity of the PSSF-based method.

4.2 METHODOLOGY

4.2.1 Geological settings

The continental shelf of the northwestern Gulf of Mexico provides regionally extensive geologic aquifers exceptionally advantageous for CO₂ storage with abundant available geological data (Kharaka et al., 2009a). The Miocene stratigraphy along the Texas Gulf Coast is composed primarily of regressive coarse-grained, porous, and permeable sandy formations, with overlying shales serving as regional seals (T. A. Meckel et al., 2017). The High Island field is an onshore oil & gas producing area, one mile from the coast of the Gulf of Mexico in the southeastern Galveston County. In this study, we use the borehole gamma ray readings (shale volume) of one typical well in the High Island field as an example (Field: HIGH IS. BLK. 24L (FB-E, HI)). The interval of interest extends from 6,000 to 7,800 ft (TVD) in the Lower Miocene overlain by the Amphistegina Chipolensis (Amph. B) Shale. This sand-shale sequence has a maximum fault throw of 500 ft as observed in seismic sections.

Shale is usually more radioactive than sand or carbonate, and the gamma ray log can be used to calculate shale volume using the equation $V_{sh} = \frac{GR - GR_{min}}{GR_{max} - GR_{min}}$ (Usman & Haris, 2019), where V_{sh} is the shale volume, GR_{min} is the minimum value of the gamma ray log, GR_{max} is the maximum value of the gamma ray log, and GR is the reading of the gamma ray log at a given depth. We generated a simplified sand-shale sequence from a gamma ray emission log in a well from the High Island field assuming a cutoff value of

shale volume ($V_{sh} = 75\%$), for which $V_{sh} > 75\%$ is 100% shale and $V_{sh} < 75\%$ is assumed as 100% sand. The result is shown in Figure 4.3a, where thick shaly intervals prevail at the depth around 7,300 ft and thick sandy intervals prevail at the depth around 6,800 ft.

4.2.2 Prediction of CO₂ column height using the SGR-based method

CO₂ migration across faults requires the buoyancy pressure to exceed the CO₂ breakthrough pressure at the fault gouge (Hildenbrand et al., 2002). Experiments on synthetic fault gouge samples (mixtures of unconsolidated Frio sands and smectite-rich Anahuac shale) suggest a relationship between scCO₂ breakthrough pressure $P_{breakthrough}$ (MPa) and clay weight fraction ω_f [-] as follows (Zheng & Espinoza, 2021)

$$P_{breakthrough} = \frac{10}{1 + e^{-14.51\omega_f + 8.12}} \quad (4.4)$$

The weight fraction ω_f can be converted into the clay volume fraction v_f with the relationship $v_f = \frac{\rho_f}{\rho_s} \omega_f$, where ρ_f is the density of fine grains, and ρ_s is the density of bulk solid grains. Here we approximate clay volume fraction as the value of SGR, which can be easily obtained through its definition (Equation 4.1) if the stratigraphic column and clay volume fraction are available.

The buoyancy pressure $P_{buoyancy}$ within a continuous CO₂ plume is

$$P_{buoyancy} = (\rho_w - \rho_{CO_2}) g \Delta h \quad (4.5)$$

where ρ_w and ρ_{CO_2} are the brine mass density and the CO₂ mass density, g is gravity, and Δh is the net height of the CO₂ column.

The calculated CO₂ breakthrough pressure (Equation 4.4) depends on clay content (SGR) and fault throw (Figure 4.3c). Figure 4.3d shows an example with a CO₂ accumulation starting underneath the caprock with increasing buoyancy pressure (Equation 4.5), and with a fault throw of 300 ft. The height of the CO₂ column will keep increasing

until the buoyancy pressure line contacts the breakthrough pressure line. This contact point is the across fault migration point for a CO₂ plume, where the buoyancy pressure maintains a balance with the breakthrough pressure. Such point also requires sand-sand contact window otherwise shale juxtaposition will prevent fluid flow across the fault. The CO₂ column height in this case is about 100 ft.

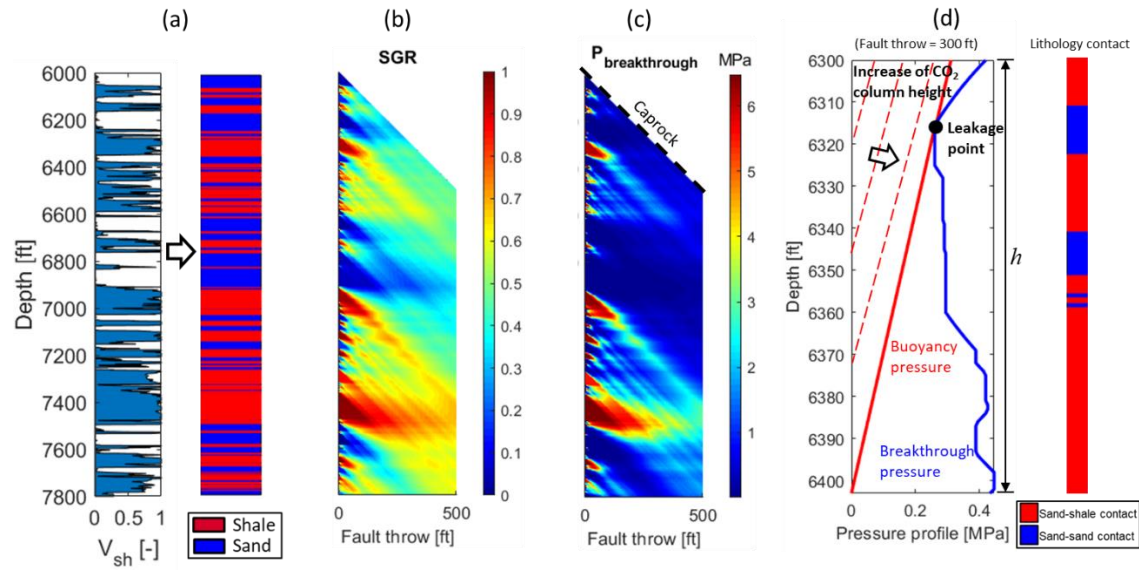


Figure 4.3: Determination of CO₂ column height using the SGR-based method: (a) stratigraphic profile of a sand-shale sequence in the High Island field; (b) SGR distribution in the triangle diagram; (c) breakthrough pressure distribution in the triangle diagram using Equation 4.4; (d) an example for CO₂ column height determination with 300 ft fault throw. CO₂ column height stops increasing once the buoyancy pressure line contacts the breakthrough pressure line. This is the maximum CO₂ column height. Leak points are not allowed where sand and shale juxtapose.

4.2.3 Prediction of CO₂ column height using the PSSF-based method

Let us assume that all sand-shale juxtapositions and clay smears have a large breakthrough pressure and the migration occurs only through sand-sand contacts and breached sections. Figure 4.4 shows a graphical application example with 16 sand/shale

layers distributed from the depth of 6,000 ft to 7,000 ft with a 150 ft fault throw to illustrate the workflow.

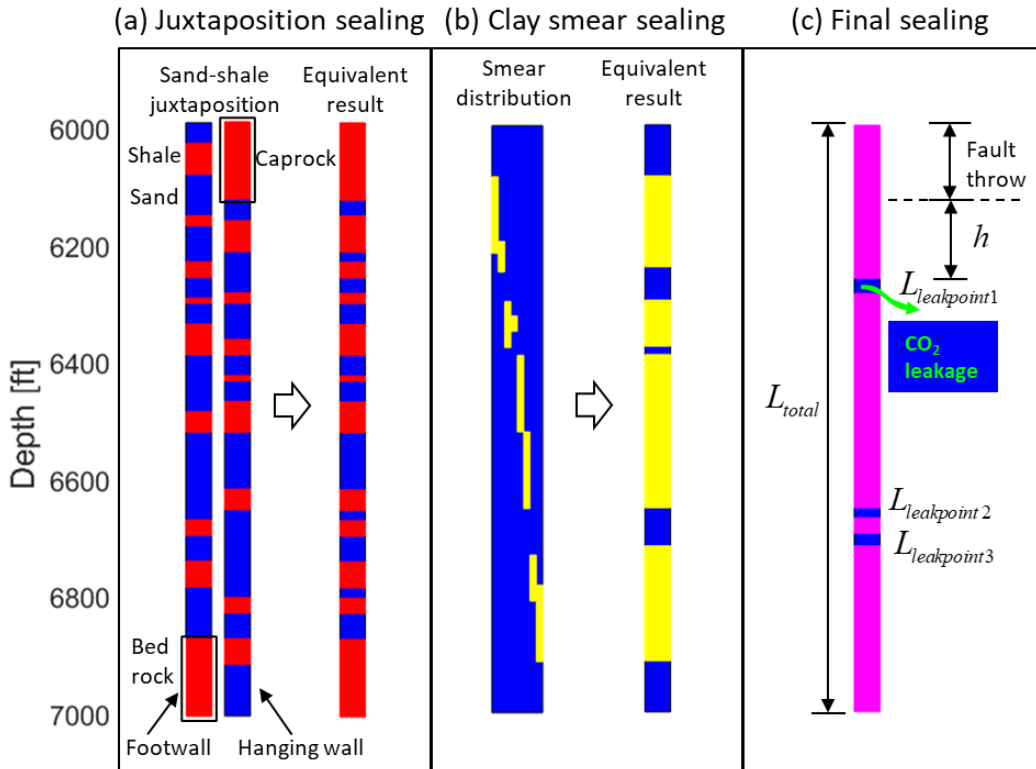


Figure 4.4: Workflow for determination of CO₂ column height including clay smears from the PSSF-based method: (a) result of juxtaposing the hanging wall with the footwall; (b) stochastic clay smear distribution within the fault; the blue intervals represent the breaches and the yellow intervals represent the smears (SSF_c is assumed to be 3 in this case); (c) final leak point in the fault by combining juxtaposition sealing and clay smearing sealing; the blue intervals represent leak points and the pink intervals represent seals. The position of the closest leak point to the caprock determines the maximum attainable CO₂ column height, assuming migration occurs through across-fault breaches only.

The determination of CO₂ column height follows these steps:

1. *Juxtaposition seal determination.* The juxtaposition of a hanging wall and a footwall in the sand-shale sequence yields three contact scenarios, in which the

sand-sand contact is colored in blue, while the other two contacts are colored in red (right-side column in Figure 4.4a). There is only one solution to this step for a given fault throw. This step assumes all fault throw occurs along a single slip plane or shear zone.

2. *Clay smear determination.* Clay smears extend downwards along the fault from the footwall with the increase of fault throw. The maximum length of each smear is $T(\text{SSFc}-1)$, where SSFc depends on the clay ductility. The smear will maintain its length after breaching. After this point, we set the smear location following a normal random distribution between the depths of the shale source on the footwall and the hanging wall. The new smear location caused by an increment of fault throw depends on the previous location, with center coinciding with p_{50} of a normal distribution and bounds set by the fault throw increment and the parent shale in the footwall and hanging wall (Figure 4.5). Figure 4.4b shows an example, with the overall smear distribution along the fault at a given fault throw.
3. *Leak point determination:* The presence of clay smears in faults produces six different contact scenarios across faults, including (1) sand-breath-sand, (2) sand-smear-sand, (3) sand-breath-shale, (4) sand-smear-shale, (5) shale-breath-shale, and (6) shale-smear-shale. The shale has the strongest sealing capacity while the sand has the weakest sealing capacity. Clay smears can be nearly 100% shale and therefore their sealing capacity can be as high as that of the parent shale (Yielding, 2012). Therefore, the across-fault sealing capacity ranking of these six contacts is $\text{sand-breath-sand} < \text{sand-smear-sand} < \text{sand-breath-shale} < \text{sand-smear-shale} < \text{shale-breath-shale} < \text{shale-smear-shale}$, where the sand-breath-sand contact is the primary migration path. We assume the sand-breath-sand contact is the leak point for fluid flow and any other scenarios inhibit fluid flow across faults. The final

distribution of leak points in Figure 4.4c shows three leak points located at different depths. The closest leak point to the caprock would serve as the migration path for accumulating CO₂ and determine the CO₂ column height as the distance between such leak point and the bottom of the caprock (Yielding, 2012). The CO₂ column height is denoted as h in Figure 4.4c and is equal to 150 ft in this example.

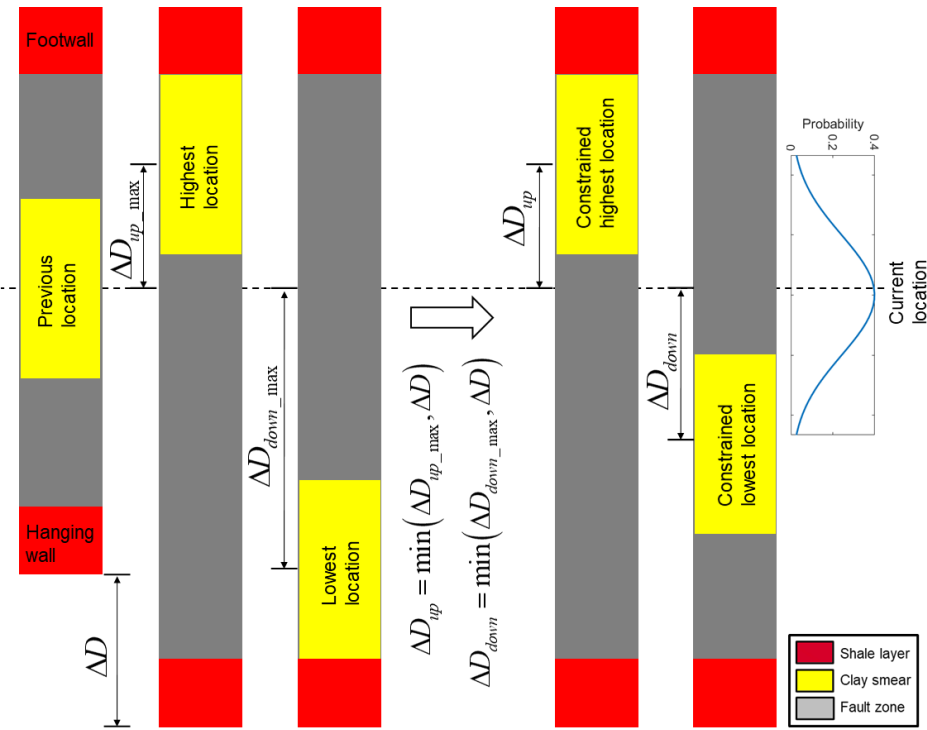


Figure 4.5: Stochastic distribution of clay smear location: the location of clay smear depends on the previous location and complies with a normal distribution within a range limited by the increment of fault throw.

We define the “seal ratio” as the ratio between the total length of the interval of interest minus the length of leaking intervals and the total length, in order to describe the proportion occupied by the leak sections in the fault zone:

$$Seal\ Ratio = \frac{L_{total} - \sum_i^N L_{leak_point}}{L_{total}} \quad (4.6)$$

The fault zone is fully occupied either by juxtaposition seal or clay smears when the seal ratio is equal to 1. A small seal ratio indicates the existence of numerous leak points for fluid migration.

4.3 RESULTS

In this section, we apply the SGR-based and PSSF-based methods to predict CO₂ column height as a function of fault throw using a sand-shale sequence from the High Island field. Fault throw increases from 0 to 500 ft with an interval of 2 ft in our simulation. Increases of fault throw in active faults happen over geological time, depend on the basin and tectonic setting, and can be quite variable within the same basin.

4.3.1 SGR-based column height prediction

The SGR-based method results show that (1) CO₂ column height is overall proportional to SGR and therefore breakthrough pressure (the SGR value in the color bar corresponds to the leakage point); (2) each fault throw results in only one prediction of CO₂ column height; and (3) CO₂ column height has an overall increasing trend with increasing fault throw (Figures 4.6a-4.6b).

The breakthrough pressure across faults derived from the SGR-based method is consistently low in the 100 ft underneath the caprock (Figure 4.6a), and thus the CO₂ column height is relatively small in this range of fault throw. A low SGR value also suggests the content of the entrained clay in fault zones is not significant in the initial event of fault movement, and the sealing degree of the fault is not sufficient to trap a long CO₂ column by shale smearing.

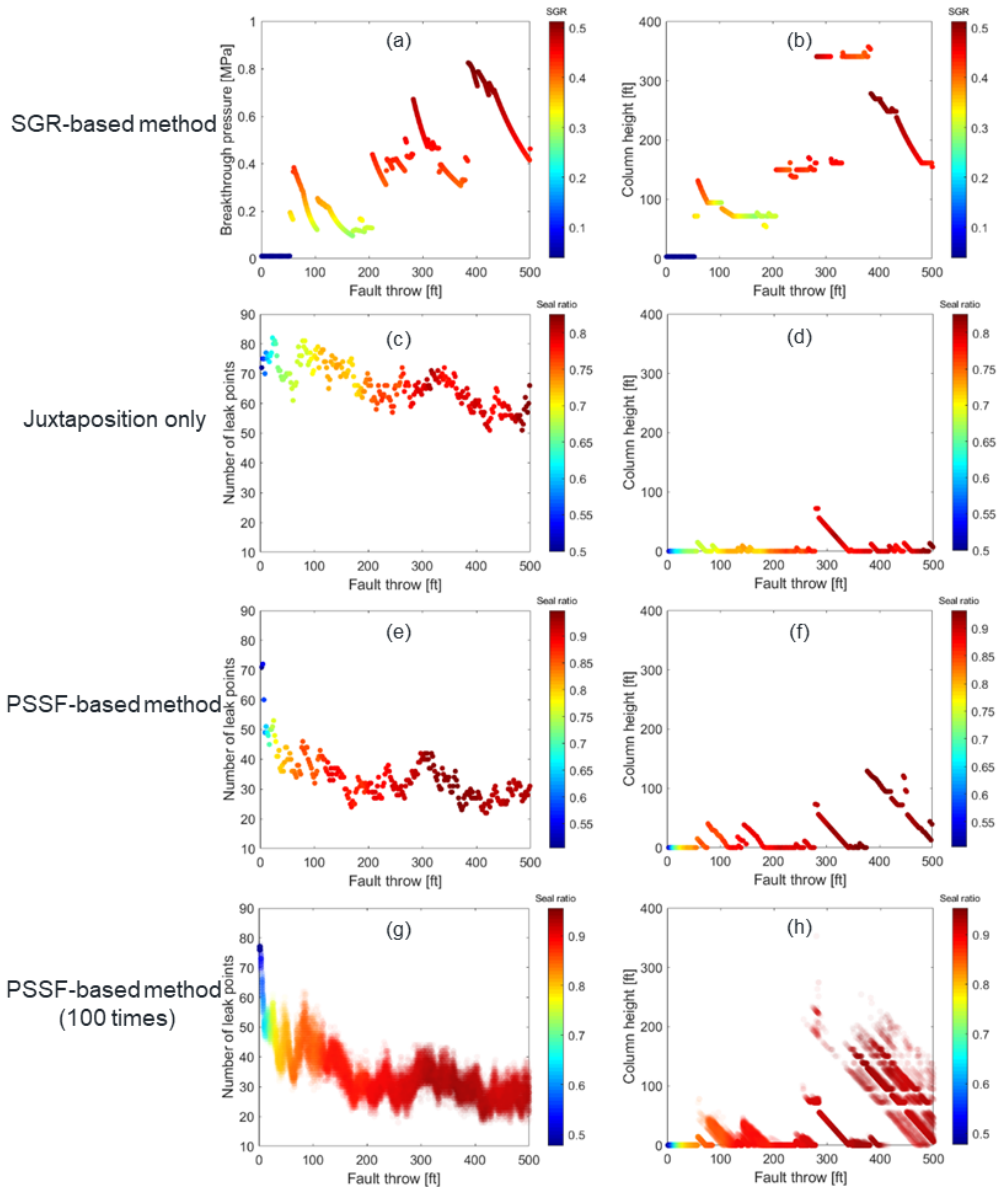


Figure 4.6: Predictions of CO₂ column height with increasing fault throw: (a) breakthrough pressure at the migration point predicted by the SGR-based method; (b) CO₂ column height predicted by the SGR-based method; (c) relationship between number of leak points and fault throw in the juxtaposition case; (d) CO₂ column height predicted by the juxtaposition only; (e) relationship between number of leak points and fault throw in the PSSF-based method; (f) CO₂ column height predicted by the PSSF-based method; (g) relationship between number of leak points and fault throw for 100 simulations; (h) CO₂ column height predicted by the PSSF-based method for 100 simulations.

The SGR-based method implies that a large fault throw results in a highly homogenized fault gouge, and thus, the resulting column height is more than 150 ft. In fact, the SGR equation (Equation 4.1) is a weighted average and tends to a non-zero asymptotic value. The breakthrough pressure is as high as 0.4 MPa when SGR is about 0.4, suggesting a significant amount of clay mixed with sands forming a barrier for CO₂ flow at a fault throw larger than 400 ft. According to the SGR-based method, the fault sealing capacity results in a CO₂ column >150 for this particular sequence and fault throws over ~200 ft. The PSSF-based method challenges this conclusion.

4.3.2 PSSF-based column height prediction

The PSSF-based method assumes trapped CO₂ is the collaborative result of both juxtaposition sealing and smear sealing as discussed in Section 2.3. We run a comparison case in which only the juxtaposition plays the role of sealing without the participation of clay smear (Figures 4.6c and 4.6d). The number of leak points decreases by ~31% when the throw increases up to 500 ft with juxtaposition only. The presence of numerous leak points provides plentiful migration paths for CO₂ flow and overall, the fault can barely trap a long CO₂ column. The relatively large column height (~60 ft maximum) at the fault throw between 270 to 340 ft is due to the juxtaposition of a thick shale layer at the depth of 6,270 to 6,340 ft (Figure 4.3a).

Figures 4.6e and 4.6f summarize the CO₂ column height predicted by the PSSF-based method. The critical shale smear factor is set to SSFc = 3, the most frequent value in Lindsay's statistics on 80 faults in the UK (Lindsay et al., 2009). The discussion section explores the sensitivity of column height with SSFc. The number of leak points decreases from 73 to about 30±10 and the seal ratio increases from 0.5 to 0.95 with the increase of fault throw from 0 to 500 ft. Consequently, the increase of fault throw results in a highly

variable CO₂ column height that varies from 0 ft to a maximum of ~155 ft, depending on fault throw and the realization case.

We created 100 realizations of CO₂ column height and summarize the results in Figures 4.6g and 4.6h. The maximum thickness for shale layers in this example is 72.5 ft, therefore, the maximum critical throw for SSFc = 3 is 72.5 ft × 3 = 217.5 ft. For a small fault throw (less than 217.5 ft), about 98% of the realizations predict a column height less than 50 ft (Figure 4.6h). When fault throw is larger than the maximum critical throw, the distribution of column height becomes scattered as all the smears have breached at this time and their location along the fault is variable. The probability of having a CO₂ column larger than 150 ft is about 11%. The predicted CO₂ column height in the High Island Field also matches with natural gas column height in the literature (Appendix A6).

Figures 4.6f and 4.6h show two outstanding features. First, column height is linearly inversely proportional to fault throw if there are continuous sealing intervals in faults. Hence, increasing fault throw with a relative static leak point results in decreases of column height (Figure 4.7a). A continuous line refers to a continuous sealing interval, either by thick shale layers or long clay smears, as smear location is correlated to its previous location through normal distribution. Second, discontinuous distribution of CO₂ column height is due to the presence of leak points. Buoyant CO₂ will start accumulating beneath the caprock and migrate through the first leak point found. The cut-off in the column height distribution indicates the occurrence of leak points across faults, which may or may not be covered by smears. The location of the first leak point changes as leak points get sealed by smears or smears breach (Figure 4.7b). Small leak points tend to be more easily sealed by clay smears. On the contrary, a large leak point is not easily sealed by clay smears and usually plays an important role in setting an upper bound for the maximum CO₂ column height.

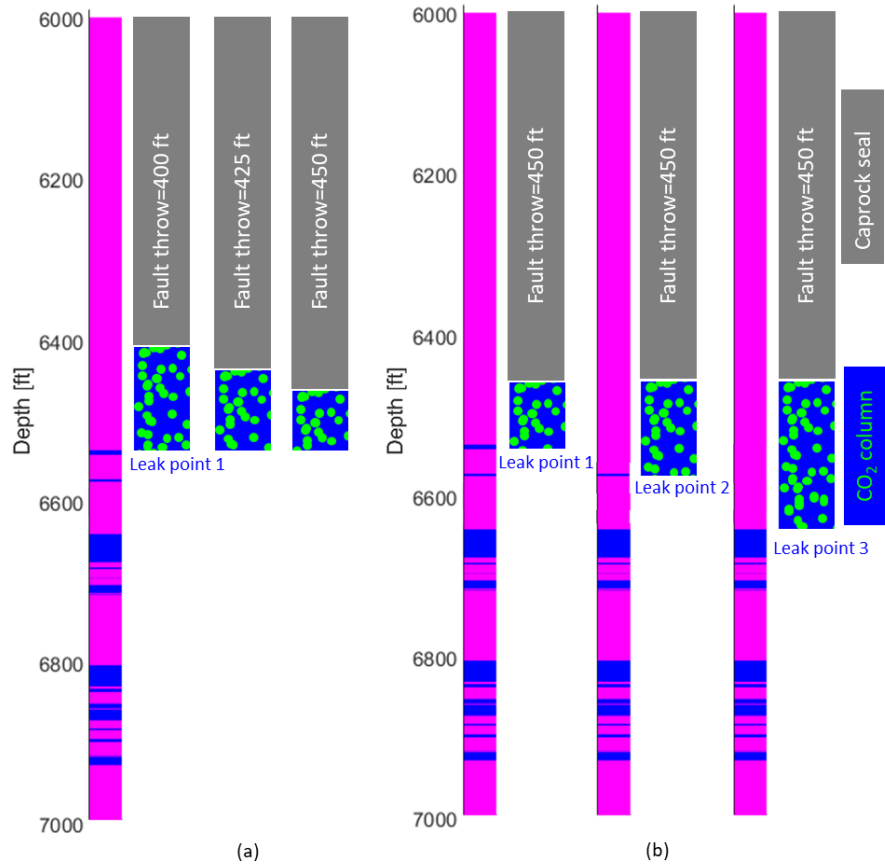


Figure 4.7: Schematic diagram of CO₂ column variability due to location and presence of leak points (sand-breach-sand): (a) inverse linear relationship between column height and fault throw; (b) discontinuous distribution of column height due to the presence of leak points. Small leak points are vulnerable to clay smears, while big leak points set an upper bound for the maximum possible column height.

4.4 DISCUSSION

4.4.1 Uncertainty quantification in the determination of maximum CO₂ column height

The exact position of clay smears along a fault is practically impossible to get to know deterministically and has been a challenge to industry for decades (Lindsay et al., 2009; Yielding et al., 1997). Instead, we present a probabilistic analysis of the resulting

CO_2 column height as a function of fault throw for 100 realizations (Figure 4.8a). The following observations are a result of this analysis for the High Island field with $\text{SSFc} = 3$:

- There is no fault sealing capacity for fault throw smaller than 50 ft.
- More than 50% of the realizations predict negligible fault sealing when fault throw is between 50 ft and 275 ft. The remaining realizations reach a CO_2 column as tall as ~50 ft and extraordinarily up to ~75 ft.
- The linear decrease of CO_2 column height with fault throw for a given leak point becomes dominant when breached smears overlap at a throw larger than the maximum critical throw (217.5 ft).
- Large fault throws (>275 ft) present large variability in the potential trapped CO_2 column height. There is potential for tall columns but many realizations also show negligible fault capacity for the same fault throw. For example, the probability of trapping a CO_2 column larger than 110 ft at 400 ft throw is as high as 70%, while the probability decreases to 20% for 500 ft throw.
- Overall, this analysis suggests it is very unlikely to have a CO_2 column higher than 200 ft in the High Island field at any fault throw with $\text{SSFc} = 3$.
- Only large displacements (>10 ft) can affect fault sealing capacity. Hence, small displacements that could be a result from fault reactivation may affect sealing capacity only during a short time assuming that clay ductility will seal off faults when pore pressure decreases.

The determination of fault slip length is a fundamental component for better understanding the tectonic history in a region (Cowie et al., 2012). The accurate measurement on a single fault is important but not representative of field conditions with numerous faults. Instead, a statistical range of fault throw might be more useful for practical applications in a given sand-shale sequence. Therefore, we separate fault throw

into 10 groups with an interval of 50 ft and compute the relative frequency of column height in these intervals (Figure 4.8b). For example, the faults with a fault throw between 350 ft and 400 ft can barely trap a long CO₂ column since the probability of having a column height larger than 50 ft is less than 0.1.

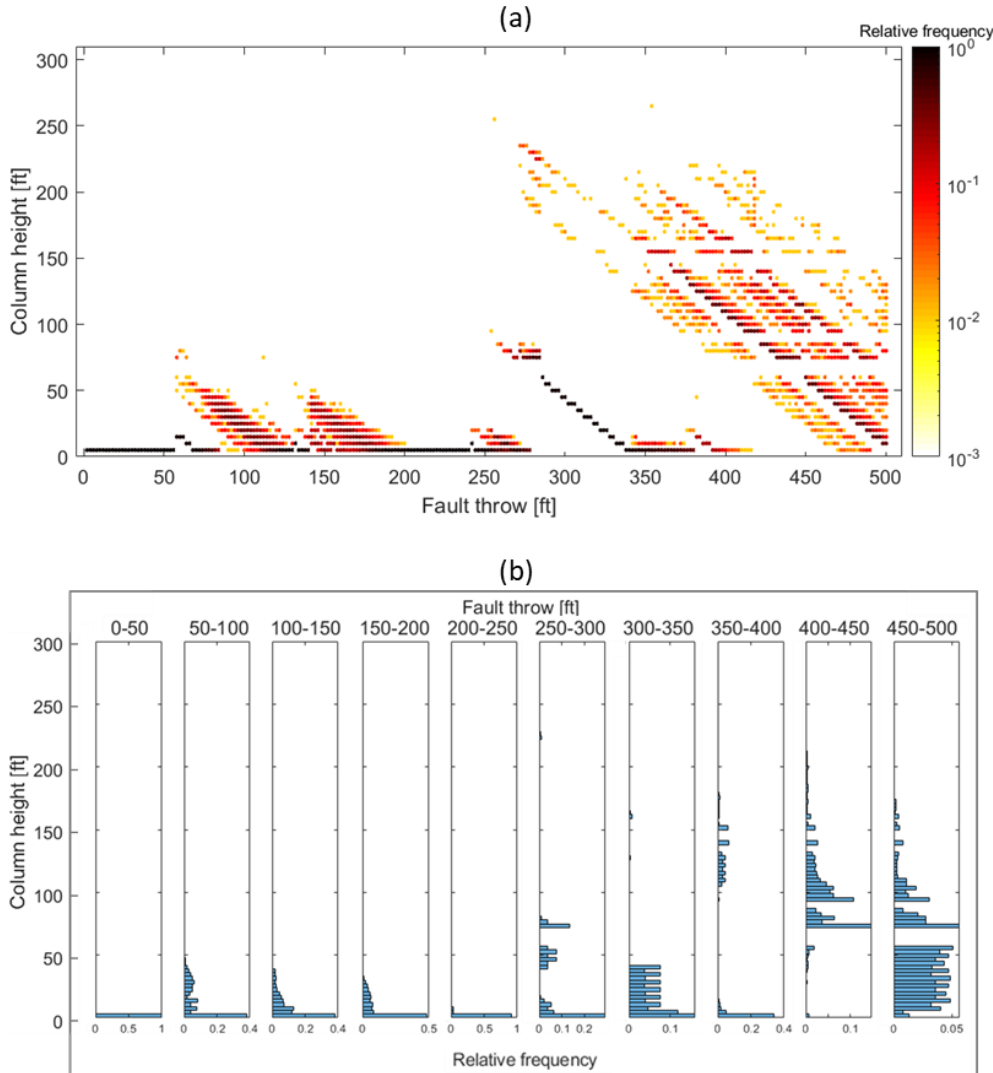


Figure 4.8: Statistical analysis of CO₂ column height with increasing fault throw: (a) relative frequency of CO₂ column height at different fault throws; (b) relative frequency of CO₂ column height at major intervals of fault throw.

The uncertainty of clay smear overlapping and breaching can be further explored analyzing locations of leak points with depth at a given fault throw (450 ft) for 100 realizations. Here the leak probability at each depth is defined as the ratio between the number of times of encountering a leak point (sand-breach-sand) and total number of simulations. The results show that the leak probability varies significantly along the fault (Figure 4.9a). Typically, the location where a sand layer juxtaposes with a sand layer favors a high leak probability. For example, the thick, continuous sand-sand juxtaposition in the depth of 6,600 ft to 6,700 ft has a high leak probability.

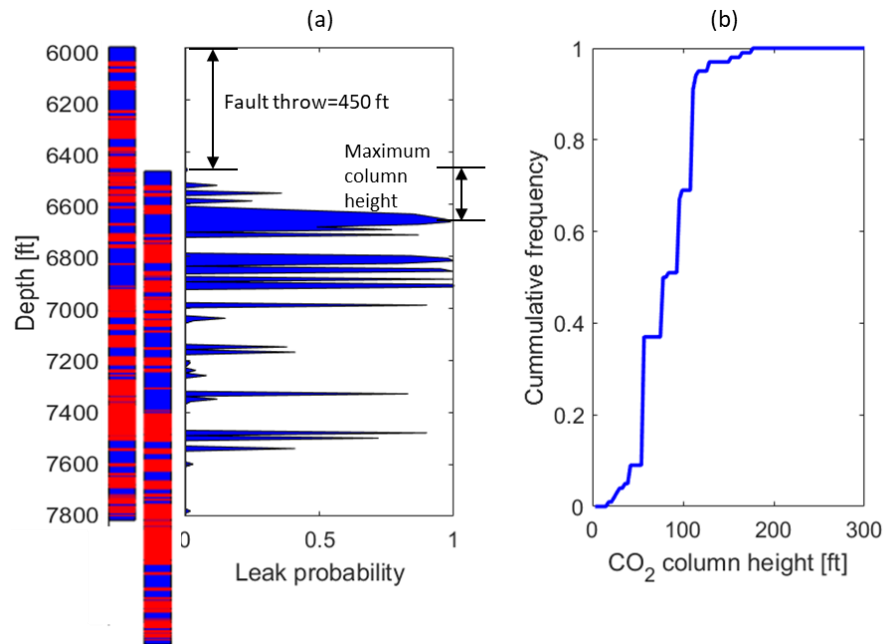


Figure 4.9: Distribution maximum CO₂ column heights at a fault throw of 450 ft for 100 simulations: (a) distribution of leak probability along the fault; (b) Cumulative frequency of maximum CO₂ column height. The maximum possible column height is closely related to the distribution of leak probability along the depth.

The leak probability has a strong influence in the cumulative frequency of maximum CO₂ column height (Figure 4.9b). The stepwise increase of cumulative

frequency corresponds to separate peaks in the distribution of leak probabilities from the depth of 6,450 ft to 6,650 ft. The probability of encountering a leak point at the depth of 6,650 ft is as high as 1, which results in a maximum CO₂ column height of 200 ft at this fault throw. It is quite unlikely to develop taller CO₂ columns because of the high probability of encountering migration paths along the way.

4.4.2 Effects of clay ductility on CO₂ column height and comparison with SGR-based method and juxtaposition only

One of the key parameters in determining clay smear potential is SSFc. The maximum fault throw with continuous clay smear determines SSFc. Thus, clay ductility, the property of deforming without the creation of discontinuities, directly impacts the value of SSFc. The increase of clay ductility can be captured in the PSSF-based model through an increase of the parameter SSFc. Sediment ductility depends on volume fractions of clay, clay type, and water salinity. The higher the specific surface of the clay, the higher the clay ductility (Santamarina et al., 2001). Ductile shales are often considered as those having a low amount of quartz and carbonate minerals but a high clay content (Gholami et al., 2016). Sediment ductility is usually quantified by the plastic index and smectite clays exhibit the highest plasticity (Germaine & Germaine, 2009).

The variability of shale plasticity prompts a sensitivity analysis to evaluate the effect of SSFc on clay smear distribution and CO₂ column height (Figure 4.10). The column on the left of each sub-figure is the schematic diagram of smear distribution in one example realization and the plot summarizes results of the maximum CO₂ column height considering: (1) juxtaposition seal only, (2) homogeneous clay distribution through the SGR-based method, and (3) clay smears from 100 realizations through the PSSF-based method.

- *Brittle case* (SSFc=2): Almost all the resulting column heights are smaller than 150 ft with the PSSF-based method. The length of each clay smear is relatively short ($75\% < 10$ ft), which results in many leak points along the fault (Figure 4.10a). The juxtaposition seal and the PSSF-based method predict similar results when fault throw is smaller than 340 ft, which suggests that brittle clay with short smears cannot seal faults and the juxtaposition seal will be the principal mechanism for trapping CO₂. The SGR-based method ignores the effects of clay brittleness and results in column height 1-to-3 times higher than the other two methods. The results of the PSSF-based method are bounded by the results of two other approaches.
- *Intermediate ‘base’ case* (SSFc=4): About 14% of the realizations with a fault throw larger than 400 ft result in a column height larger than 150 ft with the PSSF-based method (Figure 4.10b). A low expected column height at 270 ft appears in all three approaches due to the presence of a thick sand. The results of the SGR-based method still serve as an upper bound of most column height results predicted by the stochastic PSSF-method.
- *Ductile case* (SSFc=6): This ductility results in significantly large column heights with a maximum height up to 475 ft (Figure 4.10c). Clay smears of each shale source extend and overlap on each other as SSFc increases, which produces long and continuous smears. Numerous long smears seal regions with extended leak points at the depth of 150 ft below the caprock. As a result, sealing capacity and maximum CO₂ column height increases. About 73% of the realizations predict a column height greater than 150 ft when the throw is larger than 400 ft. The results of the SGR-based method in this case serve mostly as a lower bound of the PSSF-based results.

The maximum CO₂ column prediction from the juxtaposition only serves as an absolute lower bound in the prediction of CO₂ column height. SGR results are very sensitive to the location of the selected local area when fault throw is small and tend to represent homogenized fault properties as fault throw increases (based on SGR definition). However, the PSSF-based method incorporates more realistic geological processes, yields the possible range of CO₂ column height at each fault throw, and highlights the discrepancies that may be derived from using the SGR-based method.

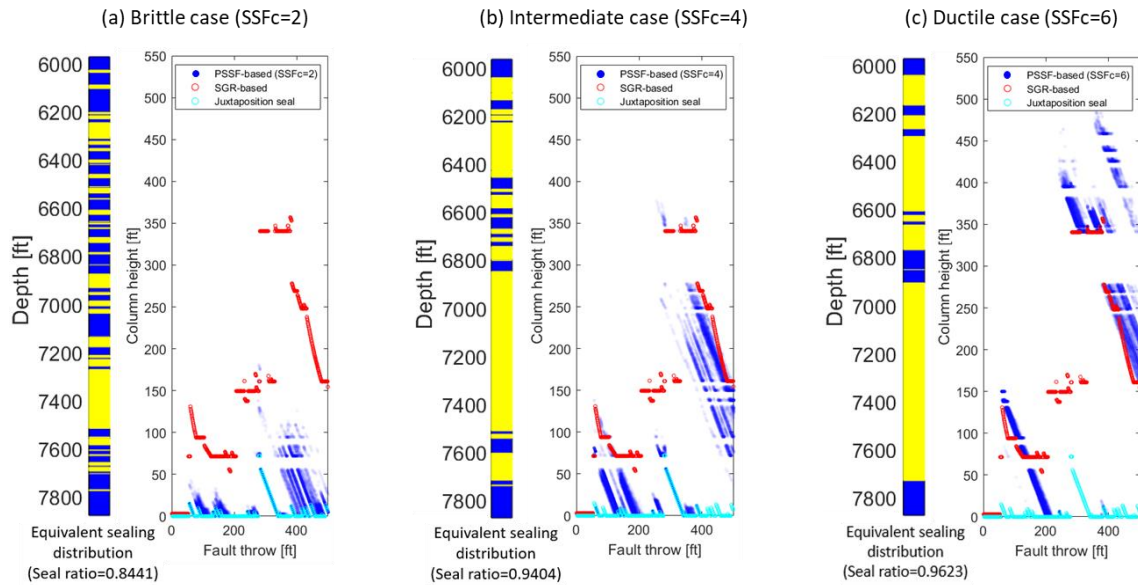


Figure 4.10: Distribution of clay smear and CO₂ column height with different values of SSFc: (a) SSFc=2; (b) SSFc=4; (c) SSFc=6. The juxtaposition seal serves as the lower bound of CO₂ height prediction. Clay smears (yellow intervals) add significant uncertainty to the prediction of CO₂ column height. Ductile clay with a high SSFc tends to have a long smear in faults and thus support a large CO₂ column.

4.4.3 Application of the PSSF-based method to hydrocarbon columns observed in the field

Yielding (2002) compiled buoyancy pressure data from hydrocarbon columns at multiple locations around the world and plotted them as a function of the calculated SGR (marked by black symbols in Figure 4.11), where the SGR was measured along the fault and the buoyancy pressure was derived from the well pressure data at the same points on the juxtaposition area. The field data show a general trend of increasing buoyancy pressure (e.g., 71 ft of CO₂ column for a buoyancy pressure of 100 psi) with increasing SGR. However, the trend is not unique and significantly small hydrocarbon columns were observed in faults with high SGR. The field data highlight the existence of an upper bound for maximum column height with increasing fault throw and the variability (sometimes over two orders of magnitude) of the resulting maximum buoyant column height.

The PSSF-based method results for a typical case in the Gulf of Mexico are superimposed to Yielding's data in Figure 4.11. The calculated column height also presents an upper bound (marked with a straight line) and high variability. This upper bound moves upward with the increase of SSFc, and it is not a fixed "failure envelope" as suggested by Yielding (2002). Smaller SSFc yields higher variability in expected maximum column heights. The simulated SGR values vary from 0.25 to 0.45 for this specific location in the High Island field. For a given SGR value, the range of buoyancy pressure can be up to one to two orders of magnitude. The SGR value less than 0.2 or larger than 0.55 is scarce, although the distribution of SGR data depends on the specific stratigraphic profile. The simulated maximum column heights are in agreement with hydrocarbon field observations that support a weak positive correlation between SGR and buoyancy pressure, no major increases in buoyancy pressure for SGR values greater than ~0.4, and high variability of the results (Bretan et al., 2003).

The major conclusion of this comparison is that the maximum buoyancy pressure a fault can sustain cannot be determined through a single SGR value. The ductility and continuity of clay smears (related to SSFc), which the SGR-based method fails to capture, play an important role in controlling fault sealing potential. The PSSF-based method takes into account the effect of smears on fault sealing and highlights geologic uncertainties in the prediction of the maximum CO₂ column a fault can trap.

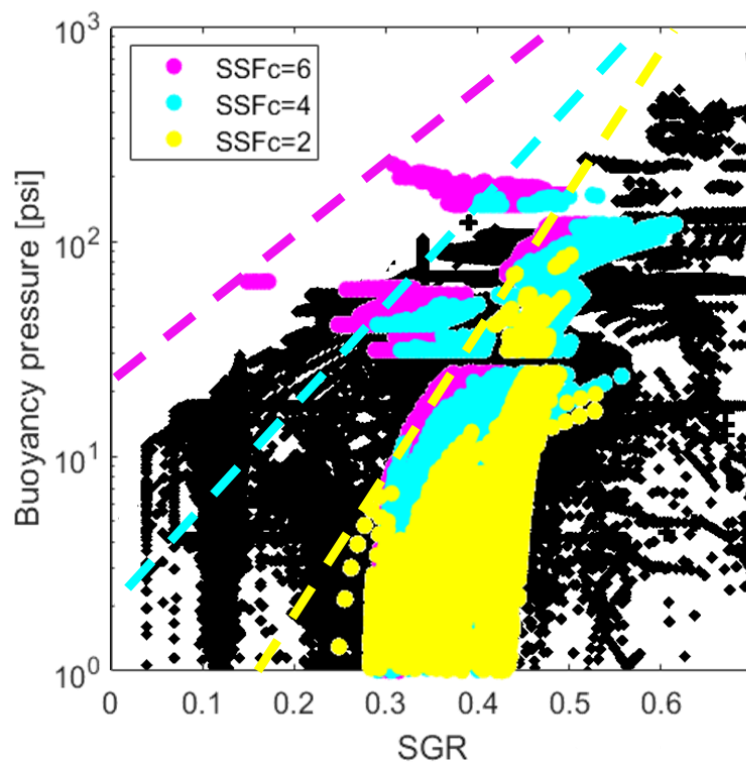


Figure 4.11: Upper bound for sealing capacity: our PSSF-based results (purple, cyan, and yellow markers) is superposed to the field data (black markers) (Yielding, 2002). There are one hundred realizations for each SSFc. The PSSF-based method reproduces variability observed in the field, highlights the uncertainties in the calculation of CO₂ column height, and expose the limitations of the SGR-based method.

4.5 CONCLUSIONS

We proposed a stochastic method based on probabilistic distribution of shale smears to predict maximum CO₂ column height at faults in shale-sand sedimentary sequences exemplified by a case in the High Island field in Texas. The major conclusions are:

- Buoyant CO₂ tends to migrate through the shallowest leak point in faults below a caprock, which is determined by both juxtaposition seal and clay smears. The presence of numerous leak points due to smear breaching may provide migration paths for buoyant CO₂ and decrease likelihood to trap a tall CO₂ column. Hence, the determination of fault sealing capacity on CO₂ column height requires reliable prediction of the location and properties of these leak points. We assumed the sand-breach-sand contact scenario is the primary migration path for CO₂ across faults, but more accurate models may incorporate two-phase fluid-flow properties for all fault contact types.
- We combined field data and laboratory data to investigate fault sealing capacity at the High Island field in Galveston county, Texas. The results show significant variability of sealing capacity with fault throw assuming a medium ductility (SSFc = 3). More than 50% of the realizations predict negligible fault sealing and the remaining realizations reach a CO₂ column as tall as ~50 ft when fault throw is less than 275 ft. A linear decrease of CO₂ column height with fault throw becomes dominant after fully-breached smears are placed over each other at a throw larger than the maximum critical throw (217.5 ft). Large fault throws (>275 ft) present many smear discontinuities and therefore large variability in the potential trapped CO₂ column height. The probability of trapping a CO₂ column larger than 110 ft at 400 ft throw is as high as 70%, while the probability decreases to 20% for 500 ft

- throw. A large proportion of the realizations result in negligible fault sealing capacity. The results imply that exceeding the critical fault throw may result in faults with drastically different sealing capacity even within the same structural complex. A corollary of this analysis is that small fault displacements induced by fault reactivation due to transient pore pressure increases will not affect the long-term sealing capacity of faults sealed by sand-shale juxtaposition and clay smears.
- Clay smear continuity significantly affects fault sealing capacity. Ductility of clay smear, which is characterized by critical shale smear factor (SSFc), controls clay extension and truncation. Brittle clay with short smears cannot form a strong sealing in faults. However, ductile clays have the potential to produce long and continuous smears and result in significantly large column heights. Future exploration work and seal evaluation should put emphasis on constraining the value of SSFc, for example, characterization of fault and parent shale clay plasticity.
 - The PSSF-based method permits explaining and incorporating variability of column heights observed in the field that are less straight-forward to predict with the SGR-based method. The SGR-based method assumes a more homogeneous distribution of shale gouge within faults than the PSSF-based approach and results in a value of CO₂ column height that may be significantly higher or lower than the value predicted by the PSSF-based method, which incorporates the effects of the ductility, continuity, and breaching of clay smears. The presence of small gaps in faults leads to large variability of the potential sealing capacity.
 - This work explored a one-dimensional application of the PSSF-based method with accumulation on the side of the footwall. Future work aims at implementing an extension of this method to three-dimensional fault structures accounting for

additional complexities such as oblique slip, varying fault throw, varying stratigraphy, and presence of growth sections.

Chapter 5: Pressure Monitoring above the Injection Zone for CO₂ Geological Storage

5.1 INTRODUCTION

The successful development of carbon dioxide (CO₂) storage necessitates robust monitoring methods to detect potential CO₂ leakage into overlying formations and provide assurance for permanent CO₂ trapping (Kim & Hosseini, 2015; T. Meckel et al., 2008). Most monitoring techniques are based on measurements on the surface and in the injection zone. On-surface monitoring (such as 4D seismic and InSAR mapping) can capture large geophysical features but is limited by high costs, laborious interpretation, and a large buffer zone of signals imposed by the overburden (Arts et al., 2004; Jonny Rutqvist et al., 2010). Monitoring in the injection zone (IZ) involves fluid sampling, rock analysis, and placement of sensors in the target formation, enables direct access to the zone of interest, and offers early leak detection, but remains limited to a few observation wells and small sampling volumes (Ajo-Franklin et al., 2013; Hovorka et al., 2006a; Zeidouni & Pooladi-Darvish, 2012b, 2012a).

Pressure monitoring above the injection zone (AIZ) is a new approach to monitor CO₂ injection and detect undesirable migration of fluids from the injection zone to overlying formations (Liebscher et al., 2013; Park et al., 2012). AIZ pressure monitoring is less costly than on-surface seismic monitoring, covers a wider area than the IZ monitoring, and has the potential to detect leaks into overlying formations (Hosseini et al., 2018). Pore pressure increases in the AIZ were thought to be zero if no hydraulic communication occurred. Thus, any deviation from the pressure baseline (expected to be constant) could be considered as a result of leaks. However, recent AIZ pressure monitoring in the Cranfield CO₂ injection project indicates measurable changes of pore pressure (~50 kPa) after two years of CO₂ injection with IZ pressure change reaching a

maximum of ~8.8 MPa in the absence of leaks (Kim & Hosseini, 2014; Tao et al., 2012). Despite recent advances and numerical simulations, AIZ poroelastic monitoring remains largely underutilized because of a lack of (1) validation schemes, (2) thorough measurement of poromechanical properties of AIZ, (3) thorough deployment of high-resolution sensors to capture subtle pressure changes (e.g., 1 kPa), and (4) coupled poroelastic simulation beyond the injection zone for all CO₂ storage projects (Hosseini et al., 2018; Hosseini & Alfi, 2016; Kim & Hosseini, 2014; Mishra et al., 2014).

CO₂ injection and reservoir pressurization cause displacements and deformations within and outside the reservoir (Segall & Fitzgerald, 1998). Fluid injection and reservoir pressurization may result in surface uplift due to expansion of the reservoir caused by decreased effective stress. For example, InSAR data shows a surface uplift on the order of 5 mm per year in the In Salah Gas Project in Algeria (with a CO₂ injection rate of 0.5–1 Mt/year) (Rutqvist et al., 2009; Jonny Rutqvist et al., 2010). The poroelastic response of fluid-saturated rocks may appear as a deformation, but also as a change of pore pressure (Detournay & Cheng, 1988; Ennis-King et al., 2017; Roussel & Agrawal, 2017). During a drained process, at constant pressure, fluid mass transfer induces volumetric strains. In contrast, pore pressure will increase in an undrained process when a (contraction) volumetric deformation is applied to a fluid-filled porous material (Cheng, 2016; Coussy, 2004). Fluid injection and reservoir pressurization load overlying formations. Even in the absence of hydraulic communication between the IZ and the AIZ, i.e., this load from the fluid injection can modify the pore pressure in the AIZ due to undrained loading.

Two mechanisms can contribute to pore pressure changes in porous media: (1) advective fluid transport; and (2) pore volume deformation. These coupled pore pressure diffusion and mechanical deformation processes are captured by the pressure P diffusivity

equation for fluid flow coupled with poroelasticity (Cheng, 2016; Coussy, 2004; Detournay & Cheng, 1993):

$$\frac{\partial P}{\partial t} = \frac{kM^*}{\mu} \nabla^2 P - \alpha M^* \frac{\partial \varepsilon_v}{\partial t} \quad (5.1)$$

where k is the porous medium permeability, μ is the fluid viscosity, α is the Biot coefficient, ε_v is the bulk volumetric strain, and the Biot modulus M^* is

$$M^* = \left(\frac{\phi_0}{K_f} + \frac{\alpha - \phi_0}{K_m} \right)^{-1} \quad (5.2)$$

where ϕ_0 is the initial rock porosity, K_f is the bulk modulus of the pore fluid, and K_m is the bulk modulus of the rock matrix.

For a linear elastic isotropic porous solid, the expected pore pressure change ΔP under undrained loading (no change in fluid mass) is directly proportional to the volumetric strain (Coussy, 2004):

$$\Delta P = -\alpha M^* \Delta \varepsilon_v \quad (5.3)$$

Thus, the estimation of pore pressure change as a response to undrained loading depends on rock poroelastic properties, fluid compressibility (K_f)⁻¹, and volumetric strain. Decreases in pore volume lead to increases of pore pressure, while increases in pore volume lead to decreases of pore pressure (Figure 5.1).

Whether a process is undrained or drained depends on the rate of (strain) loading and the rate of pore pressure diffusion. Perfect fluid containment is rare in natural environments, so most processes can be generalized as partially undrained depending on the time interval of analysis. For example, the characteristic time of pressure diffusion T_{ch} captures the time when ~2/3 of the pore pressure is relieved from an initial undrained loading state (Cheng, 2016):

$$T_{ch} = \frac{L^2}{D_h} \quad (5.4)$$

where L is the characteristic drainage length and $D_h = \frac{kM^*}{\mu}$ is the hydraulic diffusivity.

Higher permeability and shorter characteristic distance of drainage decrease the characteristic pore pressure diffusion time and the magnitude of pore pressure increase for partially undrained loading of real sediments (Figure 5.1). Thus, the partially undrained condition entails a smaller amount of pore pressure variations than the fully undrained condition due to pressure dissipation. In fact, if the rate of (strain) loading is lower than the rate of pore pressure diffusion, a porous medium may never experience a pore pressure change due to pore volume reduction. Additional constitutive equations for the multiphase fluid flow, the poroelastic solid, and coupled hydro-mechanical simulation are available in Appendix A7 (Cheng, 2016; Coussy, 2004; Prevost, 2013; Tran et al., 2009).

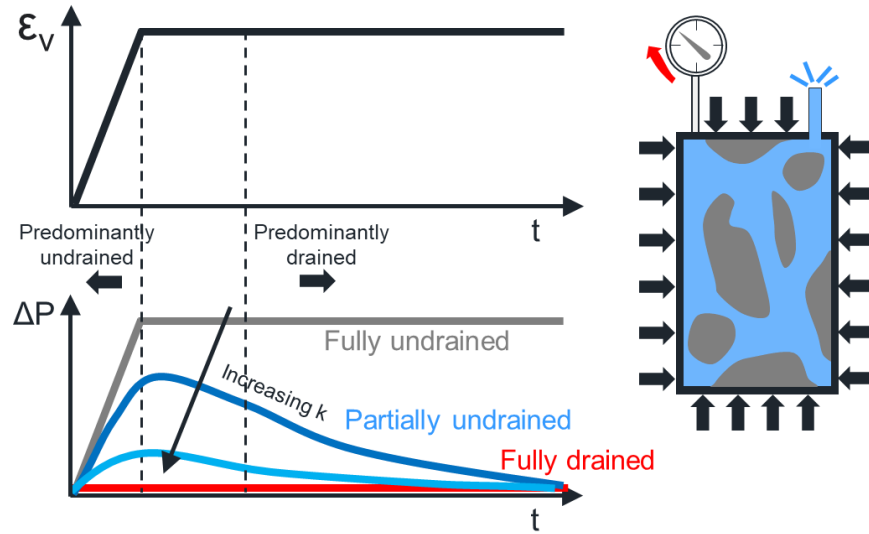


Figure 5.1: Comparison among fully drained, partially undrained, and undrained conditions: the pore pressure changes under the fully undrained condition are proportional to the imposed volumetric strain but also depend on the hydraulic diffusivity of the porous medium.

The objective of this study is to verify the feasibility of utilizing pore-pressure monitoring in the AIZ as a new subsurface signal that can potentially track the CO₂ plume, detect possible leaks, and help ensure safe storage of CO₂. This chapter starts with a description of the compositional fluid flow model coupled with the geomechanical model. We examine the poroelastic response in the AIZ by analyzing the magnitude, evolution, and distribution of the pressure increase in the AIZ. The analysis also discusses the possible configuration of pressure sensors regarding their position with respect to the injector. The discussion section considers the presence of different subsurface scenarios, including the presence of a poorly cemented injector wellbore, a leaky abandoned wellbore, a leaky/sealing fault, and two injectors.

5.2 METHODOLOGY

5.2.1 Reservoir geometry, boundary conditions, and input parameters

We use a fluid-flow compositional model coupled with poroelasticity for the entire storage complex, including overburden layers which are usually ignored in reservoir simulation. All the materials are assumed to be mechanically and hydraulically isotropic. The model is handled through the reservoir simulator CMG-GEM; details about the model formulation and coupling scheme are available in Appendix A7 (Computer Modeling Group Ltd., 2013; Tran et al., 2009). The storage complex extends 12 km by 12 km in the lateral direction (49 blocks by 49 blocks) and 6 km in the vertical direction (48 blocks) (Figure 5.2). The grid size is gradually reduced from the reservoir boundary to the center of the injection point. The grid size ($dx \times dy \times dz$) near the injector is 6 m \times 6 m \times 20 m with mesh refinement near the injection point. The detailed sensitivity tests on grid size are provided in Appendix A8. The lateral extension is sufficiently large to avoid any boundary effects. The injection zone (IZ) is 100 m thick located at 3,040 m of depth. The injection

zone is overlain by a 100 m-thick caprock. The low-permeability caprock overlying the injection zone assures CO₂ containment. The five above-injection-zone (AIZ) layers for pressure monitoring are separated by shales with a spacing of 120 m. Each AIZ has a thickness of 60 m. The IZ and AIZs are pervious layers with high permeability (300 mD) delimited by confining layers with low permeability (100 nD).

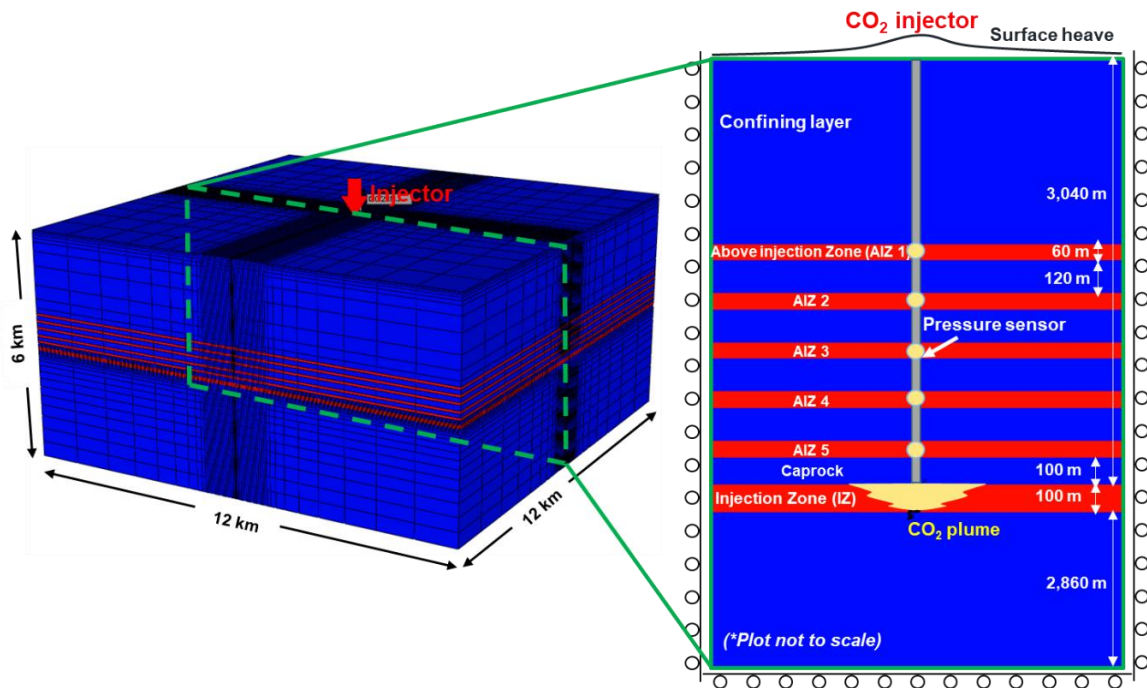


Figure 5.2: Reservoir geometry and boundary conditions. CO₂ is injected into the injection zone (IZ) at the depth of 3,040 m. The injection zone is overlain by a caprock and five above-injection-zone (AIZ) layers for pressure monitoring.

The boundaries of the IZ (the edge of this storage complex) are set to constant pressure and the boundaries of the AIZs are set to no flow condition. The boundary conditions of AIZ (either closed or open) do not affect AIZ pressure changes in the absence of leaks. The remaining lateral shale boundaries have a no-flow boundary condition. The top surface is free to move to capture surface heave due to strains induced in the injection

zone and overburden. Only vertical displacement is allowed for the lateral surfaces in the storage complex. We simulate CO₂ injection at the reservoir center with a constant injection rate of 1,008 tons of CO₂ per day (about 0.37 Mt/year). The injector is modeled as a source term in the IZ with an equivalent radius of 0.1 m. The injection operation lasts for two years followed by one year of shut-in. Other input parameters are listed in Table 5.1. Capillary pressure and relative permeability data are available in Appendix A9. The yellow dots “along the injector” in Figure 5.2 represent the hypothetical location of pressure sensors vertically above the injector source term, although the physical presence of the injector is not modeled.

Table 5.1: Input parameters.

Property	Symbol	IZ/AIZ	Caprock
Initial porosity [-]	ϕ	0.22	0.1
Permeability [mD]	k	300	0.0001
Young's modulus [GPa]	E	5	20
Poisson's ratio [-]	ν	0.2	0.3
Biot coefficient [-]	α	0.92	0.54
Bulk modulus of brine [GPa]	K_f	2.2	
Bulk modulus of rock matrix [GPa]	K_m	36	

5.3 RESULTS

5.3.1 Pressure increase in the above-injection-zone

Numerical simulations show that pressure buildup from CO₂ injection in the IZ causes pore pressure changes in the storage complex outside the IZ in the absence of any leaks (Figure 5.3). The changes are a result of partially undrained loading and, therefore, depend on space and time. For example, the affected region with $\Delta P > 1$ kPa extends to as

far as 2 km away from the injector at $t = 365$ days. The snapshots of pore pressure change at various times demonstrate that the five AIZ layers respond to CO₂ injection in the IZ.

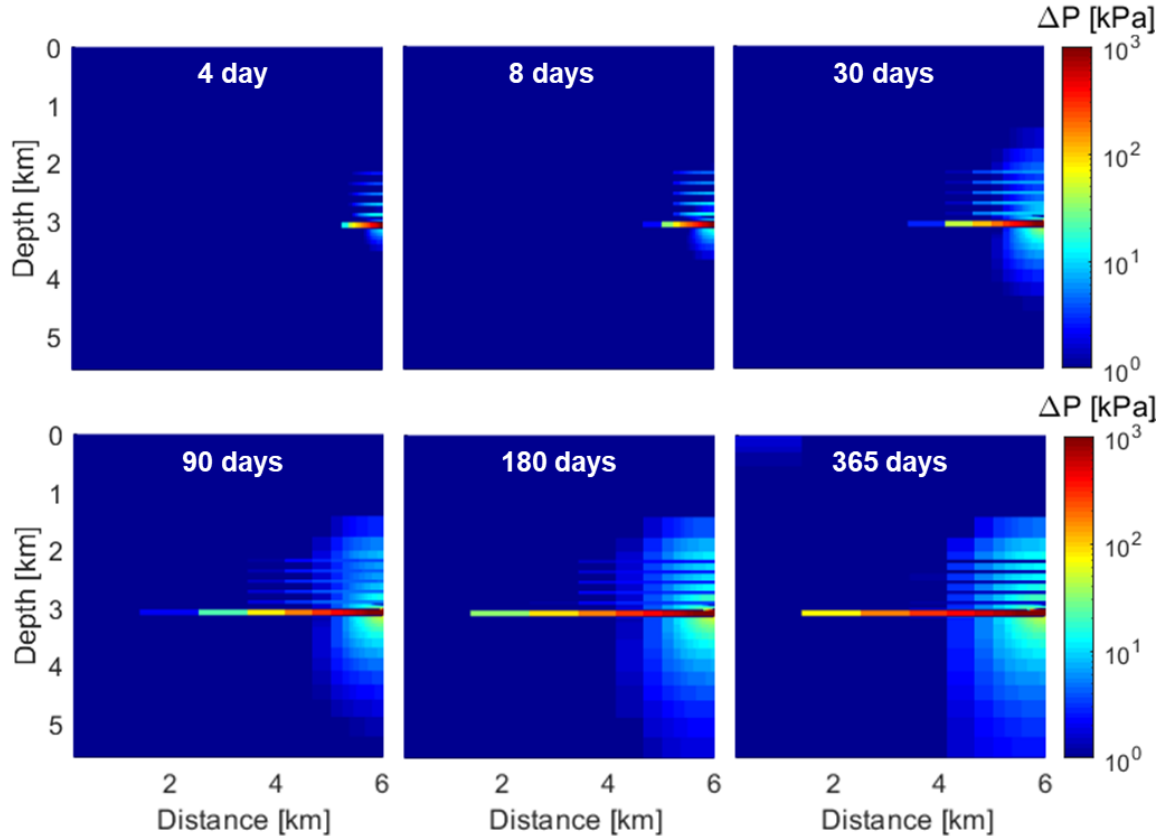


Figure 5.3: Pore pressure changes in the CO₂ storage complex (half-domain shown because of symmetry: injector located on the right boundary). CO₂ injection increases pressure $\Delta P > 1,000$ kPa in the injection zone. Partially undrained loading induced by CO₂ injection causes changes of pore pressure $\Delta P < 20$ kPa around the reservoir layer. Pore pressure in AIZ sands along the injector increases in the first 10 days to a peak value and then decreases with time. Pore pressure in shale exhibits more gradual and long-lasting changes than in sands.

The pore pressure in overlying shales also changes. The difference between pore-pressure changes in sand (AIZ) and shale (caprock and other confining layers) is the result of their distinct mechanical and hydraulic properties including bulk modulus and

permeability. The sand with a lower bulk modulus experiences a larger volumetric strain, and thus a higher increase of pressure than the shale (Equation 5.3). The sand drains more quickly (less than 10 days in this simulation) than the shale because of its larger hydraulic diffusivity (Equation 5.4 and Figure 5.3). As a result, the pressure increase due to partially undrained loading in sand presents a short-term response (\sim 10 days), while the pressure increase in shale can persist for a relatively long time ($>$ 100 days).

The temporal evolution of the injection rate, IZ pressure change ΔP , and AIZ pressure change ΔP during two years of injection and one year of shut-in are closely interrelated (Figure 5.4). The IZ pressure increases as much as 1,600 kPa and is followed by a gradual reduction until equilibrium to quasi-steady-state conditions. Instead, the pore pressure in the AIZ (along the injector) exhibits a transient response. The AIZ pressure increases in the first 10 days and then decreases due to pressure dissipation despite continued injection. The pressure in five AIZ layers is less than 5 kPa after 100 days of injection. For example, AIZ 5 (100 m above the IZ) exhibits an instantaneous response to CO₂ injection and fast pressure buildup during the initial stage of injection. A gentle decrease of pressure with time follows after reaching a peak (15 kPa) at $t = 4$ days. The pressure in other distant AIZ layers exhibits a similar trend but with a smaller amount of pressure variations and a delay in reaching the peak which increases with the distance to the injector. Hence, AIZ pressure changes are time/location-dependent and monitoring should focus on the initial stage of injection activities.

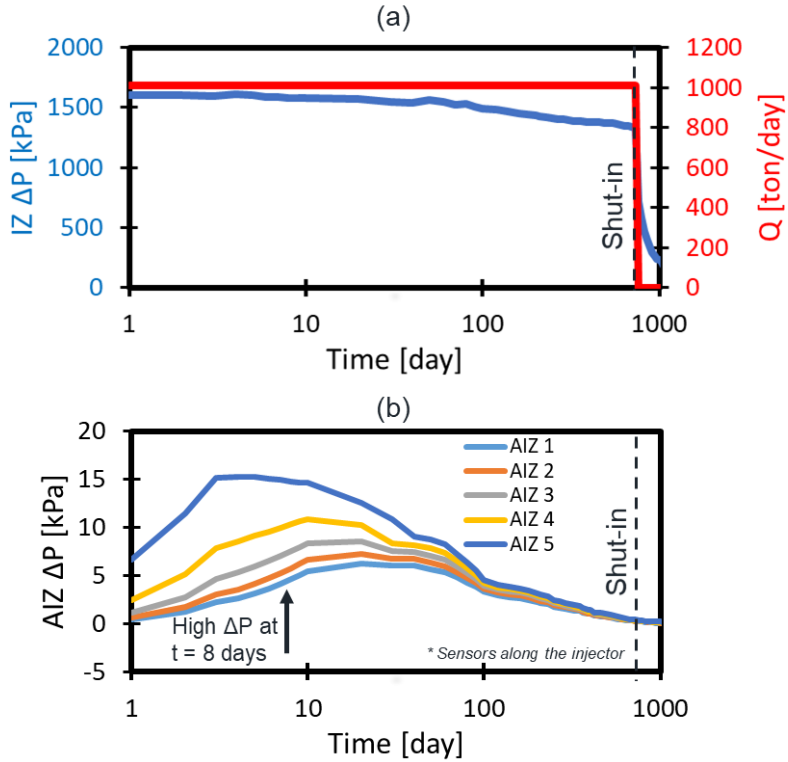


Figure 5.4: CO₂ injection rate and evolution of IZ and AIZ pressure changes: (a) injection rate and bottom-hole pressure increase in the injection zone (IZ); (b) pressure increase above the injection zone (AIZ) due to partially undrained loading.

Figure 5.5 shows the AIZ ΔP pressure front and vertical displacement around the injector at $t = 8$ days (when the maximum AIZ ΔP occurs). The AIZ ΔP is larger than 15 kPa within ~ 160 m of the injection point (the distance here refers to the radial distance to the injection point). A strong ΔP signal favors an easy and reliable interpretation of poroelastic monitoring. The AIZ ΔP decreases more quickly with increasing distance from the injector. The AIZ ΔP is less than 4 kPa when the distance is larger than 880 m. Then, high-resolution pressure sensors in the AIZ would be required to detect small variations of pore pressure for real CO₂ geological storage sites. The typical amplitude of background noise in standard subsurface pressure sensors is around 4 kPa (Hosseini et al., 2018). Noise is the result of several natural and artificial phenomena such as changes in atmospheric

pressure, ocean tides, surface precipitation, and pressure variations associated with measurement instruments and equipment operation. Therefore, pressure sensors in this particular case could detect undrained loading ($\Delta P > 4$ kPa) if installed closer than ~ 880 m from the injection point.

The vertical displacement induced by CO₂ injection is the highest closer to the injector. The uplift is higher than 5 mm if the distance to the injector is smaller than 160 m. The formation immediately above the injection zone has the maximum vertical displacement (~ 6 mm), which is a result of the reduced effective vertical stress in the IZ. This figure highlights the potential of poroelastic monitoring when surface heave (~ 0.3 mm straight above injector in this case) is challenging or impossible to measure on the surface.

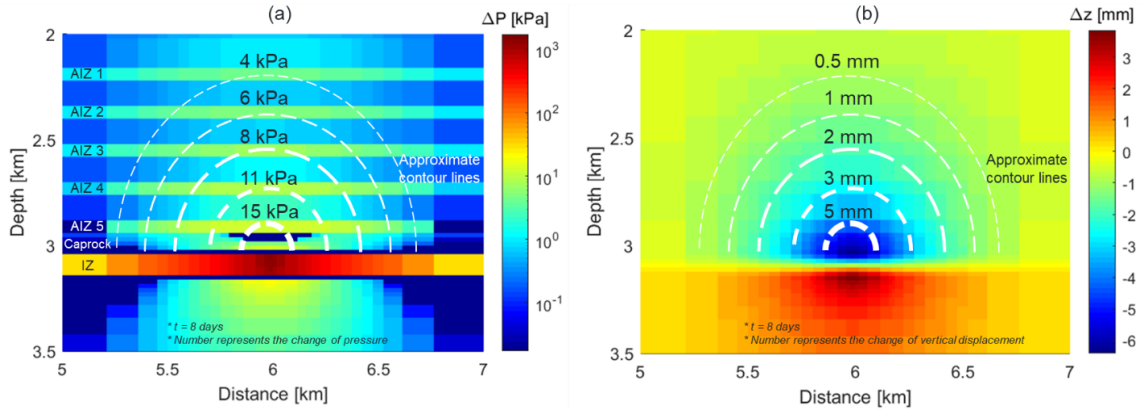


Figure 5.5: Poroelastic response at $t = 8$ days due to CO₂ injection: (a) pore pressure changes in the storage complex and pressure fronts above the injection zone (AIZ); (b) vertical displacement. Surface heave is negligible while pore pressure change in the AIZ is in the order of 10^1 kPa.

5.3.2 Relationship between AIZ ΔP and IZ ΔP

The relationship between AIZ ΔP and IZ ΔP enables the estimation of the IZ pressure from pressure increases in the AIZ. Let us examine the ratio between AIZ ΔP and IZ ΔP along the injector and plot the results as a function of time for the five AIZ (Figure

5.6a). The ratio between AIZ ΔP and IZ ΔP reaches a peak (0.40%, 0.46%, 0.54%, 0.69%, and 0.95%) between 4 to 20 days and then decreases with time. Thus, the AIZ pressure increase can be as large as $\sim 1\%$ of the IZ pressure increase for this selected reservoir model.

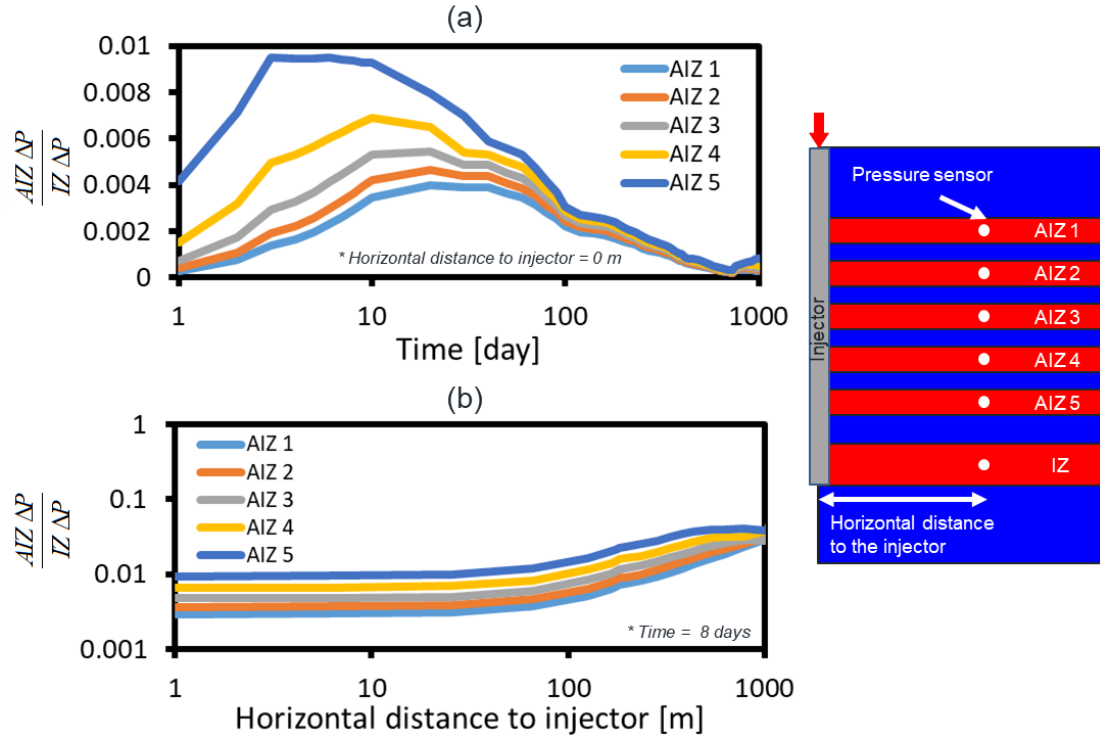


Figure 5.6: Relationship between AIZ ΔP and IZ ΔP : (1) ratio between AIZ ΔP and IZ ΔP as a function of time (sampled points along the injector); (2) ratio between AIZ ΔP and IZ ΔP as a function of horizontal distance to the injector (time = 8 days). The maximum ratio is about 1% in the areas of interest.

Figure 5.6b shows the ratio between AIZ ΔP and IZ ΔP for pairs located at the same horizontal distance from the injector at $t = 8$ days. The ratio between AIZ ΔP and IZ ΔP is nearly constant within 100 m around the injector, which indicates that the percentage of the AIZ ΔP with respect to the IZ ΔP for five AIZs does not rely much on the horizontal

distance to the injector. For a distance larger than 1000 m, the ratio between AIZ ΔP and IZ ΔP is meaningless since the pressure variations in IZ and AIZ tend to be negligible.

5.3.3 Prediction of CO₂ plume migration from AIZ pressure increase

The prediction of CO₂ plume migration from AIZ ΔP requires finding a relationship between the length of the CO₂ plume and the AIZ ΔP induced by CO₂ injection. The detailed workflow follows:

- 1) *Determination of CO₂ plume half-length:* The distribution of CO₂ saturation helps visualize the migration of the CO₂ plume. We define the arrival of CO₂ plume when the CO₂ saturation at a given location is larger than a prescribed saturation threshold. Thus, by setting a saturation threshold, we can get a corresponding CO₂ plume half-length at a given time. Summarizing all the CO₂ plume half-lengths at various times yields the relationship shown in Figure 5.7a. The three curves in Figure 5.7a correspond to saturation thresholds of 0.001, 0.01, and 0.1. For example, the CO₂ plume half-length is ~400 m after 600 days of injection when the saturation threshold is ~0.1. Different saturation thresholds yield slightly different CO₂ plume half-lengths as a function of time. The CO₂ plume half-length decreases ~50 meters when the saturation threshold is adjusted from 0.001 to 0.1.
- 2) *Determination of the IZ ΔP front:* Let us define the IZ pressure front when the IZ ΔP at a given location is larger than a prescribed threshold. Figure 5.7a shows three curves of the pressure front evolution prescribed thresholds of 1,000 kPa, 1,200 kPa, and 1,400 kPa. Comparing the advance of the CO₂ plume half-length, we can see that the 1,200-kPa-pressure front moves simultaneously with the migration of the CO₂ plume and thus the IZ ΔP induced by the CO₂ front is 1,200 kPa in this particular case.

3) *Determination of the CO₂ plume arrival from AIZ ΔP/IZ ΔP ratio:* Figure 5.6 demonstrates that the AIZ ΔP/IZ ΔP depends mainly on time (after injection) rather than horizontal distance to the injector (particularly when the horizontal distance is less than 100 m). Hence, we can use the AIZ ΔP/IZ ΔP ratio to identify the CO₂ arrival from AIZ measurements (Figure 5.7b). For example, at a given location AIZ ΔP/IZ ΔP (i) first increases until reaching the sky-blue markers (CO₂ has not arrived yet), (ii) increases further until reaching the blue marker (CO₂ has arrived). Afterward, AIZ ΔP/IZ ΔP decreases due to pore pressure dissipation. The blue markers are an upper-bound limit for AIZ ΔP/IZ ΔP. A larger value is not possible in the absence of leaks. For example, a ratio AIZ ΔP/IZ ΔP > 1.5% in AIZ 5 might indicate hydraulic communication, and therefore a potential leak. This method requires knowing IZ ΔP, which might be approximated from reservoir simulation.

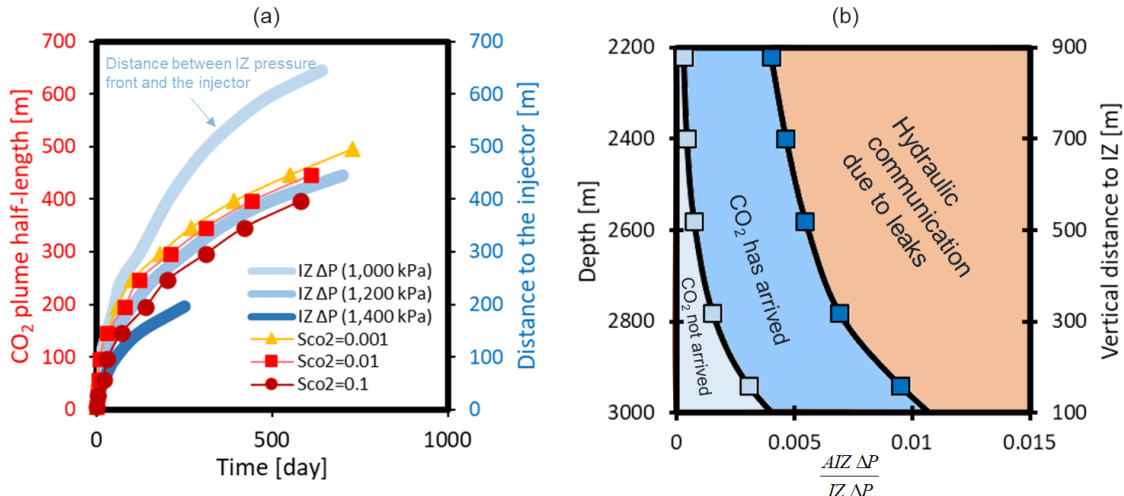


Figure 5.7: Tracking of CO₂ plume location with AIZ pressure monitoring. (a) CO₂ plume half-length: the migration of CO₂ plume is tracked through CO₂ saturation. The 1,200 kPa pressure front in the IZ moves simultaneously with the CO₂ plume for a constant injection rate. (b) Prediction of CO₂ arrival using the ratio between AIZ ΔP and IZ ΔP at the same horizontal distance from the injector.

5.4 DISCUSSION: SUBSURFACE LEAKAGE DETECTION

5.4.1 Presence of a leaky fault

As an extension of our base case with no leaks, let us consider the existence of a fault with high permeability and its influence on the AIZ pore pressure. A high permeability fault is set at a distance of 181 m from the injector. We model the fault as a wall of grid blocks with a width of 3 m and volume-average permeability equal to 1,000 mD (Childs et al., 2007; Faulkner et al., 2010; Tao et al., 2012). The fault permeability can also be calculated through the SGR-based approach in Chapter 3 or the PSSF-based approach in Chapter 4. An example fault populated with the SGR-based and the PSSF-based permeability is modeled in Appendix A10. Figure 5.8a compares the pressure increase in five AIZs monitored along the injector and the base case. The solid line represents the results from the leaky fault case and the dashed line represents the results from the base case.

The AIZ pressure increase in the base case with no leak is induced primarily by partially undrained loading. However, the AIZ pressure increase in the leaky fault case is the result of the combined effects of direct hydraulic communication and partially undrained loading (Equation 5.1). The key features in Figure 5.8a include:

- The pore pressure change due to partially undrained loading in the base case exhibits a pressure increase in the first 10 days and then starts to decay due to pore pressure dissipation within the AIZ. However, the presence of leaks favors more gradual increases of pore pressure to higher peak values until injection shut-in (2 years). This additional and sustained pressure increase is the result of fluid communication between the IZ and the AIZ through the fault.

- The pressure trends in the base and leaky cases overlap with each other in the first 10 days of CO₂ injection before the partially undrained loading reaches the maximum value. After that, the pressure deviation between the two cases gradually becomes more and more significant. The AIZ ΔP in the leaky case is one order of magnitude larger than the base case with no leaks after one year of injection. Direct fluid communication increases AIZ pore pressure ten times more than partially undrained loading after 2 years.
- The pressure buildup due to the hydraulic communication takes time and thus more distant regions exhibit a longer delay in pore pressure increase. The time delay in sensing the leak at different monitoring points helps assess reservoir integrity.

Let us also monitor the evolution of CO₂ saturation along the fault. The buoyancy of bulk CO₂ leads to the rise of CO₂ through the fault and AIZ layers, and thus the pressure in the AIZ 1 is higher than the pressure in other AIZs after two years of CO₂ injection. Here we define the CO₂ arrival at a specific AIZ when CO₂ saturation at the measured point is higher than 0.01 (Figure 5.8b). Considering the intersections between the horizontal threshold line (0.01) and each CO₂ saturation curve (Figure 5.8b), the CO₂ arrival time for five AIZs is 100, 140, 200, 250, 310 days. Thus, leakage detection through saturation monitoring requires at least several months. The AIZ pressure increase occurs before the change of CO₂ saturation and provides earlier warnings than compositional monitoring at a potential observation well near the fault.

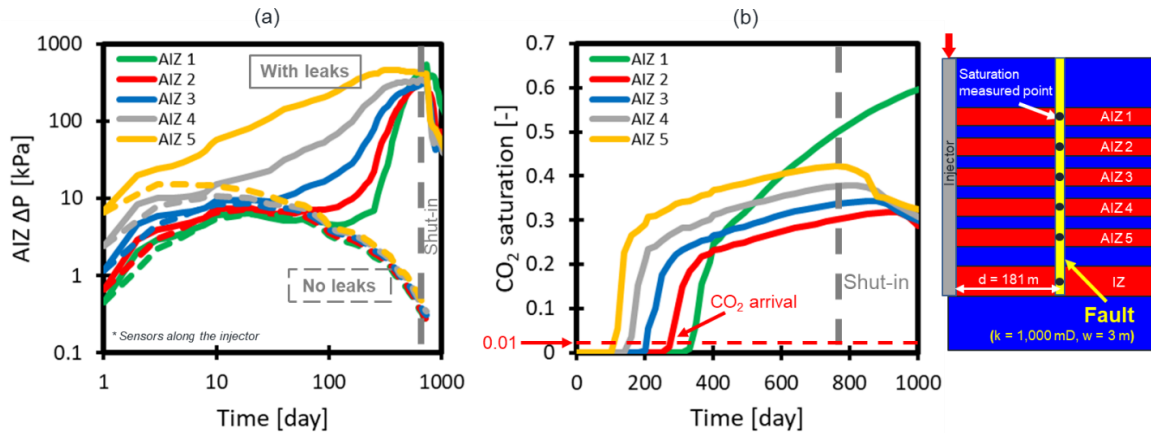


Figure 5.8: Evolution of pore pressure and CO_2 saturation above the injection zone in the presence of a leaky fault: (a) pressure increase in five AIZs along the injector, including the case with no leaks and the case with a leaky fault; (b) CO_2 saturation in five AIZs along the fault. A leaky fault results in steady and higher increases in AIZ pressure than the base case.

The pressure distribution in Figure 5.9 is the result of a leaky fault (compare to the base case in Figure 5.5a). The leaky path releases pressure from the injection zone and has the highest AIZ ΔP in each AIZ. The AIZ ΔP decays with the increase of distance to the leaky fault. A rough estimation of the leakage location is possible through pressure monitoring and mapping in the AIZ. In this case, the estimated leakage location based on the perturbations of pore pressure is about 180 m away from the injector, which coincides with the actual fault location (the leakage location has the highest AIZ ΔP in each AIZ). Increasing the number of monitoring wells is expected to provide useful information on the estimation of the extent of subsurface leakages (Zeidouni & Pooladi-Darvish, 2012b). This simple example can be extended into a formal inverse problem to detect leaky pathways with arbitrary geometry.

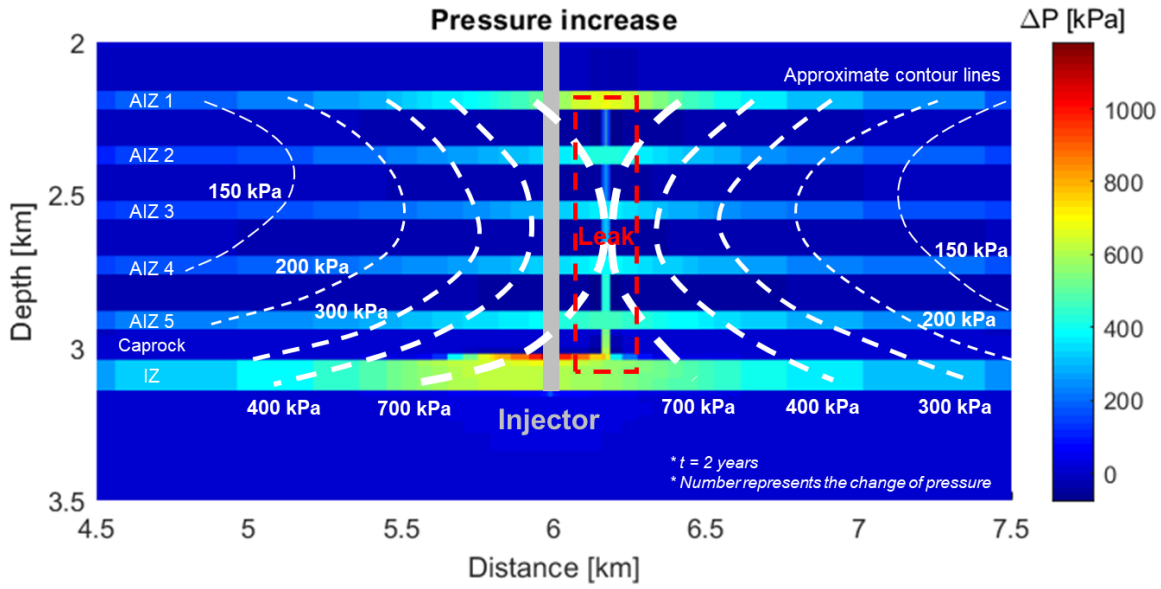


Figure 5.9: Pressure change above the injection zone (AIZ) in the presence of a leaky fault. The red dashed box highlights the estimated leaky path based solely on the observed pore pressure field, which coincides with the location of the leaky fault.

5.4.2 Other relevant scenarios

In this section, we discuss the AIZ pressure increase in other relevant subsurface scenarios. Figure 5.10 presents the distribution of CO₂ plume after two years of injection in six different cases, including (1) base case, (2) case with a sealing fault, (3) case with a leaky fault, (4) case with a leaky abandoned well, (5) case with a leaky injector, and (6) case with two injectors. The leaky fault, the sealing fault, the leaky abandoned well, and the second injector are placed at a distance of 181 m from the primary injector. The effective (volume average) permeability of all the leaky grid blocks is 1,000 mD with a thickness of 3 m. The fault permeability has three different values ($k_{fault} = 10, 100, \text{ and } 1,000 \text{ mD}$) in the leaky fault case for a sensitivity test. The top of the AIZ 1 is overlain by a thick fully sealing caprock. The black dots along the primary injector in Figure 5.10 represent the location of pressure monitoring sensors.

The CO₂ plume half-length is 533 m in the base case (cut-off S_{CO₂}=1%). The presence of leaks reduces the CO₂ plume half-length in all leaky cases. The CO₂ plume half-length is the shortest (only 427 m) in the leaky injector case. The AIZ 5 is closest to the injection zone and thus the CO₂ saturation in the AIZ 5 is higher than other AIZs. The sealing fault inhibits CO₂ flow on one side and results in preferential CO₂ migration opposite to the fault location.

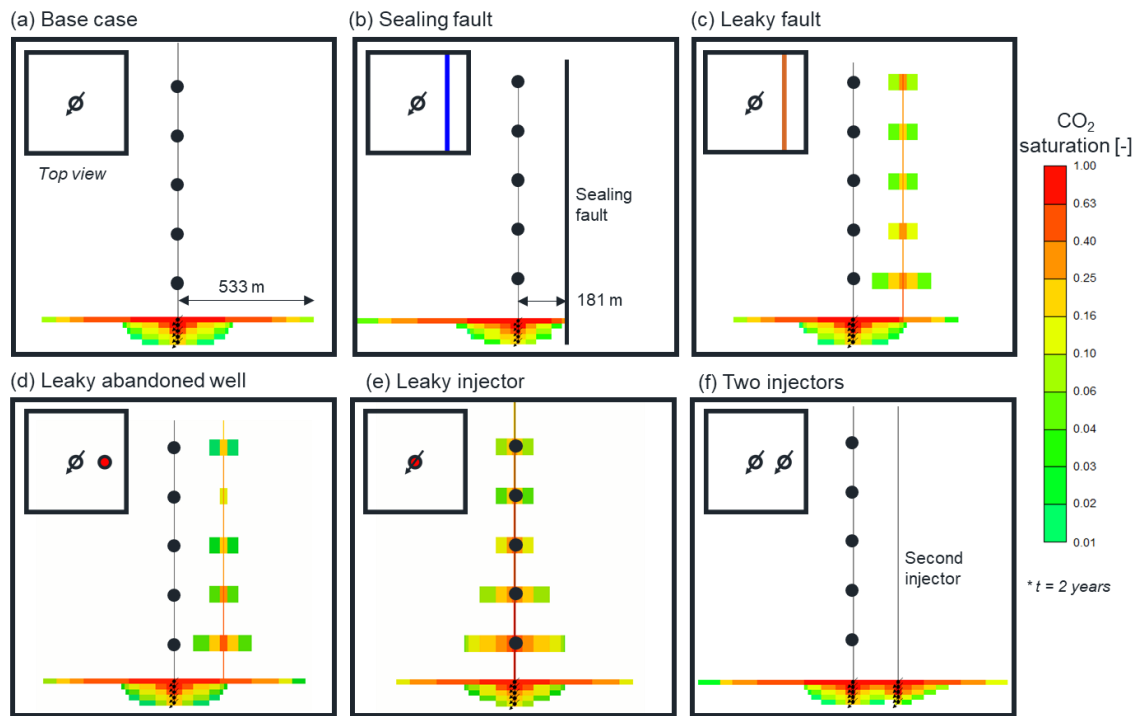


Figure 5.10: Distribution of CO₂ plume after two years of CO₂ injection in different scenarios: (a) base case with no leaks; (b) case with a sealing fault; (c) case with a leaky fault; (d) case with a leaky abandoned well; (e) case with a leaky injector; and (f) case with two injectors. The inserted plot at the top left of each sub-figure represents the schematic top-view of each layout.

Figure 5.11 shows the AIZ pressure increase for the different cases shown in Figure 5.10. The presence of leaks results in the AIZ pressure change in the range of 100 to 1,000 kPa, while pressure increase due to partially undrained loading is characterized by lower

values (in the order of magnitude of 10 kPa). The leaky injector has the most significant effect on pore pressure changes along the well compared with other leaky scenarios. The leaky abandoned well is 181 m away from the injector and thus exhibits a delay in pressure increase compared with the leaky injector case. The response for the abandoned-well case overlaps with the response for the base case at the initial stage ($t < 90$ days), suggesting direct fluid flow has not yet arrived at the abandoned well and the primary reason for pressure change is due to partially undrained loading. Afterward, continuous hydraulic communication leads to faster and higher pressure increases.

Variations in fault permeability can result in distinct responses in the AIZ. A permeable fault favors faster fluid communication and higher AIZ pressure increase than the fault with lower permeability. The pressure increase is one order of magnitude smaller for the case with $k_{fault} = 10$ mD than for $k_{fault} = 1,000$ mD. However, if the fault permeability is small enough to inhibit fluid flow (for example, 10 nD), structural sealing will favor a stronger undrained loading above the reservoir and thus higher pressure increase in the AIZ (as large as 30 kPa) than the base case with no leaks.

The addition of the second injector increases the ΔP by 12 kPa in the first five days after the second injector starts injection ($t = 1$ year), as the cumulative result of partially undrained loading and of the simultaneous injection process. The increase of pressure induced by undrained loading indeed follows the principle of superposition (Roussel & Agrawal, 2017), consistently with the assumed poroelastic behavior of the rocks. Understanding distinct features of pressure increase with or without leaks can help identify potential leaks into the AIZ.

The transient poroelastic response in the field depends on fluid injection rate and injection schedule. A large injection rate entails fast pressure buildup in the IZ and thus triggers a strong pressure response in the AIZ. For a given injected volume, a step-wise

increase of injection rate will mitigate the pore pressure increase from partially undrained loading as increases of volumetric strain happen at the same time pore pressure dissipates in the AIZ. The discussion about the injection scheme and field validation is out of the scope of this study.

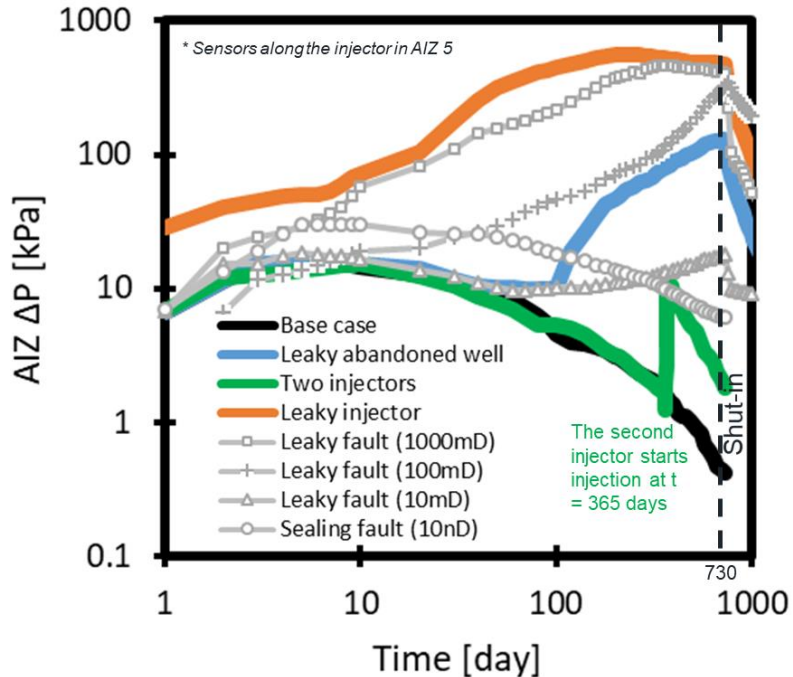


Figure 5.11: Pore pressure increases above the injection zone for different storage scenarios shown in Figure 5.10. The fault permeability varies from 10 nD to 1,000 mD. The effective permeability of leaky blocks in other leaky scenarios is 1,000 mD.

5.5 CONCLUSIONS

This study presents numerical simulation results of CO₂ injection and corresponding pore pressure changes above the injection zone (AIZ) due to partially undrained loading and hydraulic communication, in views of CO₂ plume tracking and leak monitoring. The major conclusions are:

- The pore pressure increase induced by partially undrained loading in the AIZ is non-negligible. The AIZ pressure increase is up to 1% of the injection zone (IZ) pressure increase for the chosen reservoir model. The poroelastic responses induced by partially undrained loading are cumulative and time-dependent. AIZ pressure increase due to partially undrained loading is maximum when rapid changes of pressure occur in the IZ, such as in the initial stage of injection for a constant injection rate schedule.
- The reach of AIZ ΔP caused by partially undrained loading depends on reservoir/injector geometry and decreases quickly with distance to the injector and time in the chosen single-injector and laterally extensive model. Pressure sensors installed within ~ 160 m away from the injection point may detect a pore pressure increase larger than 15 kPa for the chosen reservoir model. Observation wells should be placed within ~ 880 m of the injection point to ensure the detected pressure is larger than the background noise ($\Delta P > 4$ kPa).
- Changes of pressure in the IZ (due to CO₂ injection) increase the AIZ pressure by 0.1% to 1% of the IZ pressure due to partially undrained loading (in the absence of leaks). Moreover, the IZ pressure is linked to the migration of the CO₂ plume. Hence, it is possible to use AIZ ΔP to track the migration of the CO₂ plume in the IZ.
- The AIZ ΔP in cases with leaks can be one order of magnitude larger than the case without leaks. The pore pressure change due to undrained loading builds up to the peak (~ 15 kPa) within ~ 10 days followed by a gradual decay with time (due to pore pressure diffusion), while the presence of leaky pathways favors a higher, yet more gradual, pressure increase in the AIZ through direct fluid communication ($\Delta P = 100$ to 1,000 kPa).

- A permeable fault favors faster fluid communication and higher pressure increase in the AIZ than a fault with lower permeability. On the other hand, a sealing fault favors strong reservoir sealing and results in a higher pressure increase due to partially undrained loading in the AIZ than the case with no fault.
- AIZ pressure monitoring can be an effective technique to track the extent of the CO₂ plume, detect potential leaks, and provide earlier leak warnings than compositional fluid monitoring. Unexpected pressure increases in the AIZ pressure (above the range expected for partially undrained loading) are an indication of leaks from the injection zone into overlying formations.

Chapter 6: Conclusions

This dissertation presents the evaluation of reservoir injectivity, the assessment of reservoir sealing capacity, and the associated monitoring of subsurface leakages in CO₂ geological storage. Chapter 2 examines the isotropic compressibility and the uniaxial strain compressibility of Frio sand during the loading and unloading cycles. The results help the estimation of potential risks associate with CO₂ injection. The experimental measurements on synthetic fault gouge samples in Chapter 3 yield absolute permeability, CO₂ breakthrough pressure, and post-breakthrough CO₂ permeability as a function of clay content. A stochastic method based on the probabilistic distribution of shale smears is developed in Chapter 4 to predict the maximum CO₂ column height in shale-sand sedimentary sequences exemplified by a case in the High Island field in Texas. The evaluation of the transport properties of fault gouge and the trapped CO₂ column height permits the quantification of reservoir sealing potential. Finally, Chapter 5 investigates pore pressure changes due to partially undrained loading in the above-injection-zone (AIZ) during CO₂ injection and validates the feasibility of using AIZ pressure monitoring to detect subsurface leakages in CO₂ storage.

The major conclusions of this dissertation are:

- CO₂ injection induces pore pressure buildup and may result in the re-activation of sealing faults. Uniaxial strain unloading compressibility can better capture reservoir deformation and pressure increase than conventional isotropic loading compressibility and should be used in reservoir simulation of CO₂ injection. The uniaxial strain unloading compressibility increases non-linearly from 0.29 to 1.45 GPa⁻¹ (2 to 10 μ sip) as the mean effective stress is reduced from 26 to 5 MPa. The uniaxial strain unloading compressibility of Frio sand is about one-third of the

uniaxial strain loading compressibility at comparable levels of effective stress. The uniaxial strain compressibility of Frio sand is roughly one-half of the isotropic compressibility. Reservoir simulation further confirms that using incorrect pore compressibility values considerably underestimates the expected increase of pore pressure in a compartmentalized formation during CO₂ injection.

- Faults are key components in defining CO₂ migration pathways in CO₂ storage. The sealing capacity of faults is closely related to clay content in fault gouge. The permeability of synthetic fault gouge decreases by about one order of magnitude with increments of 10 wt% of clay from the Anahuac shale. All permeability measurements scale with the void ratio of the clay fraction, rather than bulk porosity. The breakthrough pressure of synthetic fault gouge increases by approximately half order of magnitude when adding 10 wt% clay. The samples with clay content above 40 wt% reach a breakthrough pressure equivalent to a (supercritical) CO₂ column height of more than 100 m. The measurements on fault gouge properties are meaningful to quantitatively evaluate fault sealing capability and migration of buoyant fluids through faults in sand-shale sequences.
- The Probabilistic Shale Smear Factor (PSSF) based method accounts for the ductility of clay smears and statistically determines the possible range of CO₂ column height at a normal fault in sand-shale sequences. Small fault throws lead to a reduction in the number of leak points across faults and therefore an increase of maximum CO₂ column height. In the selected case study in the High Island Field, about 98% of the realizations for a small fault throw (less than 217.5 ft) predict a column height less than 50 ft. However, large fault throws result in smear breaches and therefore in highly variable maximum CO₂ column heights, varying from 0 ft to a maximum of ~155 ft. The PSSF-based method incorporates the effects of the

ductility and continuity of clay smears and permits explaining the variability of column heights observed in the field that are less straightforward to predict with the SGR-based method.

- Pressure monitoring above the injection zone is a method to track the CO₂ plume and detect potential CO₂ leaks into overlying formations. Changes of pore pressure above the injection zone caused by partially undrained loading can be as large as ~1% of the pressure increase in the injection zone for the chosen reservoir model and initial properties. Pressure sensors should be installed within ~880 m from the injection point to ensure the detected pressure is larger than the background noise ($\Delta P > 4$ kPa). The pore pressure in the above injection zone increases due to partially undrained loading up to a maximum value of ~15 kPa within ~10 days followed by a gradual decay with time in the absence of leaks, while CO₂ migration through leaky paths favors a higher (typically one order of magnitude larger) yet more gradual pressure increase above the injection zone through direct fluid communication. Poroelastic monitoring is a feasible technology to track the CO₂ plume but requires high precision pressure measurements.

The geomechanical and petrophysical studies in this dissertation aim to reduce the risk associated with CO₂ geological storage. The long-term secure storage of CO₂ in the subsurface relies on good reservoir injectivity, reliable reservoir sealing capacity, and effective monitoring of subsurface CO₂ plume. Thus, a systematic design for CO₂ storage should consider (1) allowable CO₂ injection pressure to avoid injection-induced fault reactivation or fracturing, (2) potential leaky faults or weak planes that serve as fluid migration paths, and (3) how to detect (and manage) those unintended subsurface leakages.

Future work for this dissertation should address more realistic scenarios, including (1) complex fault zone architecture (such as the presence of cataclasis, granular flow,

multiple fault cores, and multiple deformation bands); (2) heterogeneous fault gouge (i.e., using real gouge cores rather than synthetic homogeneous gouge samples); (3) evolution of clay smear ductility and thickness; (4) clay swelling and its sensitivity to salinity, pH, and flow conditions; (5) mineral trapping due to CO₂-rock-mineral interactions; (6) residual trapping as a function of CO₂ saturation; (7) CO₂ adsorption and desorption; (8) permeability healing induced by calcite precipitation; (9) permeability dependency on fluid flow direction and in-situ stress condition; and (10) variable CO₂ injection schemes (which replicate a field case). Together, it is critical to building a CO₂ storage model that can predict the phenomena in different scales (including pore-scale, core-scale, and reservoir-scale) and explain various thermo-mechano-chemo-hydro coupled processes in the subsurface system.

Appendix

A1 MEASUREMENT OF BIOT COEFFICIENT

Figure A1 shows the stress path for measuring the Biot coefficient. The Biot coefficient is obtained as 0.944 through the regression analysis when the curves of $P_c - P_p$ as a function of volumetric strain collapse into one curve (Figure A2).

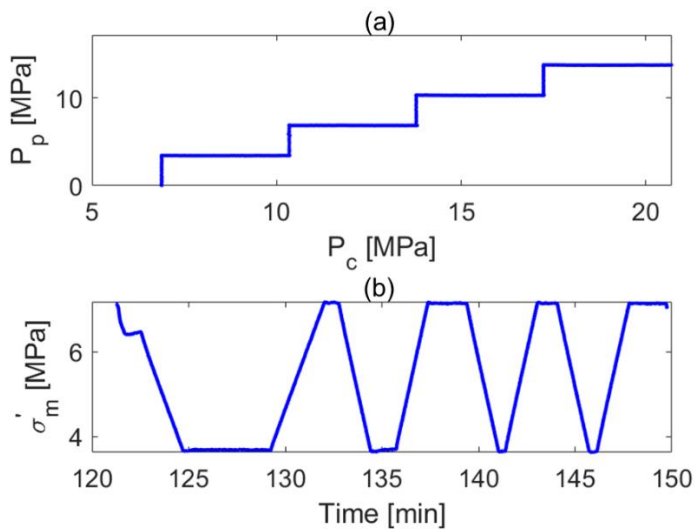


Figure A1: Stress path for the Biot coefficient test.

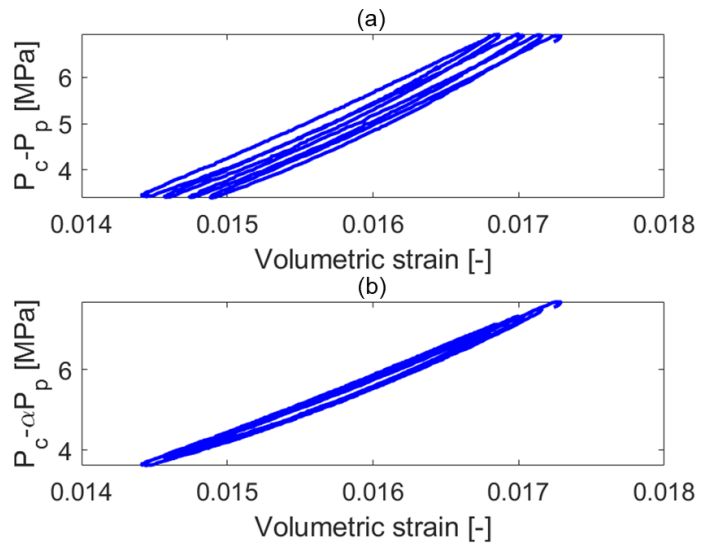


Figure A2: Regression analysis for the Biot coefficient test.

A2 UNIAXIAL STRAIN COMPRESSIBILITY IN THE LONG UNLOADING PATH

The slope of the unloading curve depends on the amount of the unloaded stress. The unloading path turns to be flatter when more stress is unloaded (test 3 in Figure 2.3). The sample starts to follow four long unloading paths when the effective axial stress reaches the maximum value (~45 MPa). Compared with the tangent modulus, the secant constrained modulus, which is defined as the slope between the initial unloading point and the endpoint (see the top inserted figure in Figure A3), can better capture the pore pressure change with large stress relief due to CO₂ injection. For example, the corresponding uniaxial strain compressibility is 1.02 GPa⁻¹ and 1.31 GPa⁻¹, respectively, when the mean effective stress, starting from 6.14 MPa in the fourth unloading path (Figure A3), is reduced to 5 MPa and 3 MPa. A large amount of the unloaded stress could result in high unloading compressibility. Thus, particular attention should be paid to continuous CO₂ injection with large unloaded stress for selecting suitable compressibility.

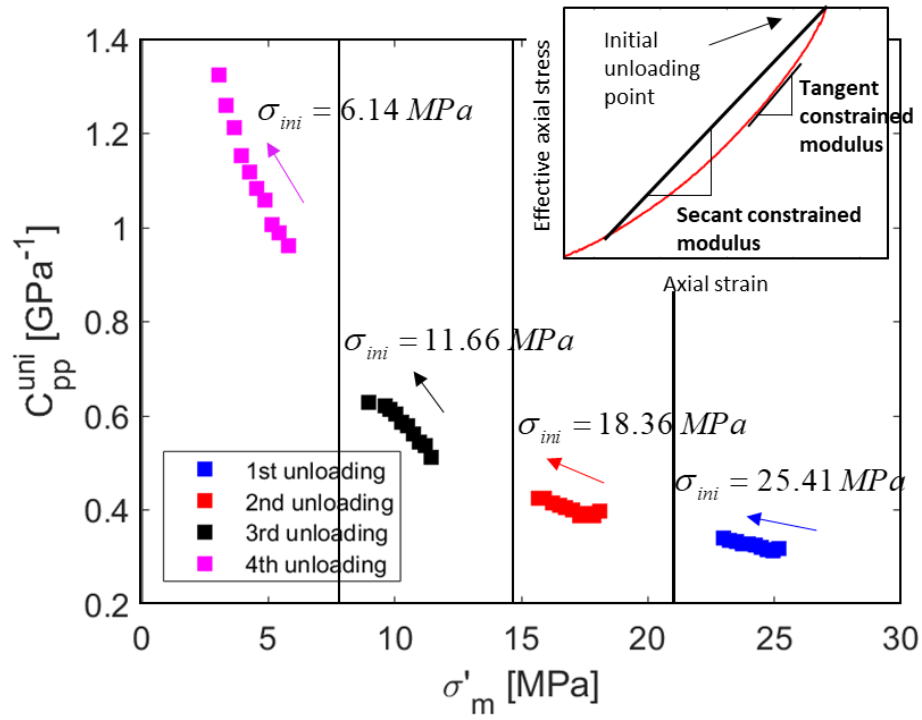


Figure A3: Uniaxial strain compressibility in the long unloading path (sample 5053.2D): the secant constrained modulus is defined to describe the compressibility change with large unloaded stress; the plot summarizes the compressibility in four long unloading paths with different initial stress.

A3 DERIVATION OF THE RELATIONSHIP BETWEEN ISOTROPIC COMPRESSIBILITY AND UNIAXIAL STRAIN COMPRESSIBILITY

This appendix presents the theoretical derivation for the relationship between isotropic compressibility and uniaxial strain compressibility. Hooke's law of linear poroelasticity is generally expressed as:

$$\sigma - \alpha P_p \mathbf{I} = 2G\varepsilon + \frac{2G\nu}{1-2\nu} \text{trace}(\varepsilon) \mathbf{I} \quad (\text{A1})$$

Taking the differentials of Equation A1, Equations 2.3a and 2.3b become $C_{bc}^{uni} = \frac{1}{\lambda + 2G}$ and $C_{bp}^{uni} = \frac{\alpha}{\lambda + 2G}$, which can be written as

$$\begin{cases} C_{bc}^{uni} = \frac{(1+\nu)}{3(1-\nu)K} \\ C_{bp}^{uni} = \frac{\alpha(1+\nu)}{3(1-\nu)K} \end{cases} \quad (A2a)$$

$$C_{bp}^{uni} = \frac{\alpha(1+\nu)}{3(1-\nu)K} \quad (A2b)$$

The boundary condition of C_{bc}^{uni} and C_{bp}^{uni} implicitly implies that $K = (K)_{P_p=cst}$ in Equation A2a and $K = (K)_{\sigma_{zz}=cst}$ in Equation A2b. The definition of bulk modulus is:

$$K = \frac{\Delta\sigma_m^{eff}}{\Delta\varepsilon_b} \quad (A3)$$

where the expression of the mean effective stress is derived in Equation 2.5. As discussed in section 2.1, there are two boundary conditions for isotropic compressibility.

For the first case, P_c is a variable while σ_D and P_p are constants. Hence, Equation 2.5 yields $\Delta\sigma_m^{eff} = \Delta P_c$, which changes Equation A3 into $K = \frac{\Delta P_c}{\Delta\varepsilon_b}$. According to Equation 2.2a, we have

$$(K)_{P_p=cst} = \frac{1}{C_{bc}^{iso}} \quad (A4)$$

If we assume constant overburden pressure and a constant Biot coefficient, $\sigma_{zz}^{eff} = \sigma_{zz}^{total} - \alpha P_p$ gives $\sigma_{zz}^{eff} = cst$. Therefore,

$$(K)_{\sigma_{zz}^{eff}=cst} = \frac{1}{C_{bc}^{iso}} \quad (A5)$$

For the second case, P_p is a variable while P_c and σ_D are constants. Equation 2.5 yields $\Delta\sigma_m^{eff} = \Delta P_p$, which changes Equation A3 into $K = \frac{\Delta P_p}{\Delta\varepsilon_b}$. According to Equation 2.2b, we have

$$(K)_{P_c=cst} = \frac{1}{C_{bp}^{iso}} \quad (A6)$$

Substituting Equation A4 and Equation A6 into Equation A2a and Equation A2b, respectively, yields Equations A7a and A7b:

$$\left\{ \begin{array}{l} C_{bc}^{uni} = \frac{(1+\nu)}{3(1-\nu)} C_{bc}^{iso} \end{array} \right. \quad (A7a)$$

$$\left\{ \begin{array}{l} C_{bp}^{uni} = \alpha \frac{(1+\nu)}{3(1-\nu)} C_{bc}^{iso} \end{array} \right. \quad (A7b)$$

$$\left\{ \begin{array}{l} C_{pc}^{uni} = \frac{(1+\nu)}{3(1-\nu)} C_{pc}^{iso} \end{array} \right. \quad (A7c)$$

$$\left\{ \begin{array}{l} C_{pp}^{uni} = C_{pp}^{iso} - \frac{2(1-2\nu)\alpha}{3(1-\nu)} (C_{pp}^{iso} + C_m) \end{array} \right. \quad (A7d)$$

where Equations A7c and A7d are given in the literature (Zimmerman, 2000a, 2017). In addition, the relationships among four isotropic compressibilities (Jaeger et al., 2009) are derived as

$$\left\{ \begin{array}{l} C_{bp}^{iso} = C_{bc}^{iso} - C_m \end{array} \right. \quad (A8a)$$

$$\left\{ \begin{array}{l} C_{pp}^{iso} = C_{pc}^{iso} - C_m \end{array} \right. \quad (A8b)$$

$$\left\{ \begin{array}{l} C_{bp}^{iso} = \phi C_{pc}^{iso} \end{array} \right. \quad (A8c)$$

Equation A7 shows the relationships between isotropic compressibility and uniaxial strain compressibility. Combined Equations A7 and A8, the pore volume compressibility is derived as:

$$\left\{ \begin{array}{l} C_{pc}^{uni} = \frac{\alpha}{\phi M} \end{array} \right. \quad (A9a)$$

$$\left\{ \begin{array}{l} C_{pp}^{uni} = \frac{-2(1-2\nu)\alpha^2 + 3(1-\nu)[\alpha(1+\phi)-\phi]}{\phi(1+\nu)M} \end{array} \right. \quad (A9b)$$

If the rock matrix is incompressible ($C_m = 0$), $K_m = \infty$. According to the definition of Biot coefficient ($\alpha = 1 - \frac{K}{K_m}$), $\alpha = 1$. Equations A7, A8, and A9 are rewritten as

$$\left\{ \begin{array}{l} C_{bc}^{uni} = \frac{(1+\nu)}{3(1-\nu)} C_{bc}^{iso} \\ C_{bp}^{uni} = \frac{(1+\nu)}{3(1-\nu)} C_{bp}^{iso} \end{array} \right. \quad (A10a)$$

$$\left\{ \begin{array}{l} C_{pc}^{uni} = \frac{(1+\nu)}{3(1-\nu)} C_{pc}^{iso} \\ C_{pp}^{uni} = \frac{(1+\nu)}{3(1-\nu)} C_{pp}^{iso} \end{array} \right. \quad (A10b)$$

$$\left\{ \begin{array}{l} C_{bc}^{iso} = C_{bc}^{uni} \\ C_{pp}^{iso} = C_{pc}^{uni} \end{array} \right. \quad (A10c)$$

$$\left\{ \begin{array}{l} C_{bp}^{iso} = \phi C_{pc}^{uni} \\ C_{bp}^{iso} = \phi C_{pc}^{iso} \end{array} \right. \quad (A10d)$$

$$C_{bp}^{iso} = C_{bc}^{iso} \quad (A11a)$$

$$C_{pp}^{iso} = C_{pc}^{iso} \quad (A11b)$$

$$C_{bp}^{iso} = \phi C_{pc}^{iso} \quad (A11c)$$

$$C_{pp}^{uni} = C_{pc}^{uni} = \frac{C_{bp}^{uni}}{\phi} = \frac{C_{bc}^{uni}}{\phi} = \frac{1}{\phi M} \quad (A12)$$

Equations A10 and A11 also give the relationships among four uniaxial strain compressibility as:

$$\left\{ \begin{array}{l} C_{bp}^{uni} = C_{bc}^{uni} \\ C_{pp}^{uni} = C_{pc}^{uni} \end{array} \right. \quad (A13a)$$

$$\left\{ \begin{array}{l} C_{bp}^{uni} = \phi C_{pc}^{uni} \\ C_{bp}^{uni} = \phi C_{pc}^{iso} \end{array} \right. \quad (A13b)$$

$$\left\{ \begin{array}{l} C_{bp}^{uni} = \phi C_{pc}^{iso} \\ C_{bp}^{uni} = \phi C_{pc}^{iso} \end{array} \right. \quad (A13c)$$

We rigorously demonstrate the underlying assumptions, prerequisites, as well as boundary conditions for uniaxial strain compressibility and isotropic compressibility, although most of the equations above were given somewhere in the literature. Equation A10 shows an analytical relationship between uniaxial strain compressibility and isotropic compressibility as:

$$C_{bp}^{uni} = \frac{(1+\nu)}{3(1-\nu)} C_{bp}^{iso} \quad (A14)$$

A4 SCHEMATIC DIAGRAM OF CONSOLIDATION SETUP

Figure A4 shows the structure of the improved consolidation setup. The new consolidation cell can accommodate high axial stress under uniaxial strain conditions.

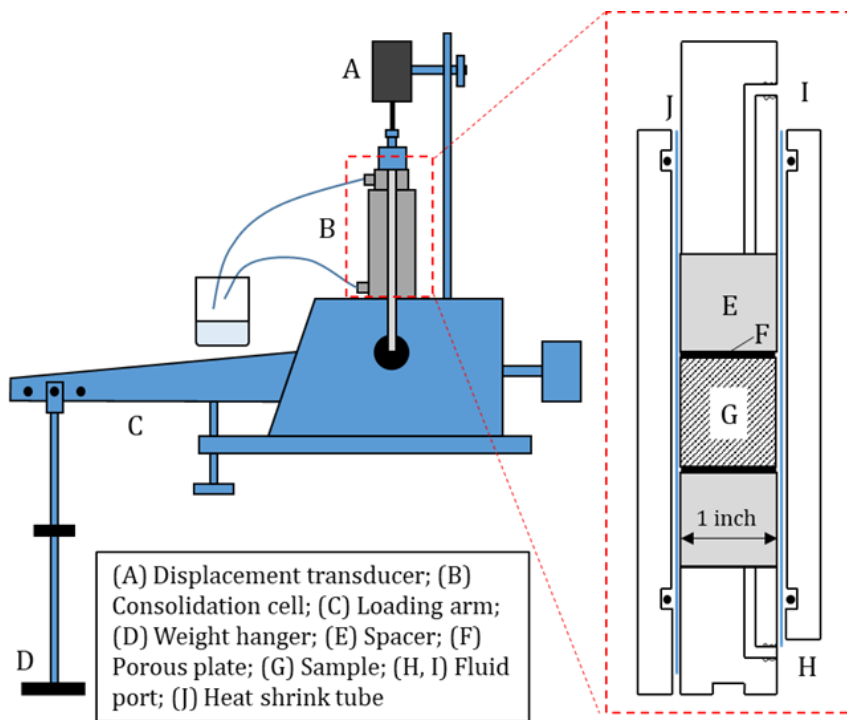


Figure A4: Structure of the improved consolidation setup.

A5 PRESSURE STEPS IN CO₂ BREAKTHROUGH PRESSURE TESTS

Table A1 summarizes the pressure steps applied for each sample in CO₂ breakthrough pressure tests. The *NB* in the table refers to "no breakthrough" and *B* refers to "CO₂ breakthrough".

Table A1: Pressure steps in CO₂ breakthrough pressure tests.

Sample	Time [hour]	P _p [psi]	Status
CS-30 (10% clay)	0	1.5	NB
	1.8	1.5	NB
	1.8	7.3	B
CS-28 (20% clay)	0	6	NB
	5	6	NB
	5	15	B
CS-26 (30% clay)	0	10	NB
	24	10	NB
	24	33	NB
	45	33	NB
	45	70	B
CS-29 (40% clay)	0	0.5	NB
	1.7	0.5	NB
	1.7	43	NB
	4.8	43	NB
	4.8	89	NB
	23	89	NB
	23	165	NB
	102	120	NB
	102	331	NB
	156	301	NB
	156	486	B
	0	168	NB
CS-27 (50% clay)	82	168	NB
	82	346	NB
	265	346	NB
	265	637	B
	0	50	NB
CS-32 (90% clay) and CS-31 (70% clay)	22	50	NB
	22	110	NB
	50	110	NB
	50	320	NB
	93	320	NB
	93	409	NB
	141	409	NB
	141	560	NB
	213	516	NB
	213	700	NB
	309	698	NB
	309	830	NB
	690	824	NB
	690	884	NB
	738	870	NB
	738	1010	NB
	951	950	NB
	951	1178	NB
	1200	1147	NB

A6 COMPARISON BETWEEN NATURAL GAS COLUMN AND CO₂ COLUMN IN THE HIGH ISLAND FIELD

Brown (2011) delineates natural gas-water contacts in the structure map of the HC Sand in the High Island 24L field (Figure A5). The height of natural gas columns is up to 250 ft (Brown, 2011; Fowler et al., 1987; Ruiz, 2019). Based on the Young-Laplace equation, the methane column height can be converted into the CO₂ column height as below:

$$h_{CO_2} = h_{methane} \frac{\sigma_{CO_2-brine} \cos \theta_{CO_2-brine} (\rho_w - \rho_{methane})}{\sigma_{methane-brine} \cos \theta_{methane-brine} (\rho_w - \rho_{CO_2})} \quad (A15)$$

Substituting typical values into the above equation (Arif et al., 2021; Kashefi et al., 2016), we get $h_{CO_2} \approx 0.7h_{methane}$. Thus, the corresponding maximum CO₂ column height in the High Island 24L field would be 175 ft, which matches with the predicted CO₂ column height in this field (Figure 4.6 in the dissertation).

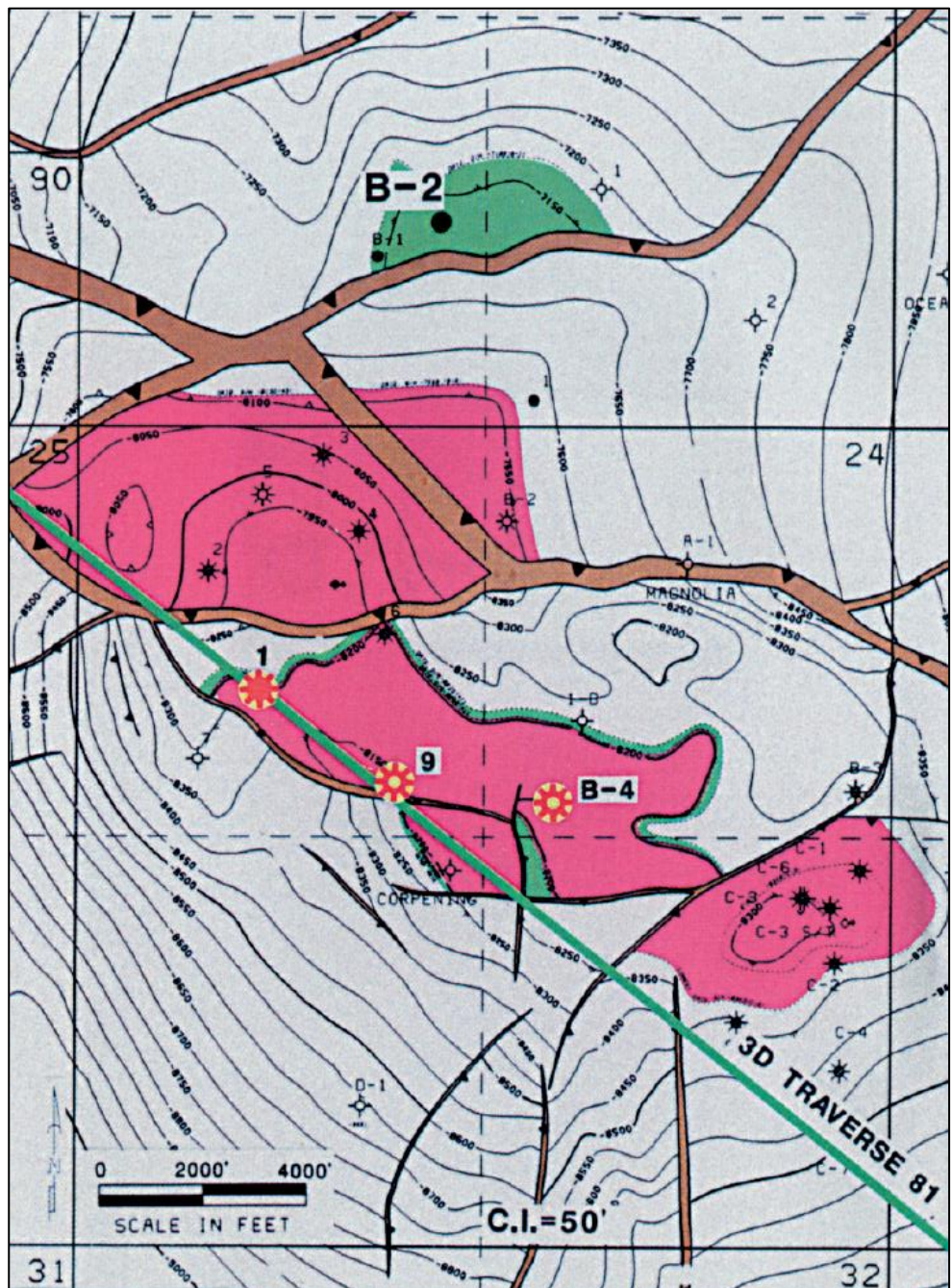


Figure A5: Structure map of the HC Sand in the High Island 24L Field: the distribution of natural gas is highlighted in pink (Brown, 2011).

A7 COUPLING BETWEEN FLUID FLOW AND GEOMECHANICS

This appendix outlines the basic equations for the coupling between fluid flow in porous media and geomechanics. Darcy's equation and the mass balance equation are (Coussy, 2004; Peters, 2012):

$$v = -\frac{k}{\mu_f} \nabla P \quad (\text{A16})$$

$$\frac{\partial(\phi\rho)}{\partial t} = \nabla \cdot (\rho v) + q \quad (\text{A17})$$

where μ_f is the fluid viscosity, k is the rock permeability, and v is the fluid velocity. For a slightly compressible fluid, the fluid density (ρ) and formation volume factor (B_f) are functions of fluid pressure (P) and fluid compressibility (C_f) (Cheng, 2016; Ebin, 2018):

$$\rho = \rho_i [1 + C_f (P - P_i)] \quad (\text{A18})$$

$$B_f = \frac{B_{f_i}}{[1 + C_f (P - P_i)]} \quad (\text{A19})$$

The conventional flow simulators typically assume that the porous media grid does not deform, while geomechanical simulators require the rock deformation. The mass conservation equation for fluid flow in a deformable porous medium is (Prevost, 2013; Tran et al., 2005):

$$\frac{\partial}{\partial t} (\phi^* \rho) - \nabla \cdot \left[\rho \frac{k}{\mu} \cdot (\nabla P - \rho b) \right] = Q_f \quad (\text{A20})$$

where b is the body force per unit mass of the fluid, k is the permeability, μ_f is the fluid viscosity, and Q_f is the fluid flow rate. The true porosity ($\phi = V_p / V_b$) has been replaced by the reservoir porosity ($\phi^* = (1 - \varepsilon_v) \phi$) in order to couple the rock deformation in the reservoir simulator (Coussy, 2004; Ebin, 2018; Settari & Mourits, 1998).

For a homogenous and isotropic material with a very small strain, the force equilibrium equation, the strain-displacement equation, and the constitutive stress-strain equation are (Cheng, 2016)

$$\nabla \cdot \sigma - F = 0 \quad (\text{A21})$$

$$\varepsilon = \frac{1}{2} \left[\nabla u + (\nabla u)^T \right] \quad (\text{A22})$$

$$\sigma = C : \varepsilon + \alpha P I \quad (\text{A23})$$

where σ represents the total stress tensor, F represents the body forces, ε is the strain tensor, u is the displacement vector, C is the tangential stiffness tensor, α is the Biot coefficient, and I is the identity matrix. Based on the above three equations, the final geomechanical balance equation is (Tran et al., 2009)

$$\nabla \left[C : \left(\frac{1}{2} \left(\nabla u + (\nabla u)^T \right) \right) \right] = -\nabla \alpha P I + \rho g \quad (\text{A24})$$

CMG applies the finite difference approach for solving fluid flow equations and the finite element method for solving the geomechanics equations (Computer Modeling Group Ltd., 2013). Figure A6 shows the workflow of the iterative two-way coupling method. The coupling between the fluid flow and geomechanics equations in CMG is achieved by the previously defined “reservoir porosity” (Ebin, 2018; Settari & Mourits, 1998). The conservation principle is satisfied by matching the porosity at the beginning of a time step with the porosity at the end of the previous time step (Tran et al., 2004, 2005).

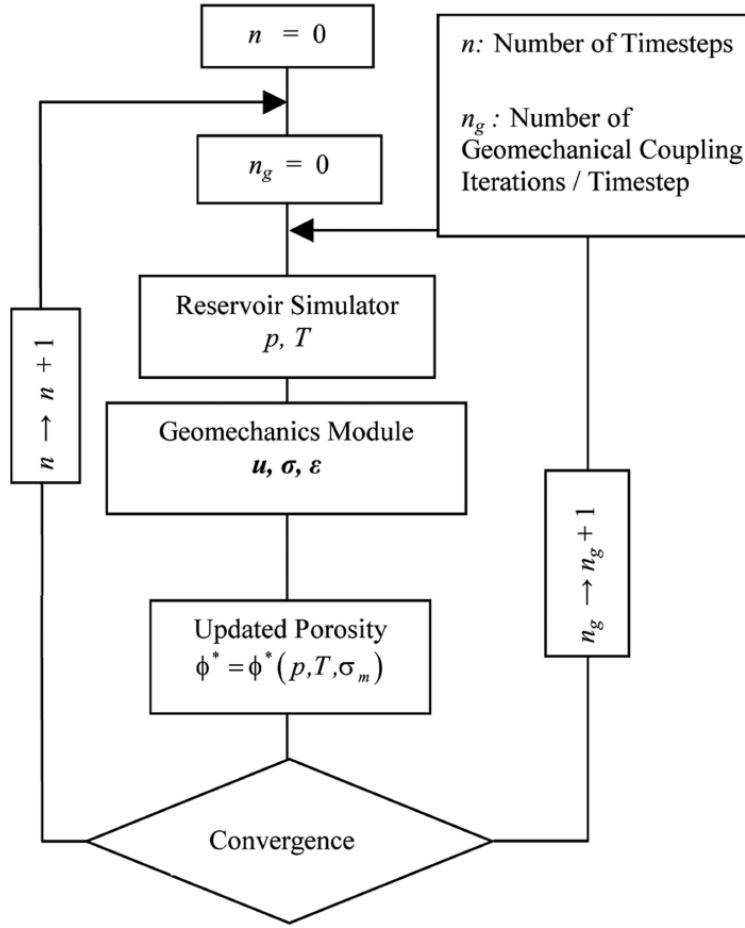


Figure A6: Flow chart for the iterative two-way coupling (Tran et al., 2004).

A8 SENSITIVITY TESTS ON GRID SIZE IN THE NUMERICAL SIMULATION

This appendix discusses the sensitivity of grid size on the numerical simulations in Chapter 5. The grid size is gradually reduced from the reservoir boundary to the center of the injection point. The grid size ($dx \times dy \times dz$) near the injector is $6\text{ m} \times 6\text{ m} \times 20\text{ m}$ with mesh refinement at the injection point. The sensitivity tests on the size of dz (in/around the injection zone) show that the small size of dz favors a slight increase of AIZ ΔP (Figure A7).

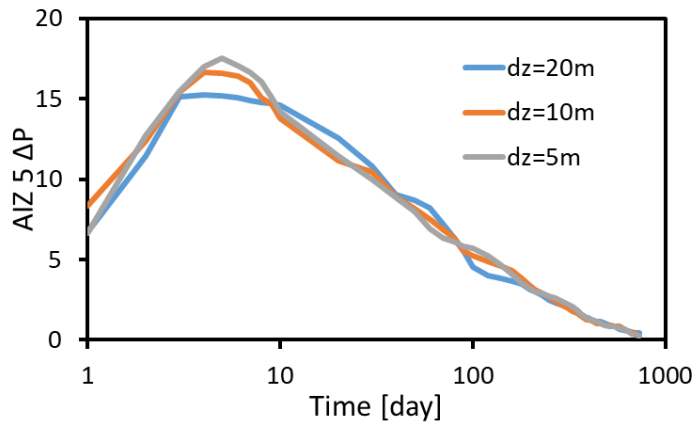


Figure A7: Sensitivity tests on grid size in the numerical simulation

A9 CAPILLARY PRESSURE AND RELATIVE PERMEABILITY

In the CMG model, the capillary pressure in sand is converted from J-functions measured with an air-mercury system to a CO₂-brine system and the relative permeability curve in sand is calculated through the Brooks-Corey drainage model (Jung et al., 2018) (Figures A8a and A8b). The capillary pressure and the relative permeability in shale are shown in Figures A8c and A8d (Bennion & Bachu, 2008; Ren et al., 2016).

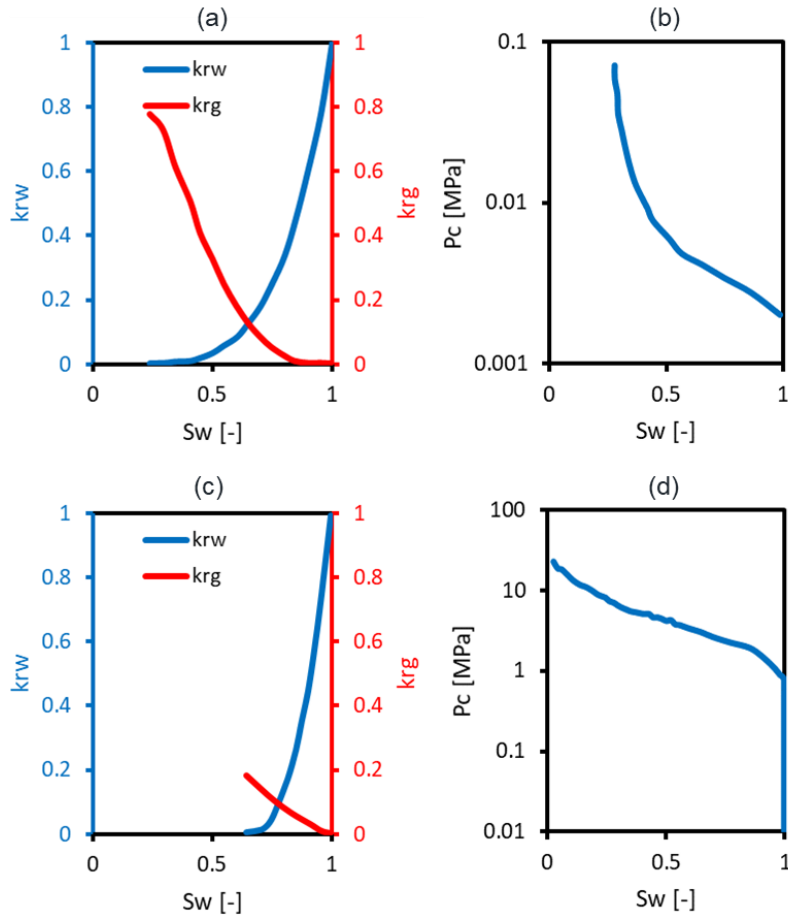


Figure A8: Capillary pressure and relative permeability in CMG: figures (a) and (b) are for sand; figures (c) and (d) are for shale.

The contribution of capillary pressure to effective stress can be estimated through the definition of Bishop effective stress (Bishop, 1959; N. Lu & Likos, 2006). The Bishop effective stress in unsaturated soil is usually written as follows:

$$\sigma^{eff} = \sigma - P_a + \chi(P_a - P_w) \quad (A25)$$

where P_a is the pore air pressure, P_w is the pore water pressure, and χ is the effective stress parameter. $\chi(P_a - P_w)$ describes the contribution of matric suction to effective stress due to capillary pressure, where χ varies between zero and unity as a function of pore water saturation. The capillary pressure between brine and CO₂ in the reservoir can be estimated

by the Young-Laplace equation and is usually in the order of a few kPa. The mean effective stress in the selected reservoir is ~3,000 psi (~20,684kPa). Thus, capillary pressure is negligible and does not significantly change the effective stress.

A10 AIZ PRESSURE MONITORING USING THE SGR-BASED AND THE PSSF-BASED FAULT PERMEABILITY

The fault in Chapter 5 is assumed to be homogeneous with a constant permeability. In this appendix, the results in Chapters 3 and 4 are integrated into the CO₂ storage model in Chapter 5; the fault permeability measured in Chapter 3 and the fault permeability predicted by the PSSF-based approach in Chapter 4 are populated into the fault in Chapter 5 to model the AIZ pressure variations due to partially undrained loading.

- (1) *Fault with the SGR-based permeability:* The experimental measurements on synthetic fault gouge in Chapter 3 give a quantitative relationship between clay fraction and fault gouge permeability. In this case, clay fraction is represented by shale gouge ratio (SGR), which is calculated by the SGR definition using the stratigraphic profile of sand-shale sequences (assuming fault throw is 50 m). Figure A9a shows the minimum fault permeability is ~10 nD in the caprock. Thus, the CO₂ plume cannot flow through the caprock into the overlying formations and the AIZ ΔP exhibits a similar trend with the base case (no fault) (Figure A9c).
- (2) *Fault with the PSSF-based permeability:* The random distribution of clay smears in faults after smear breach adds uncertainties to fault permeability as discussed in Chapter 4, particularly at a large fault throw (fault throw is 500 m in this case). The “gap” in this fault is located in the AIZ 5 and results in a leak (Figure A9b). However, the fault permeability in the caprock is ultra-low due to either clay smear

or shale juxtaposition. Thus, the AIZ ΔP exhibits a similar trend with the no-leak case (Figure A9c).

The presence of a sealing fault in both cases favors a stronger undrained loading above the reservoir and thus higher pressure increase in the AIZ than the base case with no leaks.

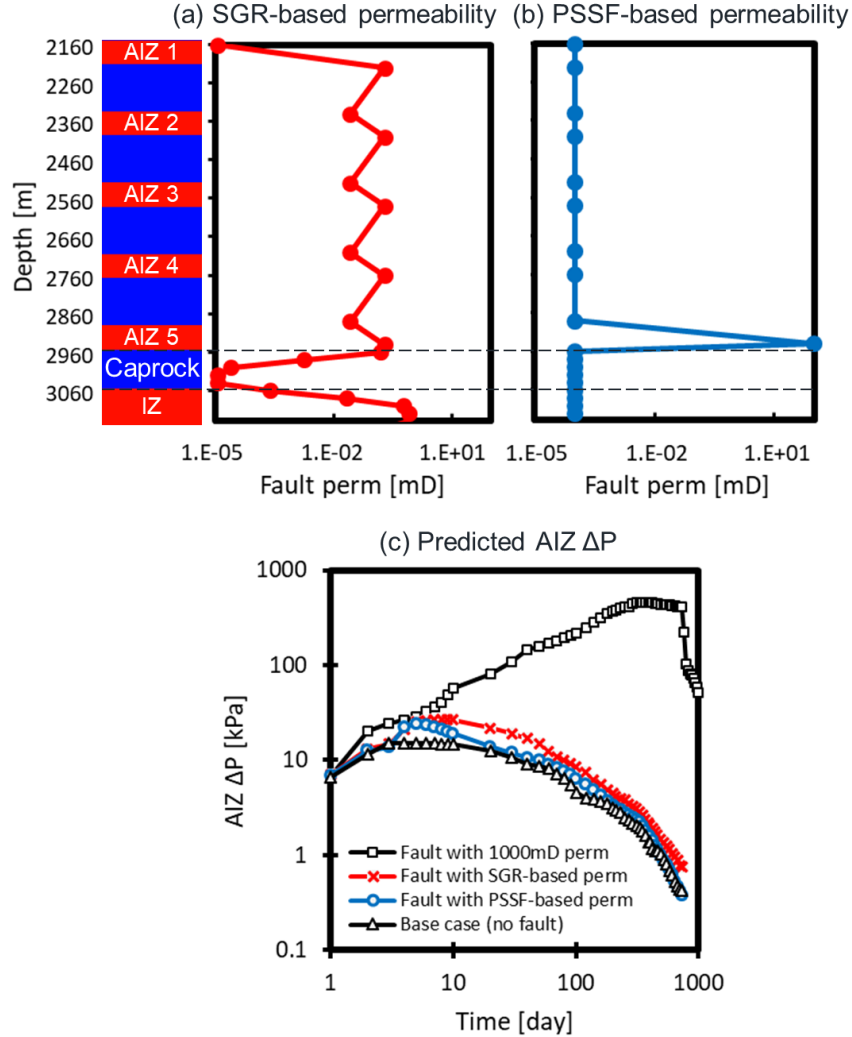


Figure A9: Impacts of different fault permeability on AIZ pressure changes: (a) SGR-based permeability predicted by experimental measurements on synthetic fault gouge; (b) PSSF-based permeability predicted by clay smear and shale juxtaposition sealing; (c) AIZ pressure increase in different cases.

Bibliography

- Ajo-Franklin, J. B., Peterson, J., Doetsch, J., & Daley, T. M. (2013). High-resolution characterization of a CO₂ plume using crosswell seismic tomography: Cranfield, MS, USA. *International Journal of Greenhouse Gas Control*, 18, 497–509.
<https://doi.org/10.1016/j.ijggc.2012.12.018>
- Allan, U. S. (1989). Model for Hydrocarbon Migration and Entrapment Within Faulted Structures. *AAPG Bulletin*, 73(7), 803–811.
- Amann-Hildenbrand, A., Bertier, P., Busch, A., & Krooss, B. M. (2013). Experimental investigation of the sealing capacity of generic clay-rich caprocks. *International Journal of Greenhouse Gas Control*, 19, 620–641.
<https://doi.org/10.1016/j.ijggc.2013.01.040>
- Andersen, M. A. (1988). Predicting Reservoir-Condition PV Compressibility From Hydrostatics Stress Laboratory Data. *SPE Reservoir Engineering*, 3(03), 1,078–1,082. <https://doi.org/10.2118/14213-PA>
- Anderson et al., M. A. (1985). A Comparison Of Hydrostatic-Stress And Uniaxial-Strain Pore-Volume Compressibilities Using Nonlinear Elastic Theory. Presented at the The 26th U.S. Symposium on Rock Mechanics (USRMS), American Rock Mechanics Association. Retrieved from <https://www.onepetro.org/conference-paper/ARMA-85-0403-1>
- Arif, M., Zhang, Y., & Iglauer, S. (2021). Shale Wettability: Data Sets, Challenges, and Outlook. *Energy & Fuels*, 35(4), 2965–2980.
<https://doi.org/10.1021/acs.energyfuels.0c04120>

- Arts, R., Eiken, O., Chadwick, A., Zweigel, P., van der Meer, L., & Zinszner, B. (2004). Monitoring of CO₂ injected at Sleipner using time-lapse seismic data. *Energy*, 29(9), 1383–1392. <https://doi.org/10.1016/j.energy.2004.03.072>
- Bachu, S. (2008). CO₂ storage in geological media: Role, means, status and barriers to deployment. *Progress in Energy and Combustion Science*, 34(2), 254–273. <https://doi.org/10.1016/j.pecs.2007.10.001>
- Bachu, Stefan. (2015). Review of CO₂ storage efficiency in deep saline aquifers. *International Journal of Greenhouse Gas Control*, 40, 188–202. <https://doi.org/10.1016/j.ijggc.2015.01.007>
- Bennion, B., & Bachu, S. (2008). Drainage and Imbibition Relative Permeability Relationships for Supercritical CO₂/Brine and H₂S/Brine Systems in Intergranular Sandstone, Carbonate, Shale, and Anhydrite Rocks. *SPE Reservoir Evaluation & Engineering*, 11(03), 487–496. <https://doi.org/10.2118/99326-PA>
- Bense, V. F., Gleeson, T., Loveless, S. E., Bour, O., & Scibek, J. (2013). Fault zone hydrogeology. *Earth-Science Reviews*, 127, 171–192. <https://doi.org/10.1016/j.earscirev.2013.09.008>
- Bishop, A. W. (1959). The Principle of Effective Stress. *Teknisk Ukeblad*, 39, 859–863.
- Bos, B., Peach, C. J., & Spiers, C. J. (2000). Frictional viscous flow of simulated fault gouge caused by the combined effects of phyllosilicates and pressure solution, 21.
- Boulin, P. F., Bretonnier, P., Vassil, V., Samouillet, A., Fleury, M., & Lombard, J. M. (2013). Sealing efficiency of caprocks: Experimental investigation of entry

- pressure measurement methods. *Marine and Petroleum Geology*, 48, 20–30.
<https://doi.org/10.1016/j.marpetgeo.2013.07.010>
- Bretan, P., Yielding, G., & Jones, H. (2003). Using calibrated shale gouge ratio to estimate hydrocarbon column heights. *AAPG Bulletin*, 87(3), 397–413.
<https://doi.org/10.1306/08010201128>
- Brown, A. R. (2011). *Interpretation of Three-Dimensional Seismic Data, Seventh edition*. Society of Exploration Geophysicists and American Association of Petroleum Geologists. <https://doi.org/10.1190/1.9781560802884>
- Busch, A., & Amann-Hildenbrand, A. (2013). Predicting capillarity of mudrocks. *Marine and Petroleum Geology*, 45, 208–223.
<https://doi.org/10.1016/j.marpetgeo.2013.05.005>
- Busch, A., Amann-Hildenbrand, A., Bertier, P., Waschbuesch, M., & Krooss, B. M. (2010). The Significance of Caprock Sealing Integrity for CO₂ Storage. In *SPE International Conference on CO₂ Capture, Storage, and Utilization*. New Orleans, Louisiana, USA: Society of Petroleum Engineers.
<https://doi.org/10.2118/139588-MS>
- Cai, J., Li, C., Song, K., Zou, S., Yang, Z., Shen, Y., et al. (2020). The influence of salinity and mineral components on spontaneous imbibition in tight sandstone. *Fuel*, 269, 117087. <https://doi.org/10.1016/j.fuel.2020.117087>
- Cappa. (2011). Modeling of coupled deformation and permeability evolution during fault reactivation induced by deep underground injection of CO₂. *International Journal*

- of Greenhouse Gas Control*, 5(2), 336–346.
<https://doi.org/10.1016/j.ijggc.2010.08.005>
- Cerveny, D., Dudley, F., Kaufman, K., & Krantz, E. G. (2005). Reducing Uncertainty with Fault-Seal Analysis. *Oilfield Review*, 14.
- Chaturvedi, K. R., Singh, A. K., & Sharma, T. (2019). Impact of shale on properties and oil recovery potential of sandstone formation for low-salinity waterflooding applications. *Asia-Pacific Journal of Chemical Engineering*, 14(5), e2352.
<https://doi.org/10.1002/apj.2352>
- Cheng, A. H.-D. (2016). *Poroelasticity*. Springer International Publishing.
<https://doi.org/10.1007/978-3-319-25202-5>
- Chertov et al., M. A. (2014). Practical Laboratory Methods for Pore Volume Compressibility Characterization in Different Rock Types. Presented at the 48th U.S. Rock Mechanics/Geomechanics Symposium, American Rock Mechanics Association. Retrieved from <https://www.onepetro.org/conference-paper/ARMA-2014-7532>
- Childs, C., Walsh, J. J., Manzocchi, T., Strand, J., Nicol, A., Tomasso, M., et al. (2007). Definition of a fault permeability predictor from outcrop studies of a faulted turbidite sequence, Taranaki, New Zealand. *Geological Society, London, Special Publications*, 292(1), 235–258. <https://doi.org/10.1144/SP292.14>
- Çiftçi, N. B., Giger, S. B., & Clennell, M. B. (2013). Three-dimensional structure of experimentally produced clay smears: Implications for fault seal analysis. *AAPG Bulletin*, 97(5), 733–757. <https://doi.org/10.1306/10161211192>

- Computer Modeling Group Ltd. (2013). Compositional & Unconventional Reservoir Simulation. Calgary.
- Coussy, O. (2004). *Poromechanics*. John Wiley & Sons.
- Cowie, P. A., Roberts, G. P., Bull, J. M., & Visini, F. (2012). Relationships between fault geometry, slip rate variability and earthquake recurrence in extensional settings. *Geophysical Journal International*, 189(1), 143–160.
<https://doi.org/10.1111/j.1365-246X.2012.05378.x>
- Crawford, B. R., Faulkner, D. R., & Rutter, E. H. (2008). Strength, porosity, and permeability development during hydrostatic and shear loading of synthetic quartz-clay fault gouge. *Journal of Geophysical Research: Solid Earth*, 113(B3).
<https://doi.org/10.1029/2006JB004634>
- Daigle, H., Ghanbarian, B., Henry, P., & Conin, M. (2015). Universal scaling of the formation factor in clays: Example from the Nankai Trough. *Journal of Geophysical Research: Solid Earth*, 120(11), 7361–7375.
<https://doi.org/10.1002/2015JB012262>
- Delle Piane, C., Giwelli, A., Clennell, M. B., Esteban, L., Nogueira Kiewiet, M. C. D., Kiewiet, L., et al. (2016). Frictional and hydraulic behaviour of carbonate fault gouge during fault reactivation — An experimental study. *Tectonophysics*, 690, 21–34. <https://doi.org/10.1016/j.tecto.2016.07.011>
- Detournay, E., & Cheng, A. H. D. (1993). Fundamentals of poroelasticity. *Unknown Journal*, 113–171. <https://doi.org/10.1016/b978-0-08-040615-2.50011-3>

- Detournay, E., & Cheng, A. H.-D. (1988). Poroelastic response of a borehole in a non-hydrostatic stress field. *International Journal of Rock Mechanics and Mining Sciences & Geomechanics Abstracts*, 25(3), 171–182.
[https://doi.org/10.1016/0148-9062\(88\)92299-1](https://doi.org/10.1016/0148-9062(88)92299-1)
- Dewhurst, D. N., Jones, R. M., & Raven, M. D. (2002). Microstructural and petrophysical characterization of Muderong Shale: application to top seal risking. *Petroleum Geoscience*, 8(4), 371–383. <https://doi.org/10.1144/petgeo.8.4.371>
- Doughty, Freifeld, B. M., & Trautz, R. C. (2008). Site characterization for CO₂ geologic storage and vice versa: the Frio brine pilot, Texas, USA as a case study. *Environmental Geology*, 54(8), 1635–1656. <https://doi.org/10.1007/s00254-007-0942-0>
- Doughty, T. (2003). Clay smear seals and fault sealing potential of an exhumed growth fault, Rio Grande rift, New Mexico. *AAPG Bulletin*, 87(3), 427–444.
<https://doi.org/10.1306/10010201130>
- Draganits, E., Grasemann, B., & Hager, C. (2005). Conjugate, cataclastic deformation bands in the Lower Devonian Muth Formation (Tethyan Zone, NW India): evidence for pre-Himalayan deformation structures. *Geological Magazine*, 142(06), 765. <https://doi.org/10.1017/S0016756805001056>
- Duan, Q., Chen, J., & Yang, X. (2020). A Comparison of Gas and Water Permeability in Clay-Bearing Fault and Reservoir Rocks: Experimental Results and Evolution Mechanisms. *Journal of Geophysical Research: Solid Earth*, 125(7), e2019JB018278. <https://doi.org/10.1029/2019JB018278>

- Dudley, J. W., Brignoli, M., Crawford, B. R., Ewy, R. T., Love, D. K., McLennan, J. D., et al. (2016). ISRM Suggested Method for Uniaxial-Strain Compressibility Testing for Reservoir Geomechanics. *Rock Mechanics and Rock Engineering*, 49(10), 4153–4178. <https://doi.org/10.1007/s00603-016-1055-4>
- Ebin, J. P. (2018, August 16). *Coupled Fluid Flow and Geomechanical Modeling of Induced Seismicity* (Thesis). Retrieved from <https://oaktrust.library.tamu.edu/handle/1969.1/174296>
- Ehlig-Economides et al. (2010). Sequestering carbon dioxide in a closed underground volume. *Journal of Petroleum Science and Engineering*, 70(1), 123–130. <https://doi.org/10.1016/j.petrol.2009.11.002>
- Eiken, O., Ringrose, P., Hermanrud, C., Nazarian, B., Torp, T. A., & Høier, L. (2011). Lessons learned from 14 years of CCS operations: Sleipner, In Salah and Snøhvit. *Energy Procedia*, 4, 5541–5548. <https://doi.org/10.1016/j.egypro.2011.02.541>
- Emberley, S., Hutcheon, I., Shevalier, M., Durocher, K., Gunter, W. D., & Perkins, E. H. (2004). Geochemical monitoring of fluid-rock interaction and CO₂ storage at the Weyburn CO₂-injection enhanced oil recovery site, Saskatchewan, Canada. *Energy*, 29(9–10), 1393–1401. <https://doi.org/10.1016/j.energy.2004.03.073>
- Ennis-King, J., LaForce, T., Paterson, L., Dance, T., Jenkins, C., & Cinar, Y. (2017). Interpretation of Above Zone and Storage Zone Pressure Responses to Carbon Dioxide Injection in the 2016 CO₂CRC Field Test. *Energy Procedia*, 114, 5671–5679. <https://doi.org/10.1016/j.egypro.2017.03.1706>

- Espinoza, D. N. (2017). CO₂ breakthrough—Caprock sealing efficiency and integrity for carbon geological storage. *International Journal of Greenhouse Gas Control*, 66, 218–229. <https://doi.org/10.1016/j.ijggc.2017.09.019>
- Espinoza, D. N., & Santamarina, J. C. (2010). Water-CO₂-mineral systems: Interfacial tension, contact angle, and diffusion—Implications to CO₂ geological storage. *Water Resources Research*, 46(7). <https://doi.org/10.1029/2009WR008634>
- Exner, U., Kaiser, J., & Gier, S. (2013). Deformation bands evolving from dilation to cementation bands in a hydrocarbon reservoir (Vienna Basin, Austria). *Marine and Petroleum Geology*, 43, 504–515.
<https://doi.org/10.1016/j.marpetgeo.2012.10.001>
- Faerseth, R. B. (2006). Shale smear along large faults: continuity of smear and the fault seal capacity. *Journal of the Geological Society*, 163(5), 741–751.
<https://doi.org/10.1144/0016-76492005-162>
- Falcon-Suarez, I. H., Livo, K., Callow, B., Marin-Moreno, H., Prasad, M., & Best, A. I. (2020). Geophysical early warning of salt precipitation during geological carbon sequestration. *Scientific Reports*, 10(1), 16472. <https://doi.org/10.1038/s41598-020-73091-3>
- Faulkner, D. R., & Rutter, E. H. (2000). Comparisons of water and argon permeability in natural clay-bearing fault gouge under high pressure at 20°C. *Journal of Geophysical Research: Solid Earth*, 105(B7), 16415–16426.
<https://doi.org/10.1029/2000JB900134>

- Faulkner, D. R., Jackson, C. A. L., Lunn, R. J., Schlische, R. W., Shipton, Z. K., Wibberley, C. A. J., & Withjack, M. O. (2010). A review of recent developments concerning the structure, mechanics and fluid flow properties of fault zones. *Journal of Structural Geology*, 32(11), 1557–1575.
<https://doi.org/10.1016/j.jsg.2010.06.009>
- Fjar, E., Holt, R. M., Raaen, A. M., Risnes, R., & Horsrud, P. (2008). *Petroleum Related Rock Mechanics*. Elsevier.
- Fowler, J., Houston, J., Mitchell, D., & Slater, J. A. (1987). High Island Block 24-L Field, 291–294.
- Freeman, S. R., Harris, S. D., & Knipe, R. J. (2010). Cross-fault sealing, baffling and fluid flow in 3D geological models: tools for analysis, visualization and interpretation. *Geological Society, London, Special Publications*, 347(1), 257–282. <https://doi.org/10.1144/SP347.15>
- Fristad, T., Groth, A., Yielding, G., & Freeman, B. (1997). Quantitative fault seal prediction: a case study from Oseberg Syd, 18.
- Fulljames, J. R., Zijerveld, L. J. J., & Franssen, R. C. M. W. (1997). Fault seal processes: systematic analysis of fault seals over geological and production time scales. In *Norwegian Petroleum Society Special Publications* (Vol. 7, pp. 51–59). Elsevier.
[https://doi.org/10.1016/S0928-8937\(97\)80006-9](https://doi.org/10.1016/S0928-8937(97)80006-9)
- Gallé, C. (2001). Effect of drying on cement-based materials pore structure as identified by mercury intrusion porosimetry: A comparative study between oven-, vacuum-,

- and freeze-drying. *Cement and Concrete Research*, 31(10), 1467–1477.
[https://doi.org/10.1016/S0008-8846\(01\)00594-4](https://doi.org/10.1016/S0008-8846(01)00594-4)
- Gallé, C., & Tanai, K. (1998). Evaluation of Gas Transport Properties of Backfill Materials for Waste Disposal: H₂ Migration Experiments in Compacted Fo-Ca Clay. *Clays and Clay Minerals*, 46(5), 498–508.
<https://doi.org/10.1346/CCMN.1998.0460503>
- Gao, S., Wei, N., Li, X., Wang, Y., & Wang, Q. (2014). Cap Rock CO₂ Breakthrough Pressure Measurement Apparatus and Application in Shenhua CCS Project. *Energy Procedia*, 63, 4766–4772. <https://doi.org/10.1016/j.egypro.2014.11.507>
- Germaine, J. T., & Germaine, A. V. (2009). *Geotechnical Laboratory Measurements for Engineers*. John Wiley & Sons.
- Gholami, R., Rasouli, V., Sarmadivaleh, M., Minaeian, V., & Fakhari, N. (2016). Brittleness of gas shale reservoirs: A case study from the north Perth basin, Australia. *Journal of Natural Gas Science and Engineering*, 33, 1244–1259.
<https://doi.org/10.1016/j.jngse.2016.03.013>
- Grude, S., Landrø, M., & Osdal, B. (2013). Time-lapse pressure–saturation discrimination for CO₂ storage at the Snøhvit field. *International Journal of Greenhouse Gas Control*, 19, 369–378.
<https://doi.org/10.1016/j.ijggc.2013.09.014>
- Guglielmi, Y., Cappa, F., Avouac, J.-P., Henry, P., & Elsworth, D. (2015). Seismicity triggered by fluid injection-induced aseismic slip. *Science*, 348(6240), 1224–1226. <https://doi.org/10.1126/science.aab0476>

Guiltinan, E. J., Espinoza, D. N., Cockrell, L. P., & Cardenas, M. B. (2018). Textural and compositional controls on mudrock breakthrough pressure and permeability.

Advances in Water Resources, 121, 162–172.

<https://doi.org/10.1016/j.advwatres.2018.08.014>

Gutjahr, A. L., Gelhar, L. W., Bakr, A. A., & MacMillan, J. R. (1978). Stochastic analysis of spatial variability in subsurface flows: 2. Evaluation and application.

Water Resources Research, 14(5), 953–959.

<https://doi.org/10.1029/WR014i005p00953>

Hansen, O., Gilding, D., Nazarian, B., Osdal, B., Ringrose, P., Kristoffersen, J.-B., et al. (2013). Snøhvit: The History of Injecting and Storing 1 Mt CO₂ in the Fluvial

Tubåen Fm. *Energy Procedia*, 37, 3565–3573.

<https://doi.org/10.1016/j.egypro.2013.06.249>

Hildenbrand, A., Schlömer, S., & Krooss, B. M. (2002). Gas breakthrough experiments on fine-grained sedimentary rocks. *Geofluids*, 2(1), 3–23.

<https://doi.org/10.1046/j.1468-8123.2002.00031.x>

Horseman et al. (1999). Gas migration in clay barriers - ScienceDirect. Retrieved August 13, 2019, from

<https://www.sciencedirect.com/science/article/pii/S0013795299000691>

Hosseini, S., & Alfi, M. (2016). Time-lapse application of pressure transient analysis for monitoring compressible fluid leakage. *Greenhouse Gases: Science and Technology*, 6(3), 352–369. <https://doi.org/10.1002/ghg.1570>

Hosseini, S., Shakiba, M., Sun, A., & Hovorka, S. D. (2018). In-Zone and Above-Zone Pressure Monitoring Methods for CO₂ Geologic Storage.

<https://doi.org/10.1002/9781119118657.CH11>

Hovorka, Benson, S. M., Doughty, C., Freifeld, B. M., Sakurai, S., Daley, T. M., et al. (2006a). Measuring permanence of CO₂ storage in saline formations: the Frio experiment. *Environmental Geosciences*, 13(2), 105–121.

<https://doi.org/10.1306/eg.11210505011>

Hovorka, S. D., Doughty, C., Benson, S. M., Pruess, K., & Knox, P. R. (2004). The impact of geological heterogeneity on CO₂ storage in brine formations: a case study from the Texas Gulf Coast. *Geological Society, London, Special Publications*, 233(1), 147–163. <https://doi.org/10.1144/GSL.SP.2004.233.01.10>

Hovorka, S. D., Benson, S. M., Doughty, C., Freifeld, B. M., Sakurai, S., Daley, T. M., et al. (2006b). Measuring permanence of CO₂ storage in saline formations: the Frio experiment. *Environmental Geosciences*, 13(2), 105–121.

<https://doi.org/10.1306/eg.11210505011>

Ikari, M. J., Saffer, D. M., & Marone, C. (2009). Frictional and hydrologic properties of clay-rich fault gouge. *Journal of Geophysical Research: Solid Earth*, 114(B5). <https://doi.org/10.1029/2008JB006089>

Jaeger, J. C., Cook, N. G. W., & Zimmerman, R. (2009). *Fundamentals of Rock Mechanics*. John Wiley & Sons.

Johansen, T. E. S., Fossen, H., & Kluge, R. (2005). The impact of syn-faulting porosity reduction on damage zone architecture in porous sandstone: an outcrop example

- from the Moab Fault, Utah. *Journal of Structural Geology*, 27(8), 1469–1485.
<https://doi.org/10.1016/j.jsg.2005.01.014>
- de Jong, S. M., Spiers, C. J., & Busch, A. (2014). Development of swelling strain in smectite clays through exposure to carbon dioxide. *International Journal of Greenhouse Gas Control*, 24, 149–161.
<https://doi.org/10.1016/j.ijggc.2014.03.010>
- Jung, H., Singh, G., Nicolas Espinoza, D., & Wheeler, M. F. (2017). An Integrated Case Study of the Frio CO₂ Sequestration Pilot Test for Safe and Effective Carbon Storage Including Compositional Flow and Geomechanics. Society of Petroleum Engineers. <https://doi.org/10.2118/182710-MS>
- Jung, H., Singh, G., Espinoza, D. N., & Wheeler, M. F. (2018). Quantification of a maximum injection volume of CO₂ to avert geomechanical perturbations using a compositional fluid flow reservoir simulator. *Advances in Water Resources*, 112, 160–169. <https://doi.org/10.1016/j.advwatres.2017.12.003>
- Kashefi, K., Pereira, L. M. C., Chapoy, A., Burgass, R., & Tohidi, B. (2016). Measurement and modelling of interfacial tension in methane/water and methane/brine systems at reservoir conditions. *Fluid Phase Equilibria*, 409, 301–311. <https://doi.org/10.1016/j.fluid.2015.09.050>
- Katz, A. J., & Thompson, A. H. (1987). Prediction of rock electrical conductivity from mercury injection measurements. *Journal of Geophysical Research: Solid Earth*, 92(B1), 599–607. <https://doi.org/10.1029/JB092iB01p00599>

- Kettermann, M., Urai, J. L., & Vrolijk, P. J. (2017). Evolution of structure and permeability of normal faults with clay smear: Insights from water-saturated sandbox models and numerical simulations. *Journal of Geophysical Research: Solid Earth*, 122(3), 1697–1725. <https://doi.org/10.1002/2016JB013341>
- Kharaka, Cole, D. R., Hovorka, S. D., Gunter, W. D., Knauss, K. G., & Freifeld, B. M. (2006). Gas-water-rock interactions in Frio Formation following CO₂ injection: Implications for the storage of greenhouse gases in sedimentary basins, 4.
- Kharaka, Thordsen, J. J., Hovorka, S. D., Seay Nance, H., Cole, D. R., Phelps, T. J., & Knauss, K. G. (2009a). Potential environmental issues of CO₂ storage in deep saline aquifers: Geochemical results from the Frio-I Brine Pilot test, Texas, USA. *Applied Geochemistry*, 24(6), 1106–1112.
<https://doi.org/10.1016/j.apgeochem.2009.02.010>
- Kharaka, Y. K., Thordsen, J. J., Hovorka, S. D., Seay Nance, H., Cole, D. R., Phelps, T. J., & Knauss, K. G. (2009b). Potential environmental issues of CO₂ storage in deep saline aquifers: Geochemical results from the Frio-I Brine Pilot test, Texas, USA. *Applied Geochemistry*, 24(6), 1106–1112.
<https://doi.org/10.1016/j.apgeochem.2009.02.010>
- Kim, S., & Hosseini, S. A. (2014). Above-zone pressure monitoring and geomechanical analyses for a field-scale CO₂ injection project in Cranfield, MS. *Greenhouse Gases: Science and Technology*, 4(1), 81–98. <https://doi.org/10.1002/ghg.1388>

- Kim, S., & Hosseini, S. A. (2015). Hydro-thermo-mechanical analysis during injection of cold fluid into a geologic formation. *International Journal of Rock Mechanics and Mining Sciences*, 77, 220–236. <https://doi.org/10.1016/j.ijrmms.2015.04.010>
- Kumar, R., Campbell, S., Sonnenthal, E., & Cunningham, J. (2020). Effect of brine salinity on the geological sequestration of CO₂ in a deep saline carbonate formation. *Greenhouse Gases: Science and Technology*, 10(2), 296–312. <https://doi.org/10.1002/ghg.1960>
- Kvamme, B., Kuznetsova, T., Hebach, A., Oberhof, A., & Lunde, E. (2007). Measurements and modelling of interfacial tension for water+carbon dioxide systems at elevated pressures. *Computational Materials Science*, 38(3), 506–513. <https://doi.org/10.1016/j.commatsci.2006.01.020>
- Laubach, S. E., Lander, R. H., Criscenti, L. J., Anovitz, L. M., Urai, J. L., Pollyea, R. M., et al. (2019). The Role of Chemistry in Fracture Pattern Development and Opportunities to Advance Interpretations of Geological Materials. *Reviews of Geophysics*, 57(3), 1065–1111. <https://doi.org/10.1029/2019RG000671>
- Laubach, Stephen E. (2003). Practical approaches to identifying sealed and open fractures. *AAPG Bulletin*, 87(4), 561–579. <https://doi.org/10.1306/11060201106>
- Lehner, F. K., & Pilaar, W. F. (1997). The emplacement of clay smears in synsedimentary normal faults: inferences from field observations near Frechen, Germany. In *Norwegian Petroleum Society Special Publications* (Vol. 7, pp. 39–50). Elsevier. [https://doi.org/10.1016/S0928-8937\(97\)80005-7](https://doi.org/10.1016/S0928-8937(97)80005-7)

Lewicki, J. L., Birkholzer, J., & Tsang, C.-F. (2006). Natural and industrial analogues for leakage of CO₂ from storage reservoirs: identification of features, events, and processes and lessons learned. *Environmental Geology*, 52(3), 457.

<https://doi.org/10.1007/s00254-006-0479-7>

Li et al. (2006). Permeability Variations Associated With Shearing and Isotropic Unloading During the SAGD Process. *Journal of Canadian Petroleum Technology*, 45(01). <https://doi.org/10.2118/06-01-05>

Li, S., Dong, M., Li, Z., Huang, S., Qing, H., & Nickel, E. (2005). Gas breakthrough pressure for hydrocarbon reservoir seal rocks: implications for the security of long-term CO₂ storage in the Weyburn field. *Geofluids*, 5(4), 326–334.

<https://doi.org/10.1111/j.1468-8123.2005.00125.x>

Liebscher, A., Möller, F., Bannach, A., Köhler, S., Wiebach, J., Schmidt-Hattenberger, C., et al. (2013). Injection operation and operational pressure–temperature monitoring at the CO₂ storage pilot site Ketzin, Germany—Design, results, recommendations. *International Journal of Greenhouse Gas Control*, 15, 163–173. <https://doi.org/10.1016/j.ijggc.2013.02.019>

Lindsay, N. G., Murphy, F. C., Walsh, J. J., & Watterson, J. (2009). Outcrop Studies of Shale Smears on Fault Surface. In *The Geological Modelling of Hydrocarbon Reservoirs and Outcrop Analogues* (pp. 113–123). Wiley-Blackwell.

<https://doi.org/10.1002/9781444303957.ch6>

- Lu, J., Larson, T. E., & Smyth, R. C. (2015). Carbon isotope effects of methane transport through Anahuac Shale — A core gas study. *Journal of Geochemical Exploration*, 148, 138–149. <https://doi.org/10.1016/j.gexplo.2014.09.005>
- Lu, N., & Likos, W. J. (2006). Suction Stress Characteristic Curve for Unsaturated Soil. *Journal of Geotechnical and Geoenvironmental Engineering*, 132(2), 131–142. [https://doi.org/10.1061/\(ASCE\)1090-0241\(2006\)132:2\(131\)](https://doi.org/10.1061/(ASCE)1090-0241(2006)132:2(131))
- Luquot, L., & Gouze, P. (2009). Experimental determination of porosity and permeability changes induced by injection of CO₂ into carbonate rocks. *Chemical Geology*, 265(1), 148–159. <https://doi.org/10.1016/j.chemgeo.2009.03.028>
- Makhnenko, R. Y., Vilarrasa, V., Mylnikov, D., & Laloui, L. (2017). Hydromechanical Aspects of CO₂ Breakthrough into Clay-rich Caprock. *Energy Procedia*, 114, 3219–3228. <https://doi.org/10.1016/j.egypro.2017.03.1453>
- Mathias, S. A., González Martínez de Miguel, G. J., Thatcher, K. E., & Zimmerman, R. W. (2011). Pressure Buildup During CO₂ Injection into a Closed Brine Aquifer. *Transport in Porous Media*, 89(3), 383–397. <https://doi.org/10.1007/s11242-011-9776-z>
- McKie, T., Jolley, S. J., & Kristensen, M. B. (2010). Stratigraphic and structural compartmentalization of dryland fluvial reservoirs: Triassic Heron Cluster, Central North Sea. *Geological Society, London, Special Publications*, 347(1), 165–198. <https://doi.org/10.1144/SP347.11>

Meckel, T., Hovorka, S., & Kalyanaraman, N. (2008). Continuous pressure monitoring for large volume CO₂ injections. *Presented at the 9th International Conference on Greenhouse Gas Control Technologies (GHGT-9)*.

Meckel, T. A., Trevino, R., & Hovorka, S. D. (2017). Offshore CO₂ Storage Resource Assessment of the Northern Gulf of Mexico. *Energy Procedia*, 114, 4728–4734.

<https://doi.org/10.1016/j.egypro.2017.03.1609>

Milliken, K. L. (2019). Compactional and mass-balance constraints inferred from the volume of quartz cementation in mudrocks, in W. Camp. In *Mudstone diagenesis: Research perspectives for shale hydrocarbon reservoirs, seals, and source rocks: AAPG Memoir 120* (pp. 33–48).

Mishra, S., Oruganti, Y. D., Gupta, N., Ganesh, P. R., McNeil, C., Bhattacharya, I., & Spitznogle, G. (2014). Modeling CO₂ plume migration based on calibration of injection and post-injection pressure response at the AEP Mountaineer Project. *Greenhouse Gases: Science and Technology*, 4(3), 331–356.

<https://doi.org/10.1002/ghg.1434>

Newman, G. H. (1973). Pore-Volume Compressibility of Consolidated, Friable, and Unconsolidated Reservoir Rocks Under Hydrostatic Loading. *Journal of Petroleum Technology*, 25(02), 129–134. <https://doi.org/10.2118/3835-PA>

Nicot, J.-P. (2008). Evaluation of large-scale CO₂ storage on fresh-water sections of aquifers: An example from the Texas Gulf Coast Basin. *International Journal of Greenhouse Gas Control*, 2(4), 582–593.

<https://doi.org/10.1016/j.ijggc.2008.03.004>

Noorsalehi-Garakani, Kleine Vennekate, G. J., Vrolijk, P., & Urai, J. L. (2013). Clay-smear continuity and normal fault zone geometry – First results from excavated sandbox models. *Journal of Structural Geology*, 57, 58–80.

<https://doi.org/10.1016/j.jsg.2013.09.008>

Noorsalehi-Garakani, Urai, J., Ziegler, M., & Walsh, J. J. (2015). *Fault gouge in sand-clay sequences - a first look in 3D*. Aachen.

Ong, S., Zheng, Z., & Chhajlani, R. (2001). Pressure-Dependent Pore Volume Compressibility - A Cost Effective Log-Based Approach. Presented at the SPE Asia Pacific Improved Oil Recovery Conference, Society of Petroleum Engineers.
<https://doi.org/10.2118/72116-MS>

Otsuki, K., Monzawa, N., & Nagase, T. (2003). Fluidization and melting of fault gouge during seismic slip: Identification in the Nojima fault zone and implications for focal earthquake mechanisms. *Journal of Geophysical Research: Solid Earth*, 108(B4). <https://doi.org/10.1029/2001JB001711>

Park, Y.-C., Huh, D.-G., & Park, C.-H. (2012). A pressure-monitoring method to warn CO₂ leakage in geological storage sites. *Environmental Earth Sciences*, 67.
<https://doi.org/10.1007/s12665-012-1667-2>

Peters, E. J. (2012). *Advanced Petrophysics: Geology, porosity, absolute permeability, heterogeneity, and geostatistics*. Greenleaf Book Group.

Phillips, T., Kampman, N., Bisdom, K., Forbes Inskip, N. D., den Hartog, S. A. M., Cnudde, V., & Busch, A. (2020). Controls on the intrinsic flow properties of

- mudrock fractures: A review of their importance in subsurface storage. *Earth-Science Reviews*, 211, 103390. <https://doi.org/10.1016/j.earscirev.2020.103390>
- Plona et al., T. J. (1995). Effects of stress cycles on static and dynamic Young's moduli in Castlegate sandstone. Presented at the The 35th U.S. Symposium on Rock Mechanics (USRMS), American Rock Mechanics Association. Retrieved from <https://www.onepetro.org/conference-paper/ARMA-95-0155>
- Prevost, J. H. (2013). One-Way versus Two-Way Coupling in Reservoir-Geomechanical Models, 517–526. <https://doi.org/10.1061/9780784412992.061>
- Ramos, M. J., Nicolas Espinoza, D., Torres-Verdín, C., & Grover, T. (2017). Use of S-wave anisotropy to quantify the onset of stress-induced microfracturing. *GEOPHYSICS*, 82(6), MR201–MR212. <https://doi.org/10.1190/geo2016-0579.1>
- Ren, W., Li, G., Tian, S., Sheng, M., Yang, R., & Wang, T. (2016). Comparison of Capillary Pressure-Saturation Models for Gas-Water Systems in Shale Gas Reservoirs. Presented at the SPE Asia Pacific Oil & Gas Conference and Exhibition, OnePetro. <https://doi.org/10.2118/182461-MS>
- Rohmer, J., Pluymakers, A., & Renard, F. (2016). Mechano-chemical interactions in sedimentary rocks in the context of CO₂ storage: Weak acid, weak effects? *Earth-Science Reviews*, 157, 86–110. <https://doi.org/10.1016/j.earscirev.2016.03.009>
- Roussel, N. P., & Agrawal, S. (2017). Introduction to Poroelastic Response Monitoring - Quantifying Hydraulic Fracture Geometry and SRV Permeability from Offset-Well Pressure Data. Presented at the SPE/AAPG/SEG Unconventional Resources

- Technology Conference, Unconventional Resources Technology Conference.
<https://doi.org/10.15530/URTEC-2017-2645414>
- Ruiz, I. (2019, July 25). *Characterization of the High Island 24L Field for modeling and estimating CO₂ storage capacity in the offshore Texas state waters, Gulf of Mexico* (Thesis). <https://doi.org/10.26153/tsw/5440>
- Rutqvist. (2016). Fault activation and induced seismicity in geological carbon storage – Lessons learned from recent modeling studies. *Journal of Rock Mechanics and Geotechnical Engineering*, 8(6), 789–804.
<https://doi.org/10.1016/j.jrmge.2016.09.001>
- Rutqvist, Vasco, D. W., & Myer, L. (2009). Coupled reservoir-geomechanical analysis of CO₂ injection at In Salah, Algeria. *Energy Procedia*, 1(1), 1847–1854.
<https://doi.org/10.1016/j.egypro.2009.01.241>
- Rutqvist, J., Birkholzer, J., Cappa, F., & Tsang, C.-F. (2007). Estimating maximum sustainable injection pressure during geological sequestration of CO₂ using coupled fluid flow and geomechanical fault-slip analysis. *Energy Conversion and Management*, 48(6), 1798–1807. <https://doi.org/10.1016/j.enconman.2007.01.021>
- Rutqvist, Jonny, Vasco, D. W., & Myer, L. (2010). Coupled reservoir-geomechanical analysis of CO₂ injection and ground deformations at In Salah, Algeria. *International Journal of Greenhouse Gas Control*, 4(2), 225–230.
<https://doi.org/10.1016/j.ijggc.2009.10.017>

- Rutter, E. H., & Maddock, R. H. (1992). On the mechanical properties of synthetic kaolinite/quartz fault gouge. *Terra Nova*, 4(4), 489–500.
<https://doi.org/10.1111/j.1365-3121.1992.tb00585.x>
- Rutter, E. H., Maddock, R. H., Hall, S. H., & White, S. H. (1986). Comparative microstructures of natural and experimentally produced clay-bearing fault gouges. *Pure and Applied Geophysics PAGEOPH*, 124(1–2), 3–30.
<https://doi.org/10.1007/BF00875717>
- Santamarina, J. C., Klein, A., & Fam, M. A. (2001). Soils and waves: Particulate materials behavior, characterization and process monitoring. *Journal of Soils and Sediments*, 1(2), 130–130. <https://doi.org/10.1007/BF02987719>
- Sawabini', C. T., Chilingar, G. V., & Aime, S. (1974). Compressibility of Unconsolidated, Arkosic Oil Sands, 7.
- Schlömer, S., & Krooss, B. M. (1997). Experimental characterisation of the hydrocarbon sealing efficiency of cap rocks. *Marine and Petroleum Geology*, 14(5), 565–580.
[https://doi.org/10.1016/S0264-8172\(97\)00022-6](https://doi.org/10.1016/S0264-8172(97)00022-6)
- Schmatz, & Urai, J. (2006). *Experimental study on clay gouge evolution in mechanically stratified sequences* (PhD Thesis). Hochschulbibliothek der Rheinisch-Westfälischen Technischen Hochschule Aachen.
- Schmatz, Holland, M., Giese, S., van der Zee, W., & Urai, Janos. L. (2010). Clay smear processes in mechanically layered sequences — Results of water-saturated model experiments with free top surface. *Journal of the Geological Society of India*, 75(1), 74–88. <https://doi.org/10.1007/s12594-010-0025-9>

- Schneider, J., Flemings, P. B., Day-Stirrat, R. J., & Germaine, J. T. (2011). Insights into pore-scale controls on mudstone permeability through resedimentation experiments. *Geology*, 39(11), 1011–1014. <https://doi.org/10.1130/G32475.1>
- Schowalter, T. T. (1979). Mechanics of Secondary Hydrocarbon Migration and Entrapment. *AAPG Bulletin*, 63(5), 723–760. <https://doi.org/10.1306/2F9182CA-16CE-11D7-8645000102C1865D>
- Segall, & Fitzgerald. (1998). A note on induced stress changes in hydrocarbon and geothermal reservoirs. *Tectonophysics*, 289(1–3), 117–128. [https://doi.org/10.1016/S0040-1951\(97\)00311-9](https://doi.org/10.1016/S0040-1951(97)00311-9)
- Settari, A., & Mourits, F. M. (1998). A Coupled Reservoir and Geomechanical Simulation System. *SPE Journal*, 3(03), 219–226. <https://doi.org/10.2118/50939-PA>
- Shi, Durucan, S., & Fujioka, M. (2008). A reservoir simulation study of CO₂ injection and N₂ flooding at the Ishikari coalfield CO₂ storage pilot project, Japan. *International Journal of Greenhouse Gas Control*, 2(1), 47–57. [https://doi.org/10.1016/S1750-5836\(07\)00112-0](https://doi.org/10.1016/S1750-5836(07)00112-0)
- Shi, J.-Q., Imrie, C., Sinayuc, C., Durucan, S., Korre, A., & Eiken, O. (2013). Snøhvit CO₂ Storage Project: Assessment of CO₂ Injection Performance Through History Matching of the Injection Well Pressure Over a 32-months Period. *Energy Procedia*, 37, 3267–3274. <https://doi.org/10.1016/j.egypro.2013.06.214>

- Shin, H., & Santamarina, J. c. (2011). Desiccation cracks in saturated fine-grained soils: particle-level phenomena and effective-stress analysis. *Géotechnique*, 61(11), 961–972. <https://doi.org/10.1680/geot.8.P.012>
- Sperrevik, S., Gillespie, P. A., Fisher, Q. J., Halvorsen, T., & Knipe, R. J. (2002). Empirical estimation of fault rock properties. In *Norwegian Petroleum Society Special Publications* (Vol. 11, pp. 109–125). Elsevier.
[https://doi.org/10.1016/S0928-8937\(02\)80010-8](https://doi.org/10.1016/S0928-8937(02)80010-8)
- Stork, A. L., Verdon, J. P., & Kendall, J.-M. (2015). The microseismic response at the In Salah Carbon Capture and Storage (CCS) site. *International Journal of Greenhouse Gas Control*, 32, 159–171.
<https://doi.org/10.1016/j.ijggc.2014.11.014>
- Sun, Z., Tang, H., Espinoza, D. N., Balhoff, M. T., & Killough, J. E. (2018). Pore-to Reservoir-Scale Modeling of Depletion-Induced Compaction and Implications on Production Rate. Presented at the SPE Annual Technical Conference and Exhibition, Society of Petroleum Engineers. <https://doi.org/10.2118/191390-MS>
- Swanson, S. M., Karlsen, A. W., & Valentine, B. J. (2013). *Geologic assessment of undiscovered oil and gas resources: Oligocene Frio and Anahuac Formations, United States Gulf of Mexico coastal plain and State waters* (USGS Numbered Series No. 2013–1257) (p. 78). Reston, VA: U.S. Geological Survey. Retrieved from <http://pubs.er.usgs.gov/publication/ofr20131257>

Takahashi, M. (2003). Permeability change during experimental fault smearing. *Journal of Geophysical Research: Solid Earth*, 108(B5).

<https://doi.org/10.1029/2002JB001984>

Tao, Q., Bryant, S. L., Meckel, T., & Luo, Z. (2012). Wellbore Leakage Model for Above-Zone Monitoring at Cranfield, MS. Presented at the Carbon Management Technology Conference, Carbon Management Technology Conference.

<https://doi.org/10.7122/151516-MS>

Tawiah, P., Duer, J., Bryant, S. L., Larter, S., O'Brien, S., & Dong, M. (2020). CO₂ injectivity behaviour under non-isothermal conditions – Field observations and assessments from the Quest CCS operation. *International Journal of Greenhouse Gas Control*, 92, 102843. <https://doi.org/10.1016/j.ijggc.2019.102843>

Tran, Settari, A., & Nghiem, L. (2004). New Iterative Coupling Between a Reservoir Simulator and a Geomechanics Module. *SPE Journal*, 9(03), 362–369.

<https://doi.org/10.2118/88989-PA>

Tran, Nghiem, L., & Buchanan, L. (2005). Improved Iterative Coupling of Geomechanics With Reservoir Simulation. Presented at the SPE Reservoir Simulation Symposium, OnePetro. <https://doi.org/10.2118/93244-MS>

Tran, D., Shrivastava, V. K., Nghiem, L. X., & Kohse, B. F. (2009). Geomechanical Risk Mitigation for CO₂ Sequestration in Saline Aquifers. Presented at the SPE Annual Technical Conference and Exhibition, OnePetro. <https://doi.org/10.2118/125167-MS>

Tucker, O., Gray, L., Maas, W., & O'Brien, S. (2016). Quest Commercial Scale CCS – The First Year. Presented at the International Petroleum Technology Conference, International Petroleum Technology Conference. <https://doi.org/10.2523/IPTC-18666-MS>

Uehara, S., & Shimamoto, T. (2004). Gas permeability evolution of cataclasite and fault gouge in triaxial compression and implications for changes in fault-zone permeability structure through the earthquake cycle. *Tectonophysics*, 378(3–4), 183–195. <https://doi.org/10.1016/j.tecto.2003.09.007>

Usman, M. B. I., & Haris, A. (2019). Reservoir Characterization Sandstone Reservoir Based on Wireline Log. *IOP Conference Series: Materials Science and Engineering*, 546, 072011. <https://doi.org/10.1088/1757-899X/546/7/072011>

Verdon, J. P. (2014). Significance for secure CO₂ storage of earthquakes induced by fluid injection. *Environmental Research Letters*, 9(6), 064022. <https://doi.org/10.1088/1748-9326/9/6/064022>

Verdon, J. P., Kendall, J.-M., Stork, A. L., Chadwick, R. A., White, D. J., & Bissell, R. C. (2013). Comparison of geomechanical deformation induced by megatonne-scale CO₂ storage at Sleipner, Weyburn, and In Salah. *Proceedings of the National Academy of Sciences*, 110(30), E2762–E2771. <https://doi.org/10.1073/pnas.1302156110>

Vrolijk, P. J., Urai, J. L., & Kettermann, M. (2016). Clay smear: Review of mechanisms and applications. *Journal of Structural Geology*, 86, 95–152. <https://doi.org/10.1016/j.jsg.2015.09.006>

- Waal, D., A, J., van Thienen-Visser, K., & Pruiksma, J. P. (2015). Rate Type Isotach Compaction of Consolidated Sandstone. Presented at the 49th U.S. Rock Mechanics/Geomechanics Symposium, American Rock Mechanics Association. Retrieved from <https://www.onepetro.org/conference-paper/ARMA-2015-436>
- White. (2016). Assessing induced seismicity risk at CO₂ storage projects: Recent progress and remaining challenges. *International Journal of Greenhouse Gas Control*, 49, 413–424. <https://doi.org/10.1016/j.ijggc.2016.03.021>
- Wibberley, C. A. J. (2002). Hydraulic diffusivity of fault gouge zones and implications for thermal pressurization during seismic slip. *Earth, Planets and Space*, 54(11), 1153–1171. <https://doi.org/10.1186/BF03353317>
- Wilson, M. J. ., & Wilson, L. (2014). Clay mineralogy and shale instability: an alternative conceptual analysis. *Clay Minerals*, 49(2), 127–145.
<https://doi.org/10.1180/claymin.2014.049.2.01>
- Wollenweber, J., Alles, S., Busch, A., Krooss, B. M., Stanjek, H., & Littke, R. (2010). Experimental investigation of the CO₂ sealing efficiency of caprocks. *International Journal of Greenhouse Gas Control*, 4(2), 231–241.
<https://doi.org/10.1016/j.ijggc.2010.01.003>
- Yielding et al. (1997). Quantitative Fault Seal Prediction. *AAPG Bulletin*, 81 (1997).
<https://doi.org/10.1306/522B498D-1727-11D7-8645000102C1865D>
- Yielding, G. (2002). Shale Gouge Ratio — calibration by geohistory. In *Norwegian Petroleum Society Special Publications* (Vol. 11, pp. 1–15). Elsevier.
[https://doi.org/10.1016/S0928-8937\(02\)80003-0](https://doi.org/10.1016/S0928-8937(02)80003-0)

- Yielding, G. (2012). Using probabilistic shale smear modelling to relate SGR predictions of column height to fault-zone heterogeneity. *Petroleum Geoscience*, 18(1), 33–42. <https://doi.org/10.1144/1354-079311-013>
- Yuan, Y., & Rezaee, R. (2019). Fractal analysis of the pore structure for clay bound water and potential gas storage in shales based on NMR and N₂ gas adsorption. *Journal of Petroleum Science and Engineering*, 177, 756–765. <https://doi.org/10.1016/j.petrol.2019.02.082>
- van der Zee, W., & Urai, J. L. (2005). Processes of normal fault evolution in a siliciclastic sequence: a case study from Miri, Sarawak, Malaysia. *Journal of Structural Geology*, 27(12), 2281–2300. <https://doi.org/10.1016/j.jsg.2005.07.006>
- Zee, W. van der, Urai, J. L., & Richard, P. D. (2003). Lateral clay injection into normal faults. *GeoArabia*, 8(3), 501–522.
- Zeidouni, M., & Pooladi-Darvish, M. (2012a). Leakage characterization through above-zone pressure monitoring: 1—Inversion approach. *Journal of Petroleum Science and Engineering*, 98–99, 95–106. <https://doi.org/10.1016/j.petrol.2012.09.006>
- Zeidouni, M., & Pooladi-Darvish, M. (2012b). Leakage characterization through above-zone pressure monitoring: 2—Design considerations with application to CO₂ storage in saline aquifers. *Journal of Petroleum Science and Engineering*, 98–99, 69–82. <https://doi.org/10.1016/j.petrol.2012.09.005>
- Zhang, & Sheng, J. J. (2017). Effects of Salinity and Confining Pressure on Hydration-Induced Fracture Propagation and Permeability of Mancos Shale. *Rock Mechanics*

- and Rock Engineering*, 50(11), 2955–2972. <https://doi.org/10.1007/s00603-017-1278-z>
- Zhang, S., & Cox, S. F. (2000). Enhancement of fluid permeability during shear deformation of a synthetic mud. *Journal of Structural Geology*, 9.
- Zhao, Y., & Yu, Q. (2017). CO₂ breakthrough pressure and permeability for unsaturated low-permeability sandstone of the Ordos Basin. *Journal of Hydrology*, 550, 331–342. <https://doi.org/10.1016/j.jhydrol.2017.04.050>
- Zheng, X., & Espinoza, D. N. (2021). Multiphase CO₂-brine transport properties of synthetic fault gouge. *Marine and Petroleum Geology*, 129, 105054.
<https://doi.org/10.1016/j.marpetgeo.2021.105054>
- Zhou, Q., Birkholzer, J. T., Tsang, C.-F., & Rutqvist, J. (2008). A method for quick assessment of CO₂ storage capacity in closed and semi-closed saline formations. *International Journal of Greenhouse Gas Control*, 2(4), 626–639.
<https://doi.org/10.1016/j.ijggc.2008.02.004>
- Zimmerman. (1990). *Compressibility of Sandstones*. Elsevier.
- Zimmerman. (2000a). Coupling in poroelasticity and thermoelasticity. *International Journal of Rock Mechanics and Mining Sciences*, 37(1–2), 79–87.
[https://doi.org/10.1016/S1365-1609\(99\)00094-5](https://doi.org/10.1016/S1365-1609(99)00094-5)
- Zimmerman. (2017). Pore Volume and Porosity Changes under Uniaxial Strain Conditions. *Transport in Porous Media*, 119(2), 481–498.
<https://doi.org/10.1007/s11242-017-0894-0>

Zimmerman, Somerton, W. H., & King, M. S. (1986). Compressibility of porous rocks.

Journal of Geophysical Research: Solid Earth, 91(B12), 12765–12777.

<https://doi.org/10.1029/JB091iB12p12765>

Zimmerman, R. W. (2000b). Implications of Static Poroelasticity for Reservoir Compaction. Presented at the 4th North American Rock Mechanics Symposium, American Rock Mechanics Association. Retrieved from
<https://www.onepetro.org/conference-paper/ARMA-2000-0169>

Zoback, M. D., & Gorelick, S. M. (2012). Earthquake triggering and large-scale geologic storage of carbon dioxide. *Proceedings of the National Academy of Sciences*, 109(26), 10164–10168. <https://doi.org/10.1073/pnas.1202473109>